In-Plane All-Photonic Transduction Method

For Silicon Photonic Microcantilever

Array Sensors

Jong Wook Noh

A dissertation submitted to the faculty of
Brigham Young University
in partial fulfillment of the requirements for the degree of

Doctor of Philosophy

Gregory P. Nordin, Chair
Brian D. Jensen
Aaron R. Hawkins
Stephen M. Schultz
Richard H. Selfridge

Department of Electrical and Computer Engineering

Brigham Young University

December 2009

Copyright © 2009 Jong Wook Noh

All Rights Reserved

ABSTRACT

In-plane All-photonic Transduction Method

For Silicon Photonic Microcantilever

Array Sensor

Jong Wook Noh

Department of Electrical and Computer Engineering

Doctor of Philosophy

We have invented an in-plane all-photonic transduction method for photonic microcantilever arrays that is scalable to large arrays for sensing applications in both bio- and nanotechnology. Our photonic transduction method utilizes a microcantilever forming a single mode rib waveguide and a differential splitter consisting of an asymmetric multimode waveguide and a Y-branch waveguide splitter. The differential splitter's outputs are used to form a differential signal that has a monotonic response to microcantilever deflection. A differential splitter using an amorphous silicon strip-loaded multimode rib waveguide is designed and fabricated to demonstrate the feasibility of the in-plane photonic transduction method. Our initial implementation shows that the sensitivity of the device is 0.135×10^{-3} nm^{-1} which is comparable to that of other readout methods currently employed for static-deflection based sensors.

Through further analysis of the optical characteristics of the differential splitter, a new asymmetric double-step multimode rib waveguide has been devised for the differential splitter. The new differential splitter not only improves sensitivity and reduces size, but also eliminates several fabrication issues. Furthermore, photonic microcantilever arrays are integrated with the differential splitters and a waveguide splitter network in order to demonstrate scalability. We have achieved a measured sensitivity of 0.32×10^{-3} nm^{-1}, which is 2.4 times greater than our initial result while the waveguide length is 6 times shorter.

Analytical examination of the relationship between sensitivity and structure of the asymmetric double-step rib waveguide shows a way to further improve performance of the photonic microcantilever sensor. We have demonstrated experimentally that greater sensitivity is achieved when increasing the step height of the double-step rib waveguide. Moreover, the improved sensitivity of the photonic microcantilever system, 0.77×10^{-3} nm^{-1}, is close to the best reported sensitivities of other transduction methods ($\sim10^{-3}$ nm^{-1}).

Keywords: Jong Wook Noh, microcantilever, in-plane photonic transduction, photonic microcantilever array sensor

ACKNOWLEDGMENTS

I owe my gratitude to all of the people who have made this research possible, especially for their personal and technical support. Thus my sincere gratitude goes to my parents, family, friends, and colleagues.

My deepest gratitude goes to my advisor, Dr. Gregory P. Nordin. I have been amazingly fortunate to have his guidance to help me follow through with my goals. Greg taught me not only how to do research but also how to guide my life. His patience and support have helped me to resolve many difficult problems and situations.

I would like to express my appreciation to all members of my advisory committee, Dr. Brian Jensen, Dr. Aaron Hawkins, Dr. Stephen Schultz, and Dr. Richard Selfridge for their comments and help in validating my research results. Special thanks goes to Dr. Seunghyun Kim, who was willing to help and give his best suggestions.

My research for this dissertation would not have been successful without the efforts of the all colleagues in our research group. I am particularly thankful to Ryan Anderson for helping me test samples, commenting on my reports, discussing problems, and sharing ideas with me.

Most importantly, my long tenure as a graduate student would not have been possible without the support and patience of my family. I wish to express my heartfelt gratitude to my parents. I am also deeply indebted to my daughter and my wife Hyojin. Their love and support have encouraged me to keep moving forward throughout this endeavor.

Finally, I would like to acknowledge the financial support from NSF grants ECS-0602261 and IIS-0641973, and DARPA grant 66001-04-8933 that funded parts of the research for this dissertation.

TABLE OF CONTENTS

LIST OF TABLES vii

LIST OF FIGURES ix

1 Introduction 1

1.1 Motivation 1

1.2 Overview of Dissertation 3

1.3 Contributions 4

2 Background 7

2.1 History 7

2.2 Microcantilever Theory 9

2.2.1 Operation Principles: Static Mode 10

2.2.2 Operation Principles: Dynamic Mode 15

2.3 Transduction Principles 20

2.4 Readout Methods 21

2.4.1 Piezoresistive Method 22

2.4.2 Capacitive Method 23

2.4.3 Optical Lever Method 24

2.5 Functionalization 25

2.6 Applications 27

3 In-plane Photonic Transduction for SOI Microcantilevers 29

3.1 Optical Waveguide Transduction Method 29

3.2 Photonic Waveguide Microcantilever Design 31

3.3 Design and Fabrication of Photonic Microcantilever System 41

3.4 Experimental Measurement 48

3.5 Analysis and Discussion 52

3.6 Conclusion 58

4 Differential Splitter Using Double-Step Rib Waveguide 59

4.1 Design of Differential Splitter with Double-Step Rib Waveguide 59

4.2 Fabrication of Photonic Microcantilever and Differential Splitter Array System 64

4.3 Experimental Measurement 67

4.4 Analysis and Discussion 73

4.5 Conclusion 75

5 Sensitivity Enhancement of Differential Signals 77

5.1 Sensitivity of Photonic Microcantilever Sensor 77

5.2 Analysis 79

5.3 Fabrication 84

5.4 Measurement and Discussion 86

5.5 Conclusion 88

6 Summary and Future Work 89

6.1 Summary 89

6.2 Future Work 92

7 References 95

LIST OF TABLES

Table 2-1: The first five wave numbers for the frequency characteristic equation 16

Table 5-1: Sensitivity and MDD comparison with other transduction methods reported 78

LIST OF FIGURES

Figure 2-1: A schematic description of an atomic force microscopy and SEM images of commercially available microcantilever probe tips (courtesy: www.xintek.com and www.nano.org.tr) 8

Figure 2-2: Cantilever beam deflection 10

Figure 2-3: Cantilever beam geometry and bending moment 12

Figure 2-4: Shape of the first four vibration mode of a cantilever beam........ 17

Figure 2-5: Microcantilever operation modes: (a) static mode (surface stress) (b) dynamic mode (microbalance) (c) dynamicmode (thermogravimetry) 20

Figure 2-6: Schematic drawing of the piezoresistive readout method for microcantilevers 22

Figure 2-7: Schematic drawing of the capacitive readout method 23

Figure 2-8: Conceptual sketch of the optical readout method using laser beam reflection technique 24

Figure 3-1: (a) Schematic layout of photonic microcantilever with single mode receiver waveguide (b) Waveguide cross section (c) Simulation result for the normalized power in the output waveguide as a function of microcantilever deflection. Simulations are performed with FIMMWAVE/PROP by Photon Design. 30

Figure 3-2: (a) Schematic 3-D layout of the photonic microcantilever system with the in-plane photonic transduction method (b) asymmetric amorphous silicon strip-loaded multimode waveguide 32

Figure 3-3: Top view of waveguide device layout for photonic simulation........ 33

Figure 3-4: Intensity profiles (top view) of that (a) upward deflection (+0.5 μm), (b) zero-deflection (0), and (c) downward deflection (-0.5 μm) cases of the input waveguide microcantilever........ 33

Figure 3-5: Simulation results for output power as a function of microcantilever deflection. 34

Figure 3-6: Differential signal as a function of the deflection of the input waveguide microcantilever........ 34

Figure 3-7: (a) Optical power in each output and (b) contrast of the differential signal for arbitrarily chosen lengths as a function of the length of the strip-loaded multimode rib waveguide. 36

Figure 3-8: Simulation results of the contrast of the differential signal as a function of the thickness of the amorphous silicon strip-loading on the multimode receiver waveguide for four different thickness cases for an asymmetric multimode rib waveguide length of 100 μm. 37

Figure 3-9: (a) Optical power in output as a function of the length of the strip-loaded waveguide, (b) contrast of the differential signal in the selected length of the strip-loaded waveguide 38

Figure 3-10: (a) Intensity profile of the fundamental TE (transverse electric) mode of the single mode rib waveguide. The asymmetric amorphous silicon strip-loaded multimode rib waveguide guides two TE modes, the (b) fundamental and (c) first order modes. 39

Figure 3-11: The mode coupling between the incident mode and two guided modes as a function of deflection. Dashed lines show the maximum mode coupling deflection position. 40

Figure 3-12: Single set of a photonic microcantilever system 41

Figure 3-13: Design parameters for (a) input waveguide splitter with S-bend structures, (b) S-bend in the output single mode waveguide, (c) the tapered multi- to single-mode waveguide section 42

Figure 3-14: Schematic layout of a 1 cm^2 die which has 8 copies of a single microcantilever set 43

Figure 3-15: Fabrication flow chart for wafer based process 45

Figure 3-16: Fabrication flow chart for individual die based process 46

Figure 3-17: (a) Microscope image of a waveguide microcantilever fabricated on a SOI wafer, SEM images of (b) after releasing the microcantilever, (b) close up of microcantilever and strip-loaded multimode receiving waveguide, and (d) close up of a gap. 47

Figure 3-18: Schematic of the experimental set-up using thermally treated SU-8 to bend the cantilever beam up. 48

Figure 3-19: SEM image of a cantilever beam bent up by a stressed SU-8 patch. 49

Figure 3-20: CCD camera image during an experiment to demonstrate the photonic waveguide microcantilever transduction mechanism. 49

Figure 3-21: Measured output power as a function of piezoactuator position. 50

Figure 3-22: P_1 and P_2 as a function of deflection of the microcantilever converted from the piezoactuator position 51

Figure 3-23: Definition of counter-clockwise (ccw) and clockwise (cw) rotation 52

Figure 3-24: Offset and contrast as a function of rotation angle of the microcantilever about the z-axis. 53

Figure 3-25: Simulation result of input waveguide microcantilever tilted 3.3 degree ccw direction about z-axis. 54

Figure 3-26: Differential signals tilted 3.3 degree to ccw direction as different ratios of P_1/ P_2.. 55

Figure 3-27 Comparison with the simulation and measurement results 56

Figure 4-1: Schematic illustration of in-plane all-photonic microcantilever transduction structure based on a differential splitter composed of an asymmetric double-step multimode rib waveguide and Y-branch splitter 60

Figure 4-2: Cross section of the double-step rib waveguide. Dashed regions indicate the etched area from the initial multimode rib waveguide. Buried oxide layer thickness is 3 μm and the remaining silicon layer thickness is 0.55 μm. 61

Figure 4-3: Normalized P_1 and P_2 output powers (left axis) and contrast of the differential signal (right axis) for selected lengths as a function of the length of the double-step rib waveguide. 62

Figure 4-4: Output powers as a function of deflection for a 17 μm long double-step rib waveguide. 63

Figure 4-5: Differential signal calculated from outputs, P_1 and P_2, as a function of deflection ... 63

Figure 4-6: Schematic of photonic microcantilever array sensor with Y-branch splitter network 64

Figure 4-7: Layout of an 8-microcantilever array with associated Y-branch input splitter network. Each fabricated die includes two such structures. 65

Figure 4-8: SEM images of (a) and (b) an 8-microcantilever array with SU8 bending patches on the top half of the array, (c) a photonic microcantilever that is 110 μm long and 45 μm wide, and (d) a double-step rib waveguide differential splitter. 66

Figure 4-9: Sketch of measurement setup for an 8-microcantilever array 68

Figure 4-10: Measured individual (a) P_1 and (b) P_2 output powers as a function of deflection for 14 out of 16 microcantilevers from two array sets. (c) Both outputs, for example, from microcantilever #4 of Set 2 are plotted in the same graph. There is a lateral shift, Δ, as expected. 69

Figure 4-11: SEM image shows clearly a defect which breaks waveguides of microcantilever #4 and #5 in the array set 1 69

Figure 4-12: Differential signals as a function of deflection 71

Figure 4-13: SEM images of microcantilever (a) #8 of Set 1, (b) #1 of Set 2, and (c) #8 of Set 2 72

Figure 4-14: Scaled differential signals as a function of deflection. 72

Figure 4-15: Comparison of measured data with simulation results 73

Figure 5-1: Schematic of photonic microcantilever and asymmetric differential splitter 79

Figure 5-2: Cross-section of the asymmetric double-step multimode rib waveguide 79

Figure 5-3: Output power profiles and the scaled differential signal as a function of deflection. 80

Figure 5-4: Simulation results for four different step-height cases. 81

Figure 5-5: (i) Fundamental and (ii) first order mode profiles, and top view of mode propagation in differential splitter for the (iii) fundamental and (iv) first order modes for 50 nm and 200 nm step heights........ 82

Figure 5-6: Mode coupling as a function of microcantilever deflection. 83

Figure 5-7: Peak Maxima separation for mode coupling and lateral shift of P_1 and P_2 as a function of step height. 84

Figure 5-8: SEM images of photonic microcantilever array system 85

Figure 5-9: Average scaled differential signal as a function of deflection from measurement data of four photonic microcantilever arrays. 86

Figure 5-10: Average slope as a function of step height for measurement and simulation........ 87

Figure 5-11: Average maxima separation of output powers as a function of step height for measurement and simulation........ 87

1 INTRODUCTION

1.1 Motivation

Microcantilevers as nanomechanical sensing devices [1, 2] have been investigated for biological [2-9], chemical [1, 10-12], and environmental [13] sensing applications due to their high sensitivity, selectivity, and label-free operation. To utilize microcantilevers for sensing, a chemo- or bio-selective layer is coated on the surface of each microcantilever beam. When target molecules are adsorbed on the selective layer, typically either a change in mass is measured by determining the shift in microcantilever resonance frequency or a change in surface stress is determined by measuring deflection of the beam [14]. Measurement of resonance frequency shifts tend to be done in vapor or vacuum ambients, while deflection measurement is particularly suited to liquid environments.

The sensitivity of microcantilever-based sensors is affected by the readout method chosen to determine changes in microcantilever properties. Moreover, the readout method influences the number of microcantilevers that can be simultaneously detected in an array. Typical readout methods include laser beam reflection [3-5, 10], piezoresistive [6-9, 13, 15, 16], piezoelectric [11, 17], and capacitive [18, 19] approaches. Reflection of a laser beam from the end of a microcantilever and measurement with a position-sensitive photodetector are well-known in atomic force microscopy (AFM). Although this optical readout method can have sub-angstrom resolution, it is typically limited in the number of microcantilevers that can be simultaneously

measured. Alternatively, piezoresistive and piezoelectric approaches are adaptable to batch microfabrication techniques such that large numbers of microcantilevers can in principle be fabricated on a single chip, but these methods tend to suffer from electrical and system noise, which influence detection sensitivity. In the capacitive approach changes in capacitance between a microcantilever and an adjacent surface are measured. While this approach can be very sensitive in some implementations, its use is difficult for situations in which the dielectric constant of the medium between the surfaces varies, such as is the case for many biosensing scenarios.

In short, a scalable, simultaneous, high sensitivity microcantilever transduction method has not to date been demonstrated. Such a method is necessary to use arrays of microcantilevers as a parallel sensor platform. The focus of this dissertation is to develop and demonstrate a new in-plane photonic transduction method that achieves the high sensitivity of the optical readout method while being scalable to simultaneous readout of many microcantilevers on a single chip. The approach comprises a microcantilever that forms a single mode waveguide in which light propagates down the length of the microcantilever, crosses a small gap, and is captured in an asymmetric multimode waveguide section that terminates in a Y-branch. By forming a differential signal with the outputs of the Y-branch, a monotonic dependence of the differential signal on microcantilever deflection can be realized. This dissertation covers design, fabrication, measurement, and analysis of in-plane all-photonic transduction for photonic microcantilever arrays.

1.2 Overview of Dissertation

This dissertation is organized as follows. Chapter 2 introduces microcantilevers and their mechanical properties, as well as the fundamentals of microcantilever-based sensors.

Chapter 3 presents the design of photonic silicon-on-insulator microcantilevers and an in-plane photonic transduction method using amorphous silicon strip-loaded multimode rib waveguides. Fabrication and measurement of microcantilevers for experimental demonstration of this transduction technique are discussed, followed by analysis of the experimental data. The measurement sensitivity of the differential signal is found to be 0.135×10^{-3} nm^{-1}, which is at least two orders of magnitude greater than piezoresistive transduction techniques and comparable to other optical transduction methods.

Chapter 4 introduces a differential splitter using an asymmetric double-step multimode rib waveguide for in-plane photonic transduction of photonic microcantilever deflection. Arrays of multiple photonic microcantilevers are integrated with differential splitters and a waveguide splitter network to demonstrate sensitivity and uniformity of the transduction. Measurement results indicate a sensitivity of 0.32×10^{-3} nm^{-1} with a minimum detectable deflection of 141 pm for a 3.5 Hz measurement bandwidth.

The sensitivity of microcantilever-based devices is a function of the microcantilever properties, readout method, and detection apparatus. The sensitivity also determines the minimum detectable deflection (MDD). In Chapter 5, we investigate the effect on the sensitivity of modifying the asymmetric structure of the double-step multimode rib waveguide. The relationship of the structure and sensitivity is investigated analytically and then demonstrated experimentally. We show that the sensitivity is enhanced by modifying the step height of the

double-step rib waveguide. The sensitivity obtained experimentally is 0.77×10^{-3} nm^{-1}, which is close to the best reported sensitivity of optical readout methods.

The final chapter includes a summary and suggestions for future work.

1.3 Contributions

My specific contributions to designing and experimentally demonstrating in-plane all-photonic transduction for photonic microcantilever arrays are enumerated below.

1. In 2004, Dr. Gregory P. Nordin proposed a transduction method for optical waveguide microcantilevers which utilizes a differential splitter consisting of an asymmetric strip-loaded multimode rib waveguide and a Y-branch splitter and a single mode rib waveguide embedded microcantilever. A patent was issued in 2007 based on simulations for silicon nitride microcantilevers and waveguides. [20] I developed an implementation for silicon microcantilevers and waveguides since silicon-based photonic devices showed significantly improved practical performance. This involved performing a series of photonic simulations to optimize the geometry of the silicon implementation to maximize the differential signal. I also did tolerance analysis to examine fabrication feasibility (Chapter 3).
2. I developed the fabrication processes for silicon-on-insulator microcantilever and optical waveguide devices, which required high alignment accuracy and tight feature dimension tolerance. We used a hybrid method of photolithography and electron beam lithography (EBL) to build the photonic microcantilever system with differential splitters using an amorphous silicon strip-loaded multimode rib waveguide in order to demonstrate the in-plane photonic transduction method. As a result, the amorphous silicon strip was

fabricated with position and dimension accuracy of 100 nm, and the gap was less than 300 nm wide.

3. I invented a method to manipulate microcantilever deflection by utilizing thermally stressed SU8. Due to thermally driven epoxy cross-linking, a SU8 polymer film patterned on top of a microcantilever experiences tensile stress which results in bending up the microcantilever. By using a probe tip attached to a piezotranslator, microcantilever deflection could be accurately controlled by pushing down on the microcantilever. With this approach we have demonstrated that a differential signal has a monotonic response over the full deflection range of ±0.5 μm.
4. Discrepancies were observed between measurement and simulation. Therefore, I investigated further to resolve them. From data analysis and simulations, I found that the discrepancies were due to microcantilever rotation and a non-unity P_1/P_2 peak ratio. Pushing down the microcantilever with a probe tip induced microcantilever rotation about its long axis unless the contact position of the probe tip was exactly on the center line of the cantilever beam. Non-unitiy P_1/P_2 peak ratio is caused by individual waveguide's property differences due to different defects in the waveguides, quality of the polished outputs, and output fiber coupling efficiency. The effects are explained in detail in a published paper [21].
5. I designed a new differential splitter using an asymmetric double-step multimode rib waveguide to improve both optical performance and fabrication reliability. I demonstrated these benefits together with array integration, by designing and fabricating photonic microcantilever arrays integrated with the newly designed differential splitters

and a waveguide splitter network. This work on the double-step rib waveguide-based differential splitter has been published [22].

6. Upon further analysis, I realized that the double-step waveguide structure could be modified to increase the sensitivity of the transduction signal. This was verified by simulation, followed by sample fabrication and experimental measurement. The measurements show that the signal sensitivity is enhanced by modifying the structure of the double-step rib waveguide in the differential splitter through a larger step height. The result is a sensitivity that is comparable to the best reported sensitivity of other microcantilever transduction methods, which is approximately 10^{-3} nm^{-1}. A manuscript describing this work has been submitted [23].

In summary, I have been working on the most significant technical aspects of the photonic microcantilever device design, simulation, fabrication, and measurement to experimentally demonstrate a new, scalable, microcantilever transduction method that has high sensitivity. Moreover, I have also been integrally involved with integration of my photonic microcantilever device with microfluidic devices to demonstrate how it performs in sensing scenarios. Current work including the microfluidic and biosensing applications is briefly described in Chapter 6.

2 BACKGROUND

Microcantilever-based devices have been investigated by a variety of researchers since the sensitivity of microcantilever-based sensors was used to measure atomic forces between single atoms in the 1980s. In this chapter, I first briefly review the history of microcantilever sensors, followed by a discussion of cantilever beam theory and microcantilever properties. I then discuss conventional transduction principles, readout methods, functionalization, and applications for microcantilever sensor systems.

2.1 History

Atomic force microscopes (AFMs) based on microcantilevers made their debut in the early 1980s. [24] The atomic force microscope can measure ultra small forces on particles as small as single atoms. Its sensitivity has been proven at a sub angstrom range which could not be measured by conventional optical instruments because of the diffraction limit. Improvements in fabrication techniques have enhanced its capabilities over the years, allowing it to measure other physical, chemical, and electromagnetic properties such as temperature [25-27], mass [28-31], biochemical [1, 3-7, 9-12, 14, 32], and magnetic forces [33-35]. A conventional AFM consists of a microcantilever and readout system. The microcantilever is a tens of microns scale cantilever beam with a sharp tip at the end of the beam in order to scan a specimen surface. [24] When the tip approaches a specimen surface, forces between the tip and the surface lead to a displacement

of the microcantilever, and the scanning result over the surface is recorded to represent the surface contour image as shown Figure 2-1.

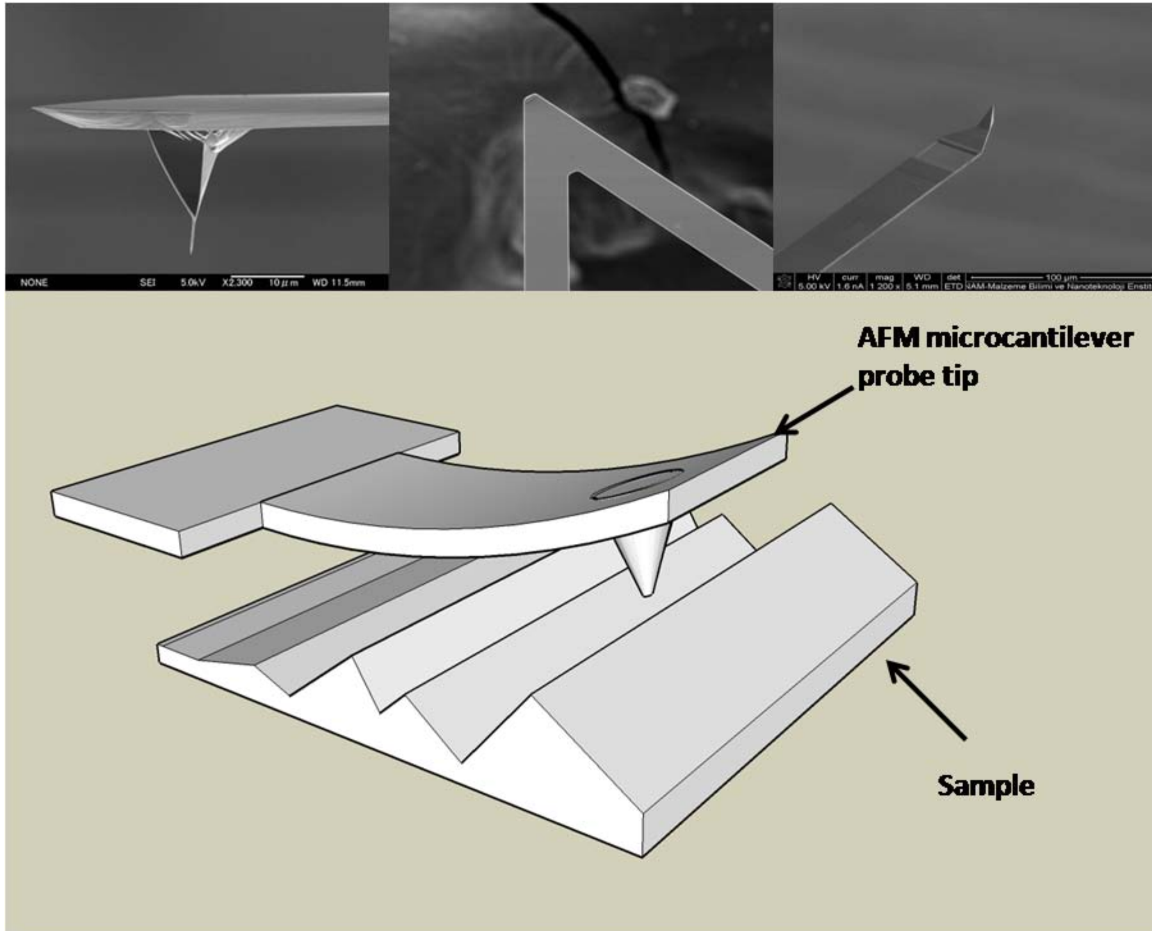

Figure 2-1: A schematic description of an atomic force microscopy and SEM images of commercially available microcantilever probe tips (courtesy: www.xintek.com and www.nano.org.tr)

Typical microcantilevers are made of silicon or silicon nitride. Readout methods to measure the motion of the microcantilever are optical lever, piezoresistive, piezoelectric, capacitive, and optical interferometry [36, 37] methods. The most sensitive readout method is the optical lever method [38, 39] in which a laser beam is reflected from the top surface of a

microcantilever to a position-sensitive photo detector. The operational mode of the AFM depends on the application; in general, the primary operation modes are divided into static and dynamic modes. In the static mode, also called a contact mode, the static deflection of the microcantilever is measured. In the dynamic mode, also called a non-contact mode, the microcantilever oscillates at its resonant frequency, and the resonant frequency is changed by forces between the tip and the surface. In this mode changes of the resonant frequency are measured.

In the mid-1990s, two research groups reported [26, 40] using AFM microcantilevers as sensors. Since then, microcantilever-based sensors have been demonstrated for various applications, and their versatility also has been realized by a variety of selective layers [2]. Currently, sensors using microcantilever transducers are being applied to diverse research fields. In order to understand how they work, first we need to investigate the fundamentals of microcantilever properties using a simple cantilever beam model.

2.2 Microcantilever Theory

A cantilever is a simple beam structure in which one end is fixed and the other is free. A cantilever beam is usually subjected to loads laterally or transversely to its axis, and is commonly used in structures and machines. In order to understand the mechanical behavior of the microcantilever as a cantilever beam, we briefly review cantilever beam theory.

Bernoulli-Euler beam theory is the most commonly used for scientific and engineering problems because of its reasonable approximations and simplicity. The Bernoulli-Euler beam model has the following basic assumptions: [41]

- One dimension is larger than the other two

- The material is linear elastic
- The Poisson effect is negligible
- The cross-sectional area is symmetric so that the neutral and centroid axes coincide
- Planes perpendicular to the neutral axis remain perpendicular after deformation
- The angle of rotation is small so that the small angle assumption can be used

The following sections describe the theory for mechanical behavior of a cantilever beam in bending and vibration. Cantilever operation is divided into static and dynamic modes which are used in sensing applications.

2.2.1 Operation Principles: Static Mode

Static mode indicates static deflection such that a rectangular cantilever beam is bent under the action of applied forces on the axis of the straight beam.

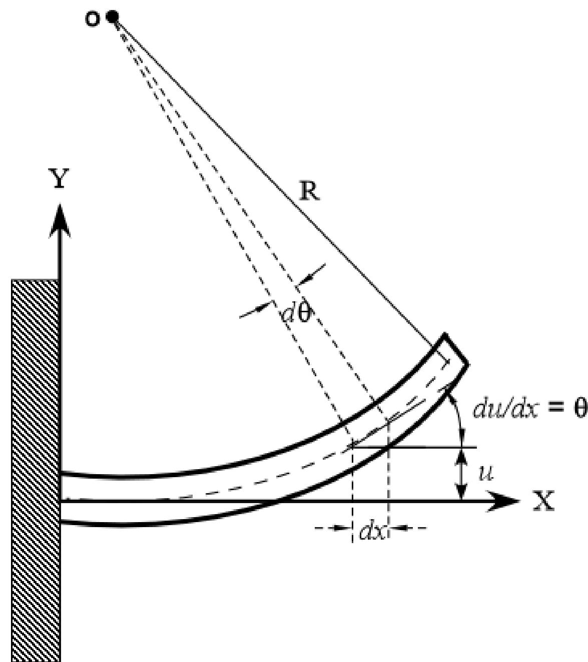

Figure 2-2: Cantilever beam deflection

The deflection u of the beam at the end is the displacement of the tip from the x-axis in the y-direction. The geometry is shown in Figure 2-2. The definition of the curvature ζ at a distance x from the y axis is expressed as [42]

$$\zeta = \frac{1}{R} = \frac{\frac{d^2u}{dx^2}}{\left[1+\left(\frac{du}{dx}\right)^2\right]^{3/2}} \quad \textbf{(2.1)}$$

where R is the radius of curvature.

The square of the slope, $(du/dx)^2$, may be negligible relative to unity since the assumption of the beam theory is the deflection of the beam is small compared with the length of the beam. Hence Equation 2.1 is expressed as

$$\zeta = \frac{1}{R} = \frac{d^2u}{dx^2}. \quad \textbf{(2.2)}$$

The curvature represents the rate at which the slope varies along the axis of the beam. There is a neutral axis of the cross section of the rectangular beam which is located at zero strain or stress. According to Hook's law of elasticity, the stress and strain relationship is denoted as

$$\sigma = \varepsilon E \quad \textbf{2.3}$$

where σ is normal stress, ε is strain, and E is Young's modulus. The concept of stress is a measure of the internal forces in the unit area reacting to external forces. When the bending moment is loaded onto a cantilever beam, it causes compression on one surface area and tension on the other. A compressive stress appears in the tension area, and a tensile stress in the compression area.

From the linear bending moment-curvature relationship, we can obtain

$$\zeta = \frac{1}{R} = \frac{M}{EI} \tag{2.4}$$

where M is a bending moment, E is Young's modulus, and the moment of inertia I of the cross section about the centroid axi is defined as: $I = \int y^2 dA$. The moment of inertia I for a rectangular cantilever beam is given by

$$I = \frac{bh^3}{12} \tag{2.5}$$

where b is width and h is thickness shown in Figure 2-3.

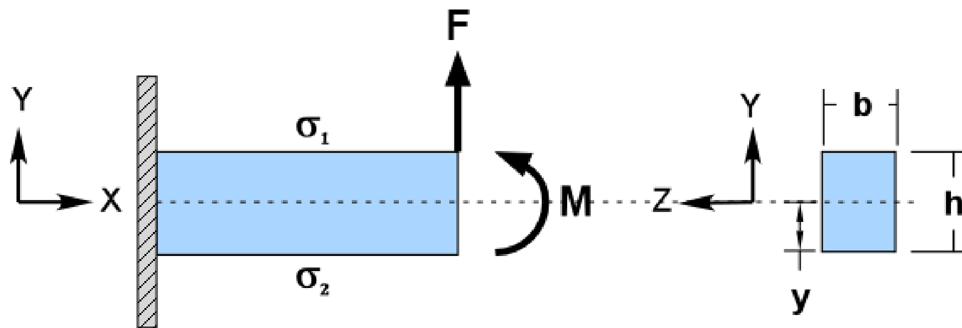

Figure 2-3: Cantilever beam geometry and bending moment

To obtain a differential equation for the deflection curve, the Equations 2.4 and 2.2 are combined,

$$\zeta = \frac{1}{R} = \frac{d^2u}{dx^2} = \frac{M}{EI}. \tag{2.6}$$

Solving Equation 2.6, the deflection angle and deflection can be expressed as

$$\theta = \frac{Mx}{EI} \ ,$$
$$\delta = \frac{Mx^2}{2EI} \ . \quad \textbf{(2.7)}$$

The maximum deflection angle and the maximum deflection at the free end of the cantilever beam due to the moment *M* can be calculated by substituting the length of the cantilever beam, *L*, into *x* with the results given by

$$\theta_{max} = \frac{ML}{EI} \ ,$$
$$\delta_{max} = \frac{ML^2}{2EI} \ . \quad \textbf{(2.8)}$$

Let's now consider a cantilever beam coated with a thin film on one surface. If the thin film is made of a different material from that of the cantilever, their mechanical properties and responses to stimuli will be different. As a result of the difference between the upper and lower stresses, σ_1 and σ_2 respectively, in the cantilever beam, a bending moment is induced which is described by

$$M = \frac{bh}{2}\Delta\sigma \quad \textbf{(2.9)}$$

where $\Delta\sigma = \sigma_1 - \sigma_2$ is the stress difference.

Inserting Equation 2.9 into 2.6, we can obtain one form of Stoney's formula: [43]

$$\frac{1}{R} = \frac{bh\Delta\sigma}{2EI} = \frac{6\Delta\sigma}{Eh^2}. \quad \textbf{(2.10)}$$

Stoney's formula has been modified by substituting *E* with *E/(1-v)* since surface stress is isotropic in all directions in the film which is assumed to be isotropic. [44] Hence Equation 2.10 becomes

$$\frac{1}{R} = \frac{6\Delta\sigma}{E(1-\nu)h^2} \tag{2.11}$$

where *v* is Poisson's ratio.

This modified Stoney's formula is used to calculate the surface stress and involves the following assumptions: [45]

i. Both film and substrate have uniform thickness and the same radius of curvature R;
ii. Both the strain and rotation of the beam are very small;
iii. Both the film and substrate are isotropic, homogeneous, and linear elastic;
iv. Surface stress components in the film are equi-biaxial or isotropic;
v. Curvature components are equi-biaxial;
vi. All stress and curvature components are spatially constant over the surface.

Surface stress changes can be caused by adsorption or interaction between molecules on the surface of the film and adsorbed molecules on the cantilever beam. Usually surface-stress-induced bending can cause static bending of the cantilever beam. Therefore, a microcantilever with a selective film layer can be used to detect molecular interaction on the film surface because surface stress changes caused by the interaction drive the microcantilever to bend.

2.2.2 Operation Principles: Dynamic Mode

In this section we review the resonant behavior of a cantilever beam. According to mechanical vibration theory, after disturbing a cantilever beam, it vibrates at its natural frequency since the inertia of the beam causes it to oscillate. First of all, the governing differential equation of motion of a cantilever beam obtained using Hamilton's principle is given in the following equation [41]

$$\rho A \frac{\partial^2 u\left(x,t\right)}{\partial t^2} + EI \frac{\partial^4 u\left(x,t\right)}{\partial x^4} = f\left(x,t\right) \quad \textbf{(2.12)}$$

where ρ is the density, A is the cross-sectional area, E is the Young' modulus, and I is the moment of inertia of the cantilever beam. A cantilever beam is fixed one end and is free the other so that at the fixed end both deflection and slope are zero and at the free end both shear force and bending moment are zero. This can be summarized as

$$\begin{aligned} &u = 0, \qquad \frac{\partial u}{\partial x} = 0 \quad \text{for fixed end,} \\ &\frac{\partial^2 u}{\partial x^2} = 0, \quad \frac{\partial^3 u}{\partial x^3} = 0 \quad \text{for free end.} \end{aligned} \quad \textbf{(2.13)}$$

As forming an initial-boundary-value problem, the differential Equation can be solved using eigenfunction expansion and variable separation. In order to solve the differential Equation of motion, first we consider a homogeneous problem by setting $f(x,t)=0$. By applying variable separation with $u(x,t)=W(x)T(t)$ where W is independent of time t and T is independent of position x, the differential Equation of motion can be separated into two ordinary differential Equations,

$$\frac{d^2T}{dt^2} + \omega_0{}^2 T(t) = 0 \,,$$
$$\frac{d^4W(x)}{dx^4} + \left(\frac{\alpha}{L}\right)^4 W(x) = 0 \qquad \textbf{(2.14)}$$

where L is the length of the cantilever and the dimensionless parameter α is defined as;

$$\left(\frac{\alpha}{L}\right)^4 = \frac{\rho A}{EI}\omega_0{}^2 \,. \qquad \textbf{(2.15)}$$

Solutions of the homogeneous differential equations are

$$T(t) = d_1 \sin \omega t + d_2 \cos \omega t \,,$$
$$W(x) = c_1 \sin\left(\frac{\alpha}{L}\right)x + c_2 \cos\left(\frac{\alpha}{L}\right)x + c_3 \sinh\left(\frac{\alpha}{L}\right)x + c_4 \cosh\left(\frac{\alpha}{L}\right)x \,. \qquad \textbf{(2.16)}$$

By applying boundary conditions to the spatial function $W(x)$, a characteristic frequency equation can be obtained as

$$\cos\alpha \cosh\alpha + 1 = 0 \qquad \textbf{(2.17)}$$

with the first five values α_i for the Equation 2.17 in Table 2-1. [41] Figure 2-4 shows schematics of the first four modes of a cantilever beam. [46]

Table 2-1: The first five wave numbers for the frequency characteristic equation

α_0	α_1	α_2	α_3	α_4
1.875	**4.694**	**7.855**	**10.996**	**14.137**

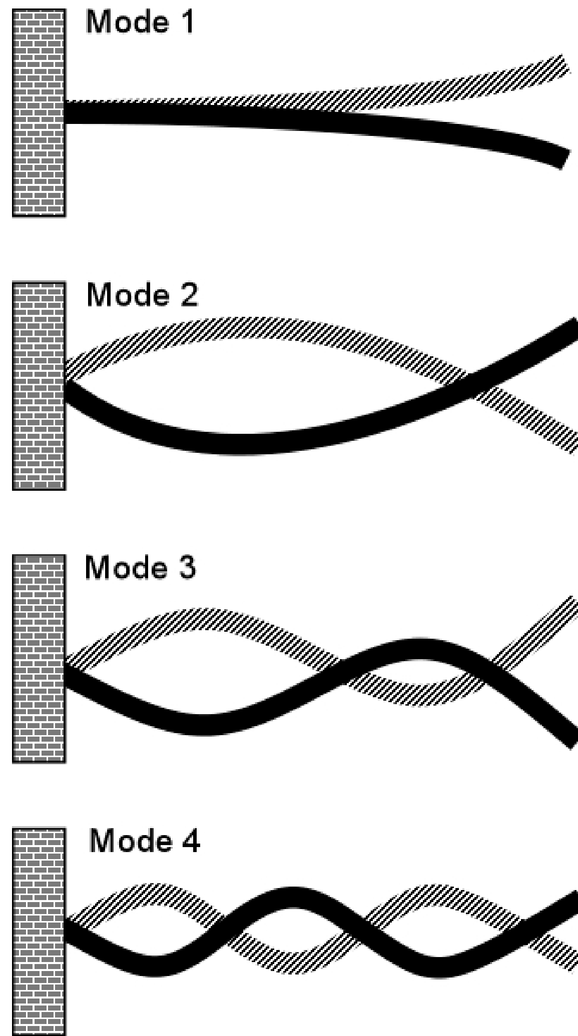

Figure 2-4: Shape of the first four vibration mode of a cantilever beam

An unloaded beam freely vibrating in a bending mode in a vacuum will have a number of resonant frequencies. [47] The general expression of the *i* th mode resonance of the beam, f_i, is given by

$$f_i = \frac{1}{2\pi}\left(\frac{\alpha_i}{L}\right)^2 \sqrt{\frac{EI}{\rho A}}. \qquad \textbf{2.18}$$

A spring constant, also known as a force constant, k, is defined as $k=F/x$ (i.e. $k=3EI/L^3$ for the rectangular cantilever beam). By substituting $\rho=m/bhL$ and $A=bh$ into Equation 2.18, f_i can be expressed with the spring constant term as shown in Equation 2.19,

$$f_i = \frac{\alpha_i^2}{2\pi\sqrt{3}}\sqrt{\frac{k}{m}} \tag{2.19}$$

where m is the mass of the cantilever beam.

If a thin film coated on the surface of the cantilever beam reacts with molecules or other reagents, same of the molecules will adhere to the cantilever. The mass of the cantilever beam will increase by the additional mass, Δm, of the gained layer. As a result of that, the resonance frequency of the cantilever beam will shift. The new frequency can be obtained by inserting the additional mass term Δm into Equation 2.19, which can be used to estimate the sensitivity of the cantilever beam to additional mass as

$$f_i^{\Delta m} = \frac{\alpha_i^2}{2\pi\sqrt{3}}\sqrt{\frac{k}{m+\Delta m}}. \tag{2.20}$$

Such an additional layer can also effect the stiffness of the cantilever beam since the cross-sectional area of the cantilever beam increases due to the adsorbed layer. The cantilever beam's moment of inertia is also changed and it can be expressed as

$$I_a = \frac{bh_a^3}{12} + bh_a\left(\frac{h_a}{2} - h - y_c\right)^2 \tag{2.21}$$

where h_a is the thickness of the adsorbed layer, h is the cantilever beam thickness, and y_c is the centroid of the total cross-sectional area including the adsorption layer given in Equation 2.22

$$y_c = \frac{Eh^2 + E_a(2h_a h + h_a^{\ 2})}{2E_a h_a + 2Eh}, \qquad \textbf{(2.22)}$$

where E_a is the Young's modulus of the adsorbed layer. As a result, the force constant of the cantilever beam changes with the additional force constant Δk defined by $\Delta k = \left(3E_a I_a / L^3\right)$. Thus, the resonance frequency can be modified by combining Δk into Equation 2.19 and is given by

$$f_i^{\Delta k} = \frac{\alpha_i^{\ 2}}{2\pi\sqrt{3}}\sqrt{\frac{k}{m}+\frac{\Delta k}{m}}. \qquad \textbf{(2.23)}$$

The surface stress change due to the interaction between molecules can be considered as another effect on the shift of the resonance frequency and is denoted in the following equations:

$$f_i^{\Delta\sigma} = \frac{1}{2\pi\sqrt{3}}\left[1+\frac{2\Delta\sigma L^3}{EI\pi^2}\right]\left(\frac{\alpha_i}{L}\right)^2\sqrt{\frac{k}{m}} \qquad \textbf{(2.24)}$$

where σ is surface stress defined by Equation 2.25;

$$\Delta\sigma = \left[\left(\frac{f_i^{\Delta\sigma}}{f_i}\right)^2 - 1\right]\frac{Ebh^3\pi^2}{24L^3}. \qquad \textbf{(2.25)}$$

Hence, the combination of the three Equations, 2.19, 2.23, and 2.24, are expressed a general case of a frequency shift due to additional mass, to additional stiffness, and to additional surface stress as shown in Equation 2.26

$$f_i^{\Delta m,\Delta k,\Delta\sigma} = \frac{1}{2\pi\sqrt{3}}\left[1+\frac{2\Delta\sigma L^3}{EI\pi^2}\right]\left(\frac{\alpha_i}{L}\right)^2\sqrt{\frac{k}{m+\Delta m}+\frac{\Delta k}{m+\Delta m}}. \qquad \textbf{(2.26)}$$

2.3 Transduction Principles

A sensor is a device that detects a physical quantity and transforms it into a signal. A sensor indicates a state or a value on an analog or digital display by a signal converter. In general, bio- or chemical sensors consist of a transducer and a selective layer so that measurable output signals can be generated in response to stimuli. A microcantilever as a transducer has been used in many different areas. [2, 48, 49] Before discussing modes of operation for microcantilever based sensors, three examples are illustrated in Figure 2-5.

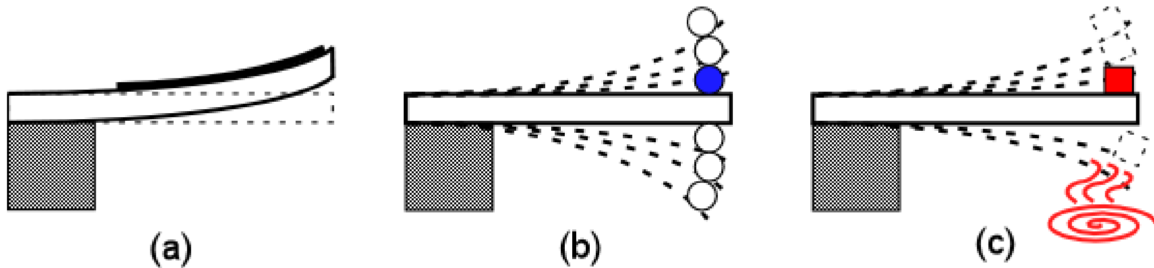

Figure 2-5: Microcantilever operation modes: (a) static mode (surface stress) (b) dynamic mode (microbalance) (c) dynamicmode (thermogravimetry)

In static mode, the following are examples of transduction principles: [2, 6-8, 14, 32, 43, 49]

- Surface stress in which an adsorbed layer of molecules on the selective layer-coated surface of a microcantilever beam induces a change
- Diffusion into polymer that diffusion of target molecules from the environment around a microcantilever beam causes swelling of the polymer layer,
- Biomolecular recognition that target molecules from the environment binds with analyte molecules on the selective layer coated surface

- Bimetallic thermal effect that a microcantilever composing of a sandwich of materials which have different thermal expansion coefficients bends as a change of temperature or heat

Some sensing scenarios using dynamic mode are as follows:

- Mass change that additional mass loading on the microcantilever beam causes a shift in its resonance frequency [28-31]
- Medium visco-elasticity that changes in viscosity or density of the environment influence the damping condition in the vibration mode of a microcantilever [50, 51]
- Thermogravimetry that tracks the resonant frequency shift of a microcantilever while changing the temperature to determine the additional mass change [52]

2.4 Readout Methods

The readout method plays an important role in which it is used to detect the mechanical state of a microcantilever. There are various readout methods in use for microcantilever sensors, and each method has different merits and problems. In this section, we describe common readout methods.

2.4.1 Piezoresistive Method

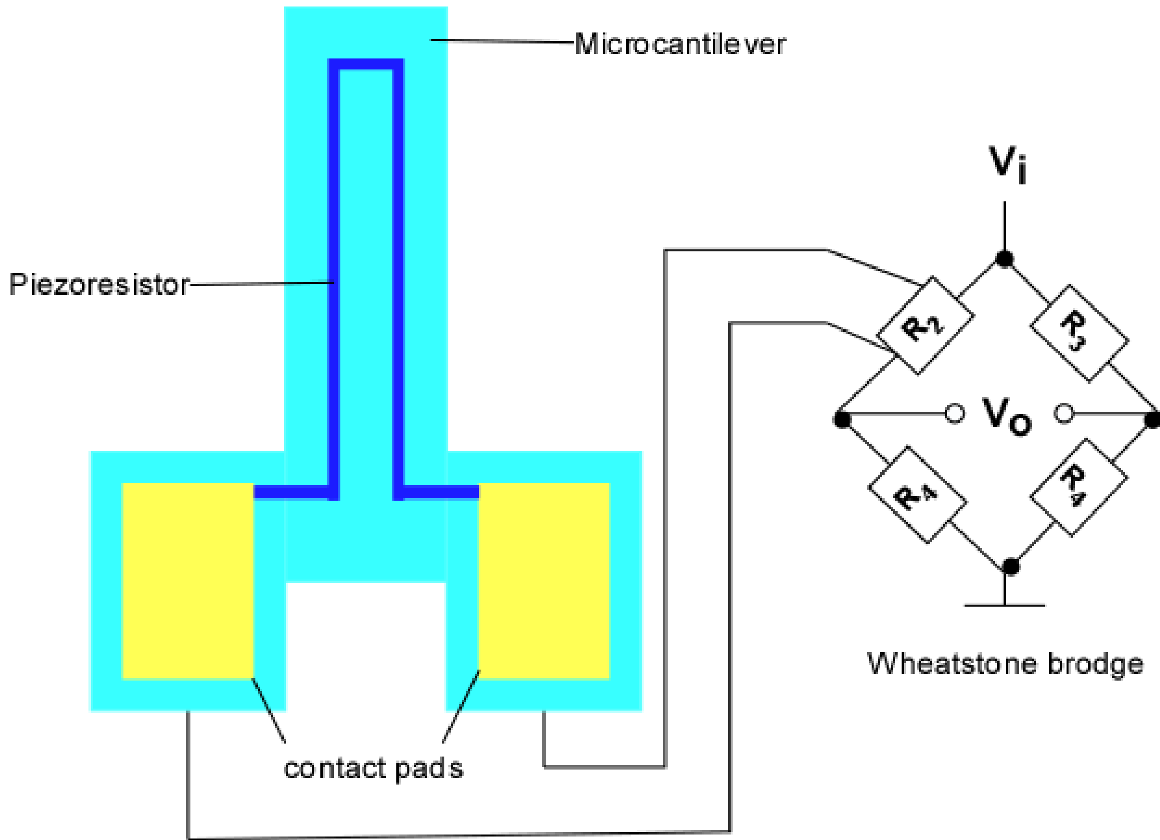

Figure 2-6: Schematic drawing of the piezoresistive readout method for microcantilevers

A schematic diagram of piezoresistive detection is shown in Figure 2-6. A piezoresistive material changes its electrical conductivity when external force is applied to it. A deflection of the microcantilever into which a piezoresistive material is integrated causes the change in resistance. The piezoreisistive effect is used in a Wheatstone bridge at the microcantilever sensor platform, and the microcantilever deflection or bending is determined by measuring the resistance change in the Wheatstone circuit. The piezoresistive readout method is well-suited to measure a large number of microcantilever arrays and to make a compact system such as a lab-

on-a-chip device. [15, 16, 35, 53, 54] The disadvantages of this technique are electronic, thermal, and conductance fluctuation noise, nonlinear response, thermal drifts caused by temperature changes, and poor sensitivity. [55, 56]

2.4.2 Capacitive Method

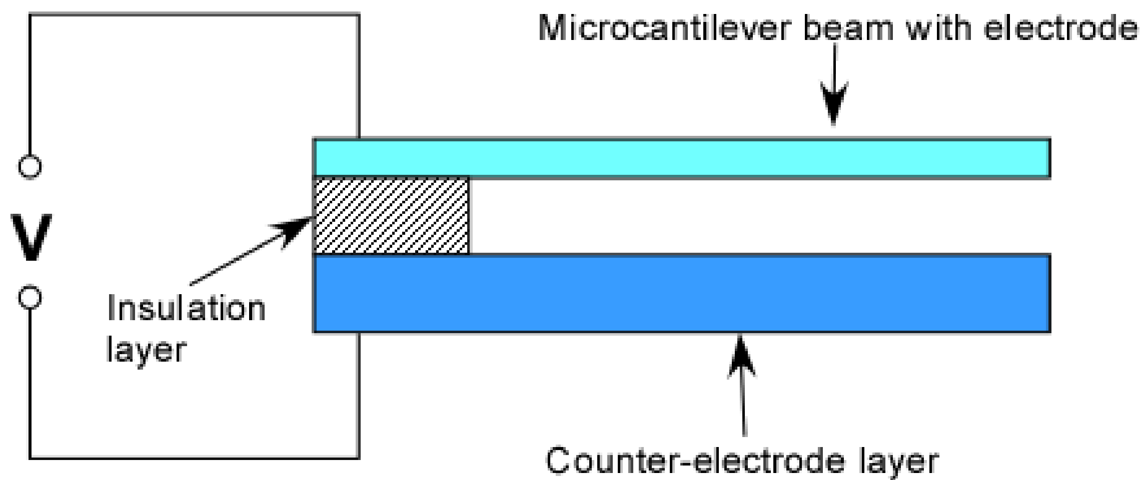

Figure 2-7: Schematic drawing of the capacitive readout method

A capacitive method is based on measuring the capacitance between an electrode on a microcantilever and another electrode fixed on the substrate underneath the microcantilever with a small separation as shown in Figure 2-7. [19] Upon mechanical movement of the microcantilever the capacitance between two electrodes changes and allows the deflection of the microcantilever to be determined. Sensitivity of the capacitive method is dependent on the separation distance between the microcantilever and the substrate because the capacitance is inversely proportional to the separation between two electrodes. This technique suffers from interference with changes in the effective dielectric constant of the medium around the electrodes

and from stiction when parallel electrode plates are brought in too close proximity. [2, 47] As a result, the capacitive method is usually used in gaseous and not aqueous media.

2.4.3 Optical Lever Method

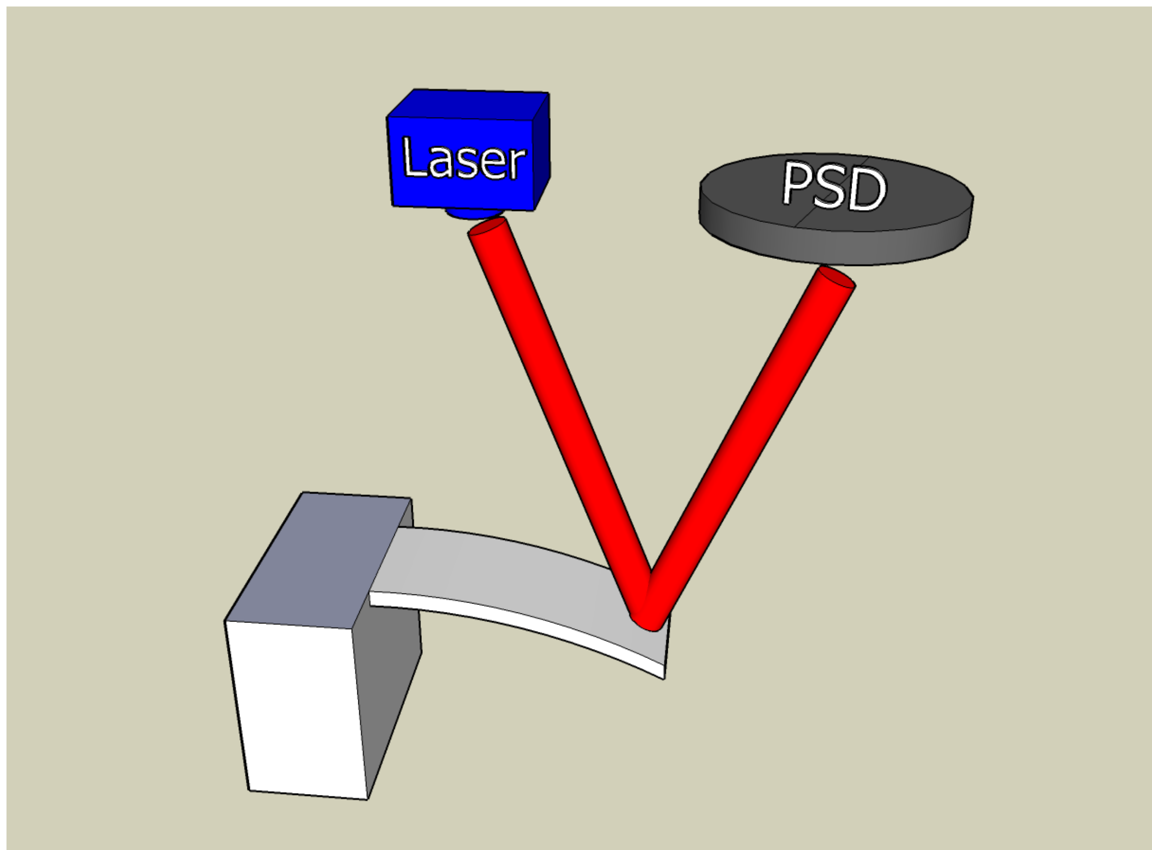

Figure 2-8: Conceptual sketch of the optical readout method using laser beam reflection technique

The most commonly used readout method is the optical lever technique shown in Figure 2-8, which is also called as laser beam reflection. It is applicable to both static and dynamic mode measurements. A laser beam focused on the microcantilever tip is reflected to a position-sensitive photodetector (PSD), where the reflected beam position is changed by the mechanical

motion of the microcantilever. This optical method can detect ultra small changes in microcantilever deflection as small as a few angstrom (=10^{-10}m) and is currently the most sensitive readout method for microcantilever sensors. [8, 49, 57] Other advantages of the optical lever method are simplicity, linearity of response, and reliability. But some limitations of this technique are well known, i.e., interference from changes in the optical properties of the surrounding medium around the microcantilever and nonlinear response of the photodetector. Also this technique does not scale well to a large number of microcantilevers in an array. [8, 56] As a result, the number of microcantilevers in an array is limited.

2.5 Functionalization

Microcantilever-based sensors have to be functionalized by depositing or coating a selective or receptor layer directly on one or more surfaces of the microcantilever to achieve selectivity in response. For static mode, interaction between the selective layer and the target analyte which can bind to the selective coating on the microcantilever surface causes a change in the surface stress between the functionalized and non-functionalized surfaces. There are many materials including metals and organic chemical/biological molecules that can be used for the selective layers, the choice of which affects the selectivity, reproducibility, and sensitivity of the microcantilever sensor system.

Metal or ceramic films as selective layer coatings with a high affinity for a specific analyte are used to detect the analyte in ambient air or liquid around the microcantilever. When all surfaces on the microcantilever are deposited by a selective layer, analyte molecules in the medium bind to the selective surfaces and then the concentration of the analyte molecules is directly related to the change in a mass of the microcantilever beam. As a result of the mass

change, the resonant frequency is shifted proportionally to the amount of additional mass. However, if only one surface is functionalized, then static mode measurement can be used since the molecular interaction on the selective surface causes a differential surface stress between the coated and uncoated sides of the microcantilever resulting in static deflection.

Functionalization methods are also important to realize a microcantilever system as a sensor. There are numerous techniques to coat a microcantilever beam with material. First of all, conventional evaporation and sputtering methods are commonly used to deposit metallic or ceramic materials in microfabrication batch processes. These methods are suitable for coating large areas or coating a single side of microcantilever beams, but not individual microcantilevers in an array without complex shadow masking processes. Other simple methods to coat microcantilevers use manual approaches such as pipetting, dropping, and pin-dipping. Disadvantages of these simple methods include scalability to large arrays of microcantilevers, limited reproducibility, and time-consuming. For a microcantilever array, microfluidic network devices can be used to deliver specific solutions to each microcantilever through separate microfluidic channels. [58] A capillary array is another approach to simultaneously coat multiple microcantilevers. A simple array of glass capillaries designed to accommodate the dimensions and pitch of the microcantilevers in a linear array is filled with a variety of solutions containing materials such as polymers, self-assembled monolayers, protein solutions, and single-stranded DNA oligonucleotides. [59] This method involving insertion of the microcantilever array into the capillary array to functionalize microcantilevers. All of above methods for an array use manual alignment of the microcantilever array and functionalization device, and are limited for a large number of microcantilevers. A micro/nano-inkjet printing technique overcomes the disadvantages since it affords efficient, rapid, and reliable functionalization of only one side of

the microcantilevers. By adjusting the size and number of droplets spotted on the microcantilever, the thickness of the selective layer coating can be precisely controlled. [59] The down side is that it is a serial method. Currently, this inkjet printing technique is used to functionalize our SOI photonic microcantilevers.

2.6 Applications

Microcantilever sensing applications have been investigated by numerous researchers. For exampless, microcantilevers coated with gold (Au) on functionalized surfaces have been used to detect the concentration of Mercury in a gaseous medium because of the significant affinity between Au and Mercury molecules. [1] Additionally, artificial nose applications in which many chemicals need to be detected at once, and microcantilevers with polymer or sol-gel coatings for vapor phase analytes [60, 61] have been investigated. Array interesting application is biosensing since microcantilever biosensors could potentially be faster and cheaper compared to typical bioassay sensors. [2] Biological molecules attached to one or more microcantilever surfaces are able to bind selectively with the target molecules to which they have strong affinity.

The following are some examples of biological sensor applications. Baselt et al. [62] showed that it is possible to detect the presence of receptor-coated magnetic particles bound to a microcantilever by functionalizing the microcantilever surface with specific receptors for magnetic particles which is attached an analyte whose counterpart is the receptor on the surface. The deflection of the microcantilever is measured while the magnetic particles amplify the deflection by applying an external magnetic field. Antonik et al. [63] proposed sensing the response of living cells cultured directly on a microcantilever surface to external chemical stimuli. Ilic et al. [64] measured the number of bacteria adsorbed onto an antibody-coated

microcantilever by monitoring changes in its resonant frequency. The detection of prostate-specific antigen over a wide range of concentrations was reported as a diagnostic assay using microcantilevers by Wu et al. [4]. Using the antibody-antigen interaction of biotin and streptavidin, Raiteri et al. [32] show that the specific binding causes a microcantilever to bend.

Microcantilever based sensors have also been applied to genomics research. Fritz et al. [3] used a microcantilever array to detect single-stranded DNA (ssDNA) hybridization. They were able to discriminate a single mismatch between two 12mer oligonucleotides. Other researchers also reported DNA-based sensing experiments [65, 66] with microcantilever sensor systems.

From these bioanalytic measurements, we can conclude that microcantilever biosensors are promising tools for a new class of miniaturized sensor systems. High sensitivity, versatility, label-free, and reproducibility are required for a high-end sensor system in biotechnology and nanotechnology. In order to improve performance of microcantilever based sensor system for applications such as clinical diagnostics, further research and development are ongoing.

3 IN-PLANE PHOTONIC TRANSDUCTION FOR SOI MICROCANTILEVERS

An in-plane photonic transduction method utilizes a differential splitter consisting of an asymmetrical amorphous silicon strip-loaded multimode rib waveguide and a Y-branch splitter to transduce the deflection of a photonic waveguide microcantilever, which itself forms a single mode rib waveguide, into an optical signal. [67-69] In this chapter I introduce the transduction method and present a first generation design and experimental measurement. In order to optimize sensitivity and fidelity of the in-plane photonic transduction method for silicon-on-insulator (SOI) microcantilevers, we first do a design analysis based on computer simulations, and then an integrated photonic circuit to experimentally demonstrate the proposed transduction method.

3.1 Optical Waveguide Transduction Method

A number of groups have proposed measuring microcantilever properties by turning the microcantilever into a waveguide and capturing light with a static single mode waveguide that is fixed across a small gap from the free end of the microcantilever [57, 70, 71]. To illustrate the advantages and disadvantages inherent in this approach, consider the photonic microcantilever geometry in Figure 3-1(a) in which a silicon microcantilever is etched to form a single mode rib waveguide. The waveguide cross section is shown in Figure 3-1(b) and supports a single transverse electric (TE) mode (i.e., electric field polarized in the plane of the silicon layer) at a wavelength of 1550 nm. The optical power captured in the static waveguide is shown in Figure 3-1(c) as a function of vertical deflection of the photonic microcantilever.

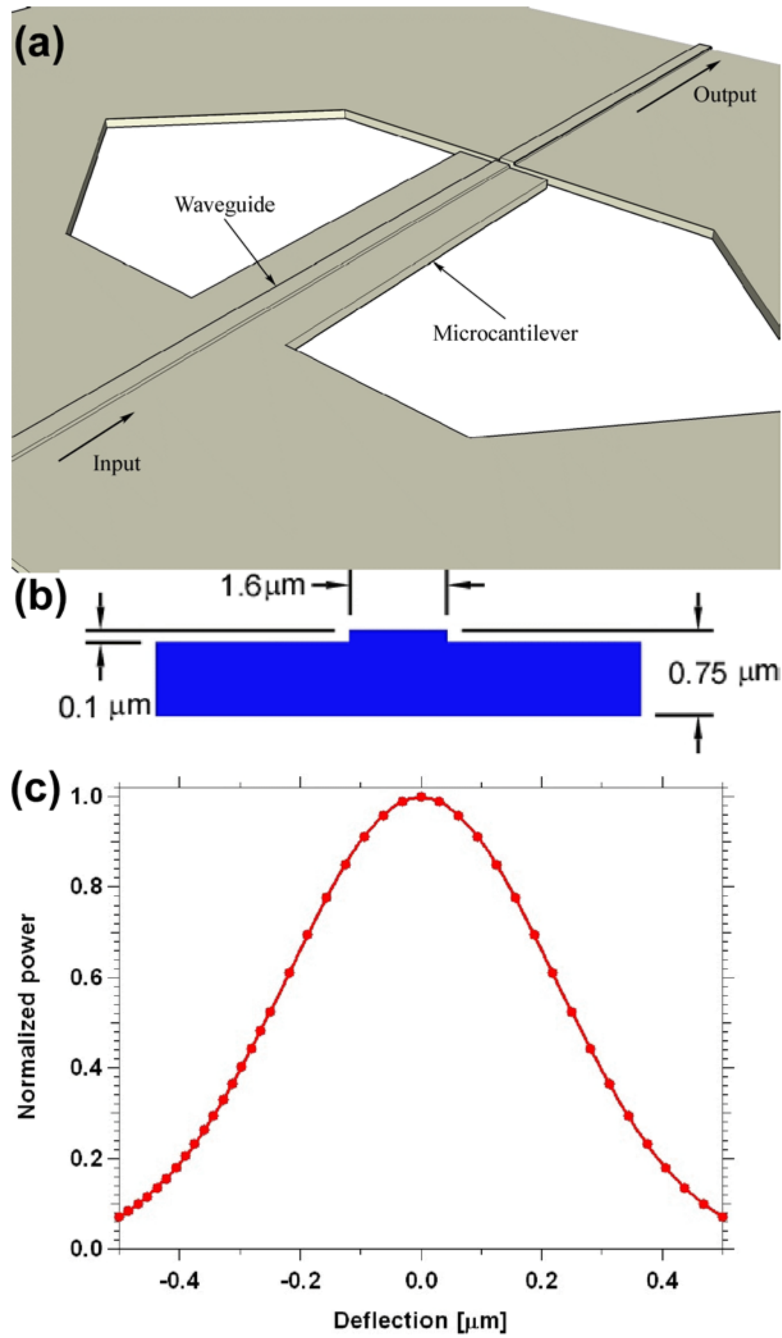

Figure 3-1: (a) Schematic layout of photonic microcantilever with single mode receiver waveguide (b) Waveguide cross section (c) Simulation result for the normalized power in the output waveguide as a function of microcantilever deflection. Simulations are performed with FIMMWAVE/PROP by Photon Design.

Note that near zero deflection there is very little change in the output power since the slope in this region is small. Hence this approach suffers from lack of sensitivity in the middle of

the measurement range. If, however, one could bias the operating point to a deflection of, say, 0.2 μm, and operate in a range of approximately ±0.15 μm around this deflection, then this approach offers the advantage of use of simple waveguides.

3.2 Photonic Waveguide Microcantilever Design

A new in-plane photonic microcantilever transduction mechanism based on an asymmetric multimode static receiver waveguide is designed for silicon photonic devices. A single mode rib waveguide embedded in a microcantilever and an asymmetrical amorphous silicon strip-loaded multimode rib waveguide are key elements in this transduction method. The structure of a single mode rib waveguide remains the same as shown in Figure 3-1(b). Figure 3-2(a) shows a schematic diagram of the microcantilever and waveguide geometry. The receiver waveguide consists of a 3.0 μm wide etched rib in the silicon layer and a 0.1 μm thick amorphous silicon strip loading that is 1.5 μm wide and is placed over half of the etched rib as shown in Figure 3-2(b). This asymmetric multimode section supports two TE waveguide modes and terminates in a Y-branch 1×2 optical power splitter. We use a commercial simulation tool, FIMMWAVE/PROP (Photon Design, Ltd), to evaluate performance of the photonic microcantilever system.

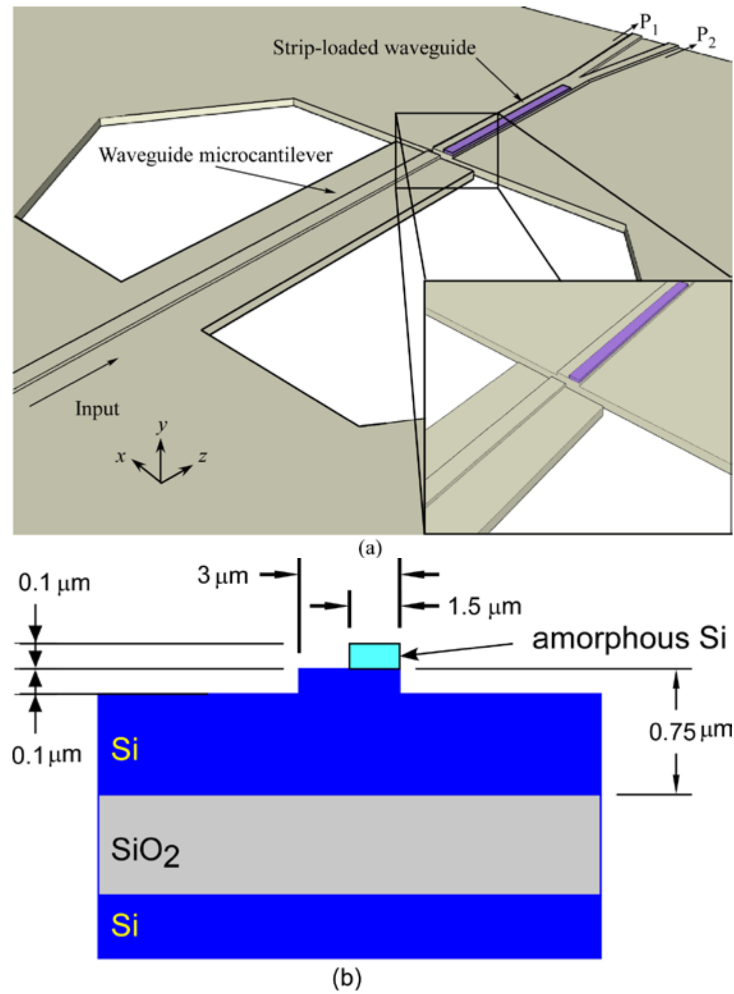

Figure 3-2: (a) Schematic 3-D layout of the photonic microcantilever system with the in-plane photonic transduction method (b) asymmetric amorphous silicon strip-loaded multimode waveguide

The top-view layout for the photonic simulation is shown in Figure 3-3. The lengths of the input single mode rib waveguide, strip-loaded multimode rib waveguide, and Y-branch splitter are 20 µm, 100 µm, and 200 µm, respectively.

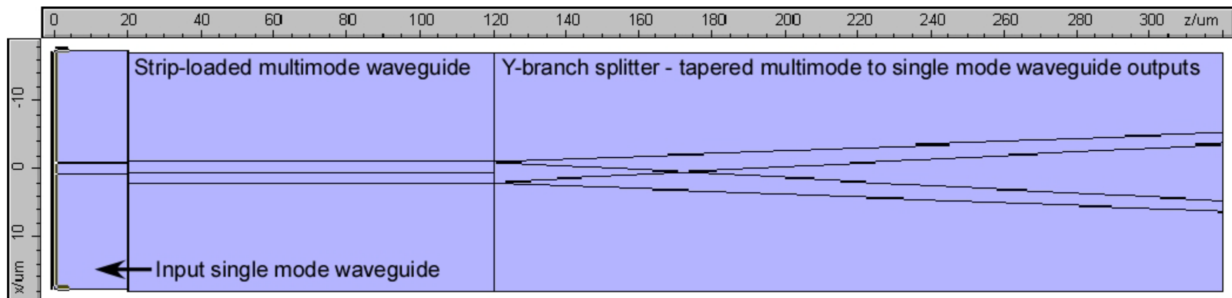

Figure 3-3: Top view of waveguide device layout for photonic simulation

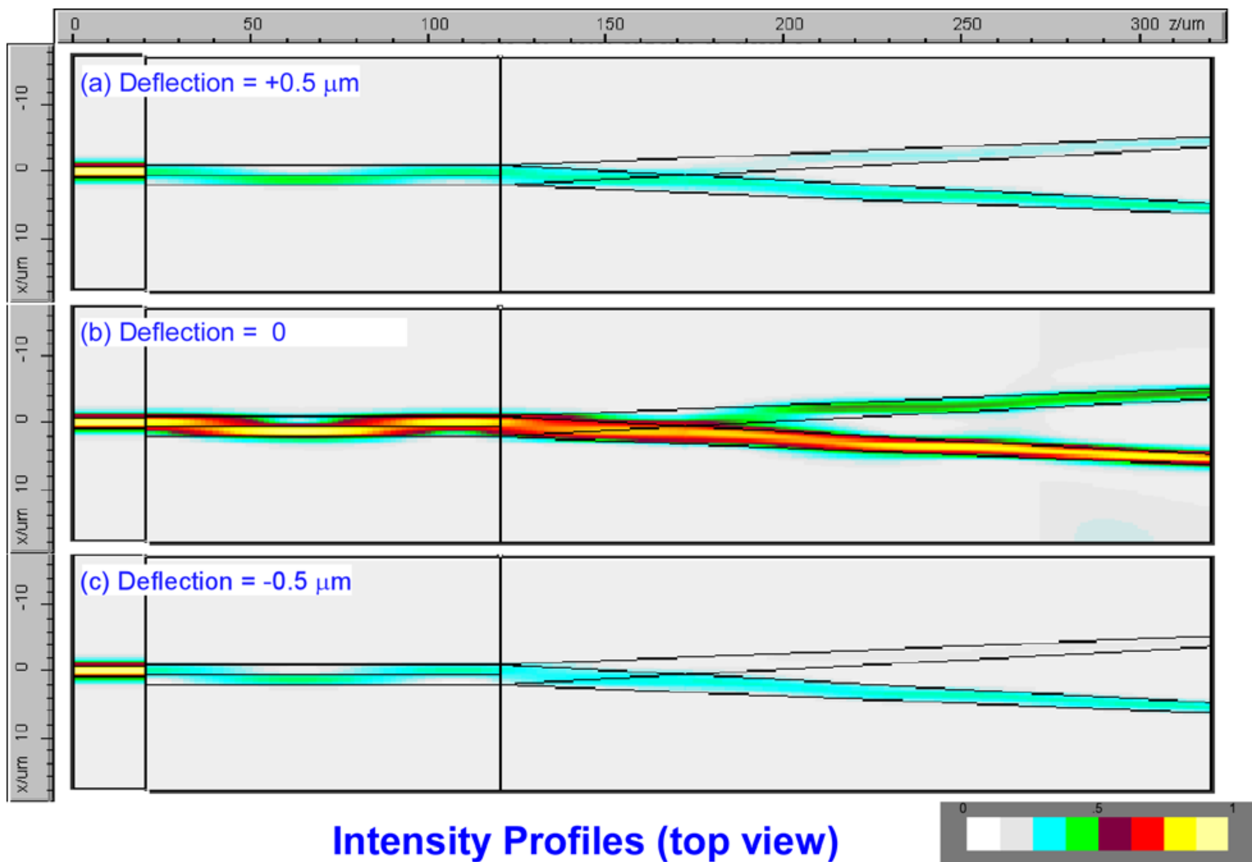

Figure 3-4: Intensity profiles (top view) of that (a) upward deflection (+0.5 μm), (b) zero-deflection (0), and (c) downward deflection (-0.5 μm) cases of the input waveguide microcantilever.

Figure 3-4 shows intensity profiles of three different cases of the microcantilever deflection. As shown in Figure 3-4(a) and Figure 3-4(c), the intensity profile at the output,

especially P_1 (the upper waveguide of the Y-branch), is different between the upward and downward deflection cases, even though the magnitude of deflection is the same. Hence, the optical field distribution into P_1 and P_2 of a differential splitter is a function of microcantilever deflection.

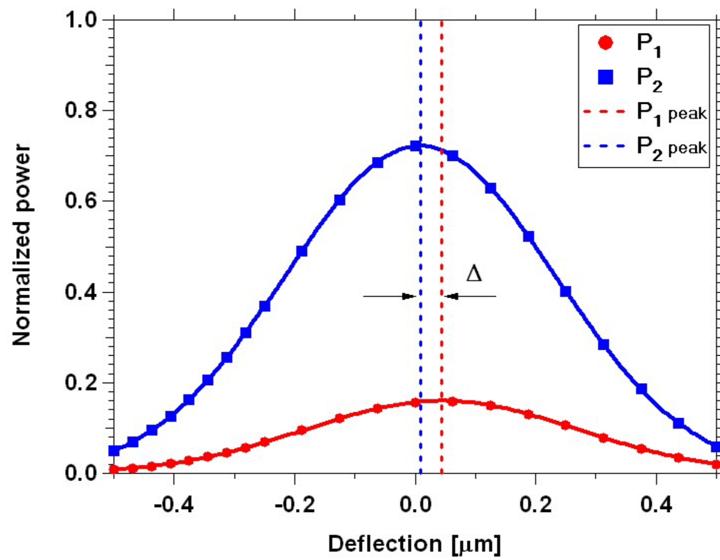

Figure 3-5: Simulation results for output power as a function of microcantilever deflection.

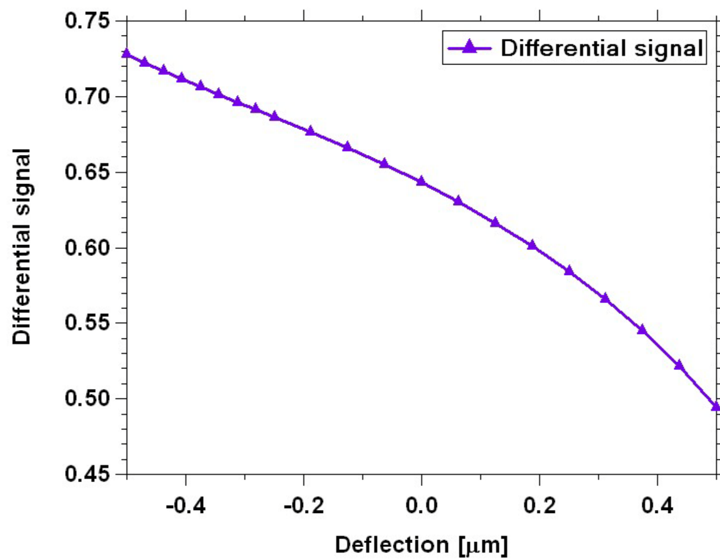

Figure 3-6: Differential signal as a function of the deflection of the input waveguide microcantilever

The output power as a function of microcantilever deflection is shown in Figure 3-5. Note that the individual output power profiles are each Gaussian-like similar to what is observed for a single mode receiver waveguide as shown in Figure 3-1(c). However, there is a small offset, Δ (0.035 μm), between the peaks of P1 and P2 in Figure 3-5. This is significant because we can define a differential signal, η, as

$$\eta = \frac{P_2 - P_1}{P_2 + P_1}, \qquad \textbf{(3.1)}$$

which is monotonically dependent on microcantilever deflection as shown in Figure 3-6. Note that it is a monotonic function of deflection and hence the lack of sensitivity in the middle of the measurement range seen in Figure 3-1(c) is avoided. For ±0.5 μm deflection, the contrast, κ, of the differential signal (i.e., the difference between the differential signal values at the endpoints of the measurement range, -0.5 μm and 0.5 μm, $\kappa = \eta_{-0.5} - \eta_{+0.5}$) is 0.23. Naturally, we want to maximize κ in order to have the largest possible signal range.

We perform photonic simulations to optimize the design of the amorphous silicon strip-loaded multimode rib waveguide-based differential splitter for better performance. Figure 3-7 shows output power P_1 and P_2 curves as a function of the length of the amorphous silicon strip-loaded waveguide and the contrasts for several arbitrarily chosen lengths. In order to see the effects of the strip-loaded waveguide length on the output and contrast, we monitor output signals from the differential splitter as a function of the length. As shown in Figure 3-7(a), output signals oscillate as a function of the strip-loaded waveguide length. Contrasts for several strip-loaded waveguide lengths are shown in Figure 3-7(b). Note that there is a variation in the contrast. The 100 μm length case shows the largest contrast among the chosen lengths.

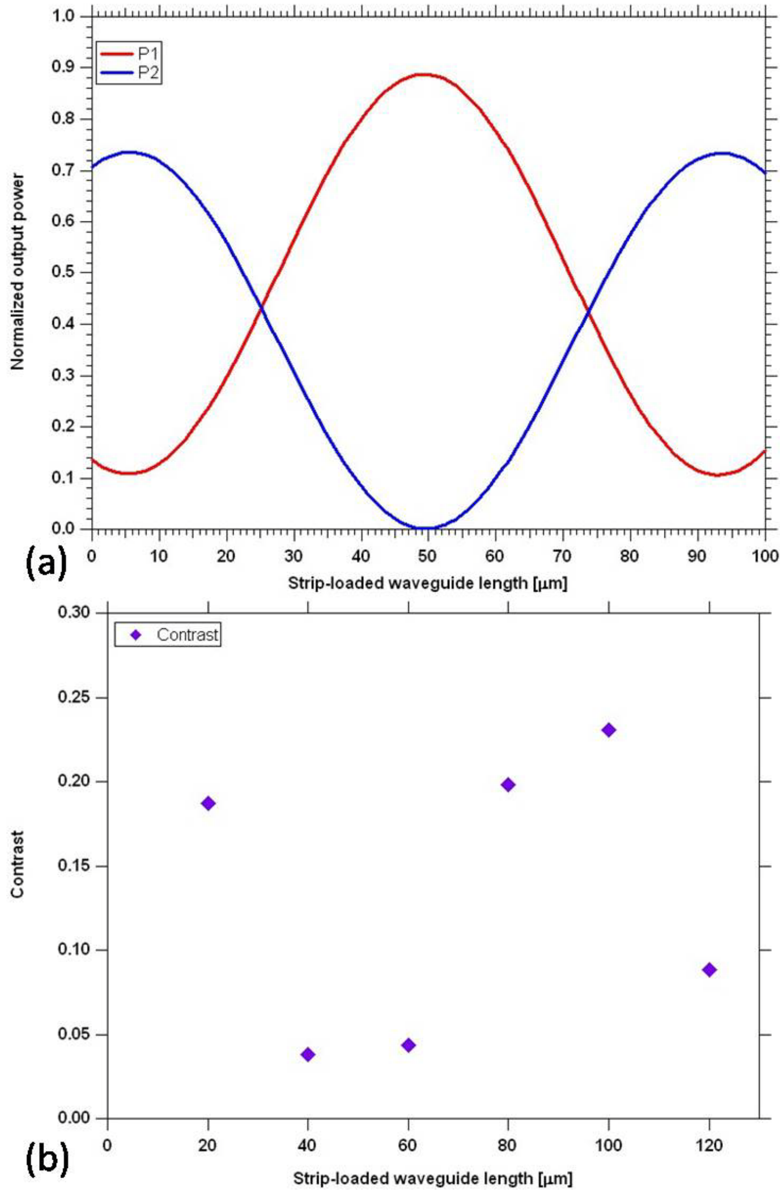

Figure 3-7: (a) Optical power in each output and (b) contrast of the differential signal for arbitrarily chosen lengths as a function of the length of the strip-loaded multimode rib waveguide.

Another parameter of interest is the thickness of an amorphous silicon strip. The refractive index of amorphous silicon, which is deposited by a sputtering system, is 3.0. To perform photonic simulations, the length of an amorphous silicon strip-loaded multimode rib waveguide is chosen to be 100 mm long. Figure 3-8 shows the contrast as a function of the

thickness of an amorphous silicon strip. This result indicates that thicker is slightly better. However, the contrast is not a strong function of the thickness in the range of 100 nm to 200 nm since the difference of the contrast values is only 0.01 between the 100 nm and 200 nm thickness cases. Since the amorphous silicon strip loading will be patterned with a lift-off technique which is easier for thin films, we choose a thickness of 100 nm.

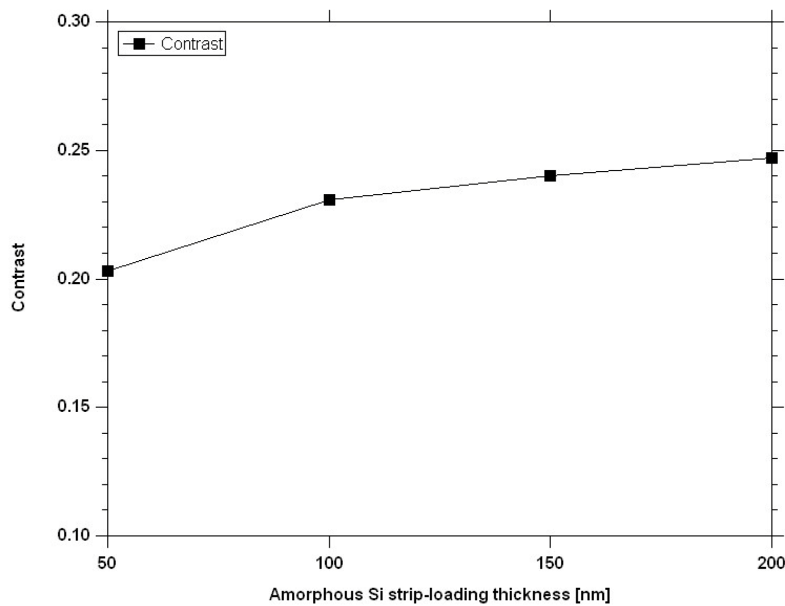

Figure 3-8: Simulation results of the contrast of the differential signal as a function of the thickness of the amorphous silicon strip-loading on the multimode receiver waveguide for four different thickness cases for an asymmetric multimode rib waveguide length of 100 μm.

The center-to-center horizontal offset between the input single mode and amorphous silicon strip-loaded multimode rib waveguides is also considered as a design parameter. The optical power in each output as a function of horizontal offset of the waveguide microcantilever is shown in Figure 3-9, which illustrates this effect for zero deflection. We calculate the contrast κ of the differential signal for arbitrarily chosen offsets and append to Figure 3-9. The contrast of

the -0.5 μm offset case is greater than that of the +0.5 μm case (i.e., the minus direction is toward P_1 (upper output) shown in Figure 3-3).

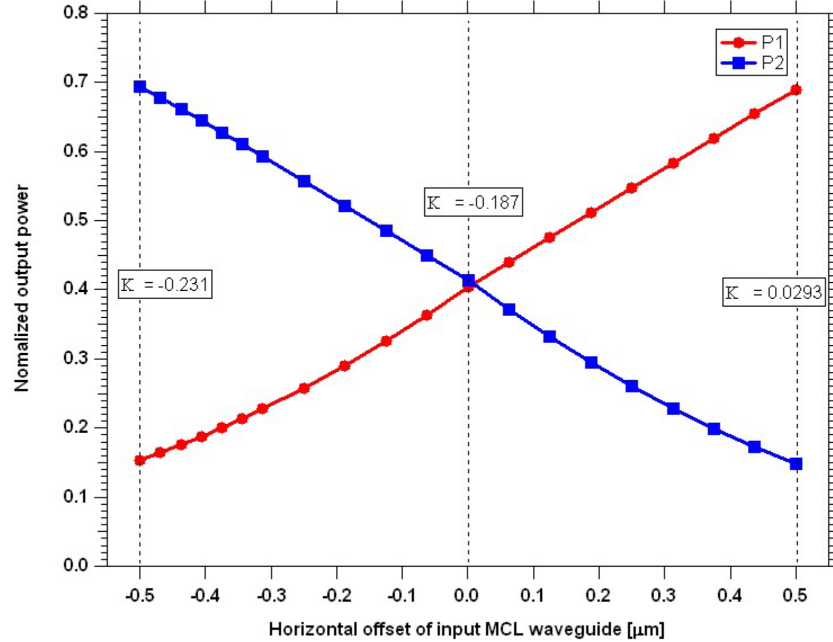

Figure 3-9: (a) Optical power in output as a function of the length of the strip-loaded waveguide, (b) contrast of the differential signal in the selected length of the strip-loaded waveguide

On the basis of the above simulation results, we choose as an initial design a 100 μm long amorphous silicon strip-loaded multimode rib waveguide, a 100 nm thick amorphous silicon strip, and a minus half micrometer offset of the input waveguide. Simulation results based on these parameters are shown in Figure 3-6, and in which we expect to achieve a contrast of 0.23.

We now turn to a brief examination of the optical properties of the waveguides to understand the role of a differential splitter for in-plane photonic transduction. The single mode rib waveguide embedded in the microcantilever guides only a fundamental mode, while the asymmetric amorphous silicon strip-loaded waveguide supports two guided modes, the

fundamental and first order modes. The intensity profiles of the guided modes are shown in Figure 3-10.

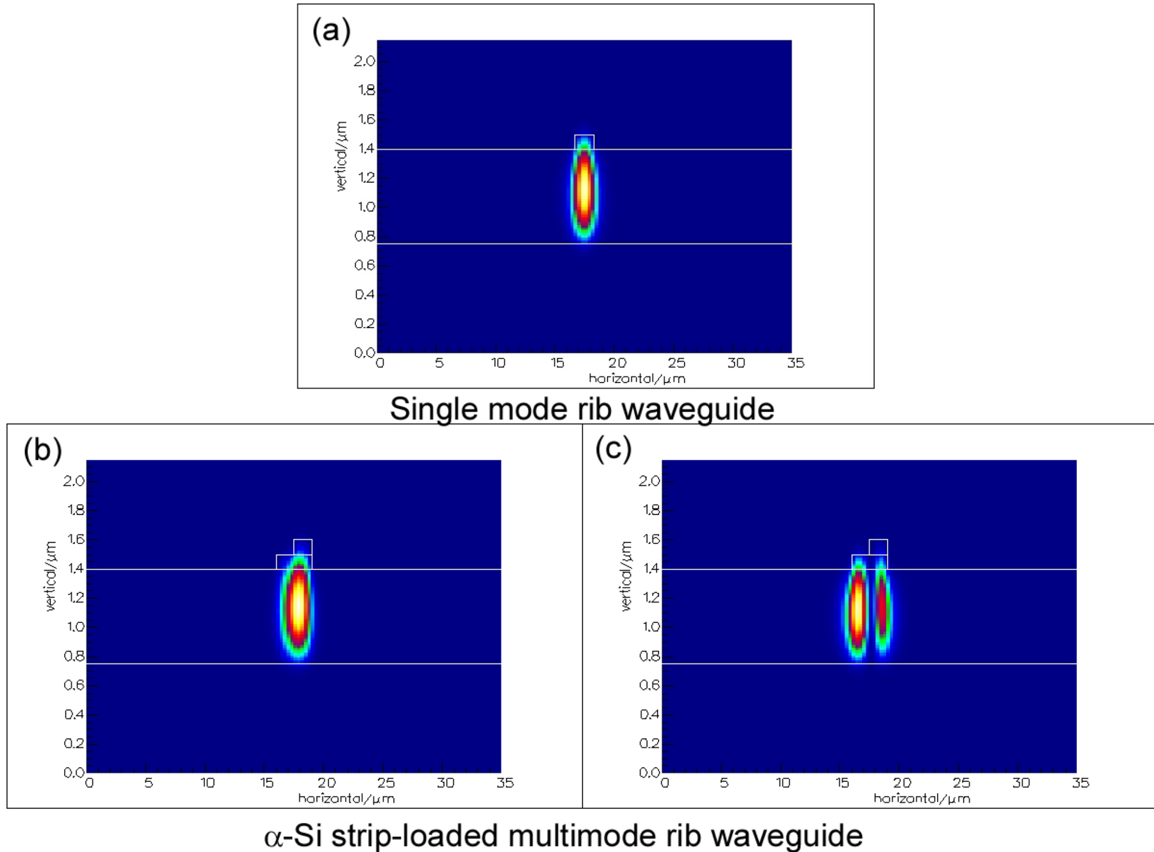

Figure 3-10: (a) Intensity profile of the fundamental TE (transverse electric) mode of the single mode rib waveguide. The asymmetric amorphous silicon strip-loaded multimode rib waveguide guides two TE modes, the (b) fundamental and (c) first order modes.

Coupling based on mode overlap integrals between the incident mode exiting the single mode rib waveguide into the two guided modes of the strip-loaded waveguide as a function of deflection is shown in Figure 3-11 (dashed lines indicate the maximum mode coupling position.). The curves of the mode coupling are Gaussian-like, and there is a lateral separation between the maximum mode coupling into the fundamental and first order.

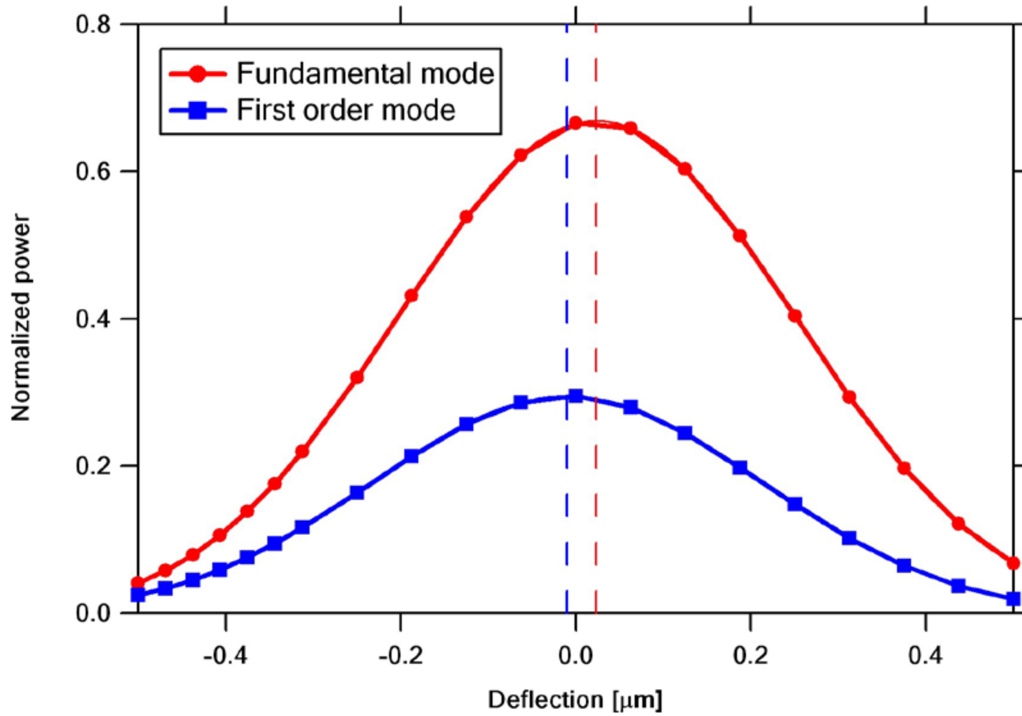

Figure 3-11: The mode coupling between the incident mode and two guided modes as a function of deflection. Dashed lines show the maximum mode coupling deflection position.

The lateral separation of the mode coupling is related to the difference in the mode shape between the guided modes. Output powers, P_1 and P_2, from the differential splitter correlate with the mode coupling. Hence, the maxima separation of the mode coupling affects the differential signal which is formed by the differential splitter outputs. Therefore, our in-plane photonic transduction mechanism utilizing a differential signal is based on the asymmetric structure of the amorphous silicon strip-loaded rib waveguide. The relationship between the waveguide structure and differential signal is examined in detail in Chapter 5.

3.3 Design and Fabrication of Photonic Microcantilever System

For demonstration of the in-plane photonic transduction method for SOI photonic microcantilevers, we design a single microcantilever set. The layout is illustrated in Figure 3-12.

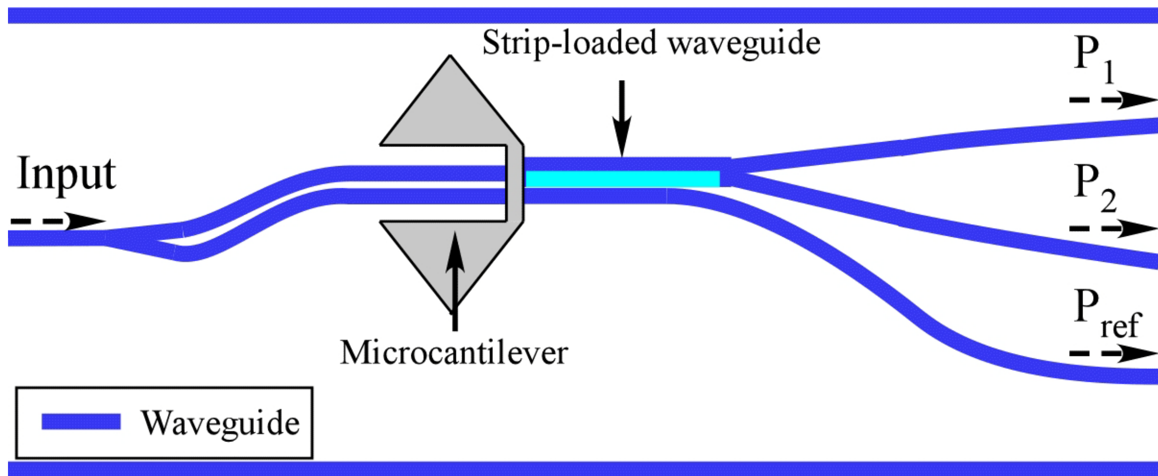

Figure 3-12: Single set of a photonic microcantilever system

One single mode input waveguide is divided by a 1x2 Y-branch splitter into two single mode waveguides, and these waveguides extend to the end of the microcantilever. The microcantilever is 100 μm long and 35 μm wide, and the two waveguides in the microcantilever are 18 μm apart. The upper waveguide sources light into our differential splitter structure while the lower one is coupled into a single mode static waveguide. The purpose of the lower waveguide, which is the same situation as described in Section 3.1, is to allow us to determine zero deflection for the microcantilever. The multimode capture waveguide is terminated by two tapered multi- to single mode waveguides. S-bend structures were designed and inserted to create

250 μm separation between the 3 output waveguides so that their outputs can be measured simultaneously with a butt-coupled fiber array mounted in a fiber block. Specific design parameters of the S-bend and the tapered multimode to single mode waveguide sections are shown in Figure 3-13.

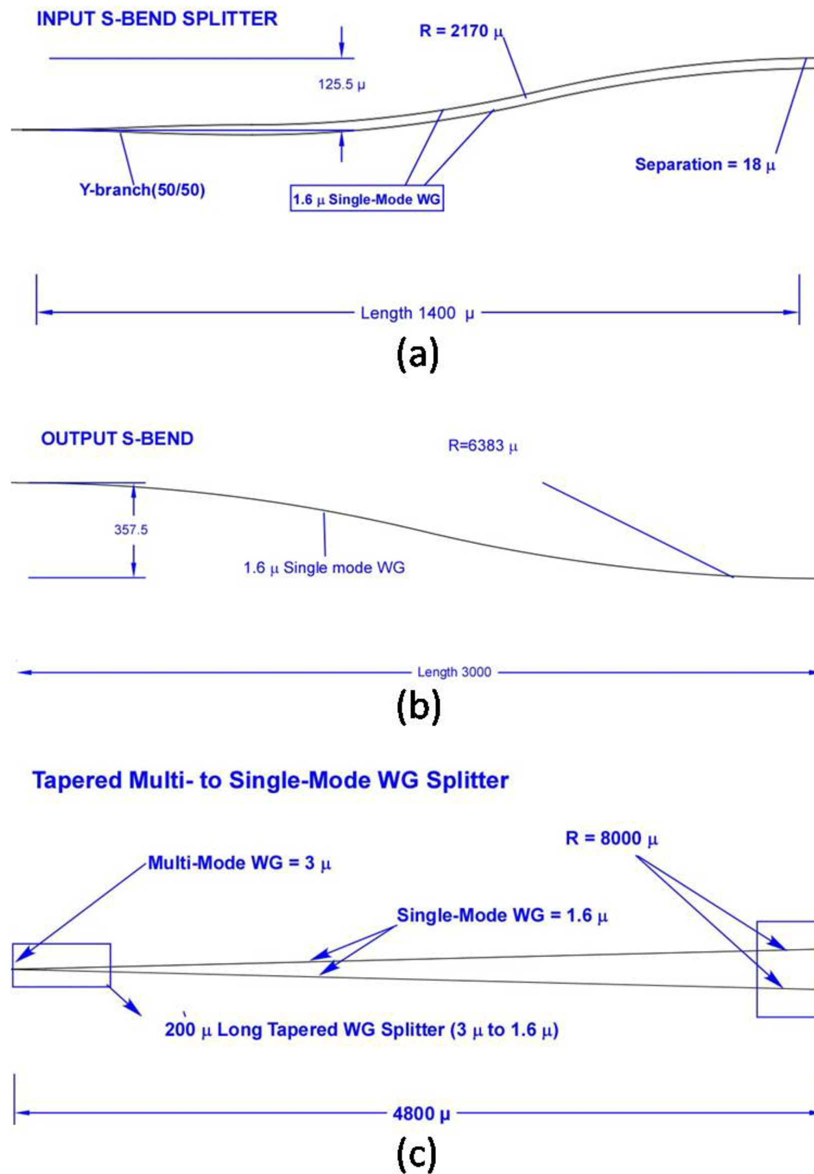

Figure 3-13: Design parameters for (a) input waveguide splitter with S-bend structures, (b) S-bend in the output single mode waveguide, (c) the tapered multi- to single-mode waveguide section

We fabricated 1 cm^2 chips with eight copies of the photonic microcantilever set shown in Figure 3-14. Fabrication starts with a 100 mm SOI wafer that has a 0.75 μm single crystal silicon layer and a 3 μm buried oxide layer.

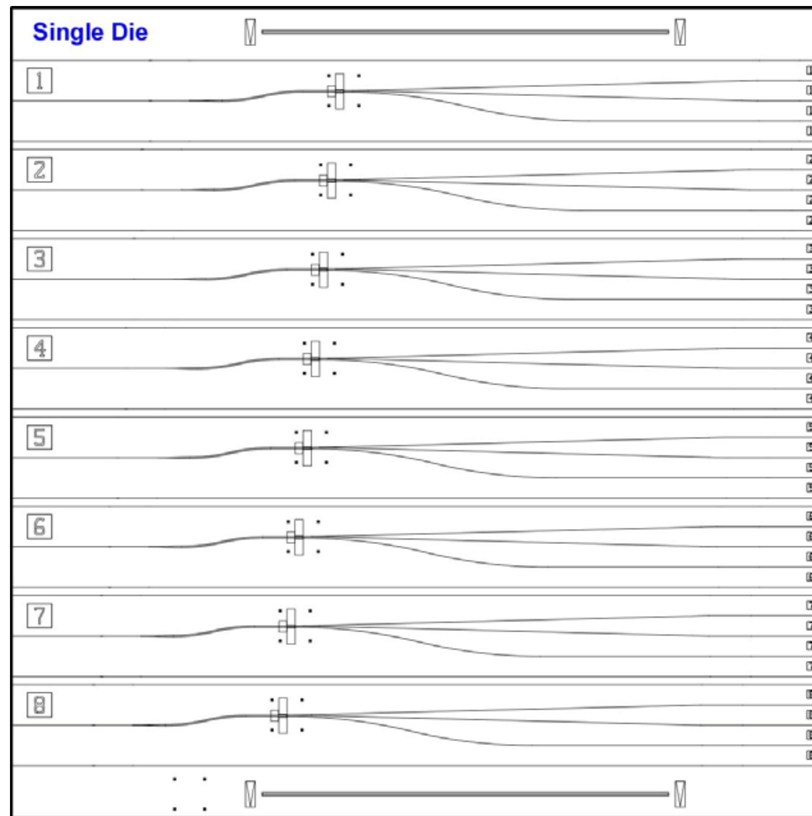

Figure 3-14: Schematic layout of a 1 cm^2 die which has 8 copies of a single microcantilever set

Fabrication is divided by two categories, wafer-based processes and individual die-based processes. In the wafer-based process, waveguides and cantilevers are defined in separate photolithography steps in a contact mask aligner, each of which is followed by a silicon etch in an inductively coupled plasma reactive ion etcher (ICP RIE) (Surface Technology Systems). After all wafer based processes are performed, the wafer is diced into discrete die. An individual

die is further processed by patterning a 300 nm gap at the end of the microcantilever to form its free end. This is done by electron-beam-lithography (EBL) with a Nanometer Pattern Generation System (JC Nabity NPGS) and field emission environmental scanning electron microscope (FEI/Philips XL30 ESEM-FEG) using alignment marks that are patterned in the same step as the waveguides. After anisotropic etching of the gap and stripping of the e-beam resist, a further EBL step is done to define the strip loading on the multimode waveguide, followed by sputtering of amorphous silicon and lift-off. Etching in hydrofluoric (HF) acid followed by critical point drying (Tousimis Autosamdri 815B) is used to remove the buried oxide and release the microcantilevers. Figure 3-15 shows a fabrication process flow of the wafer-based steps. The individual die-based fabrication flow chart is illustrated in Figure 3-16.

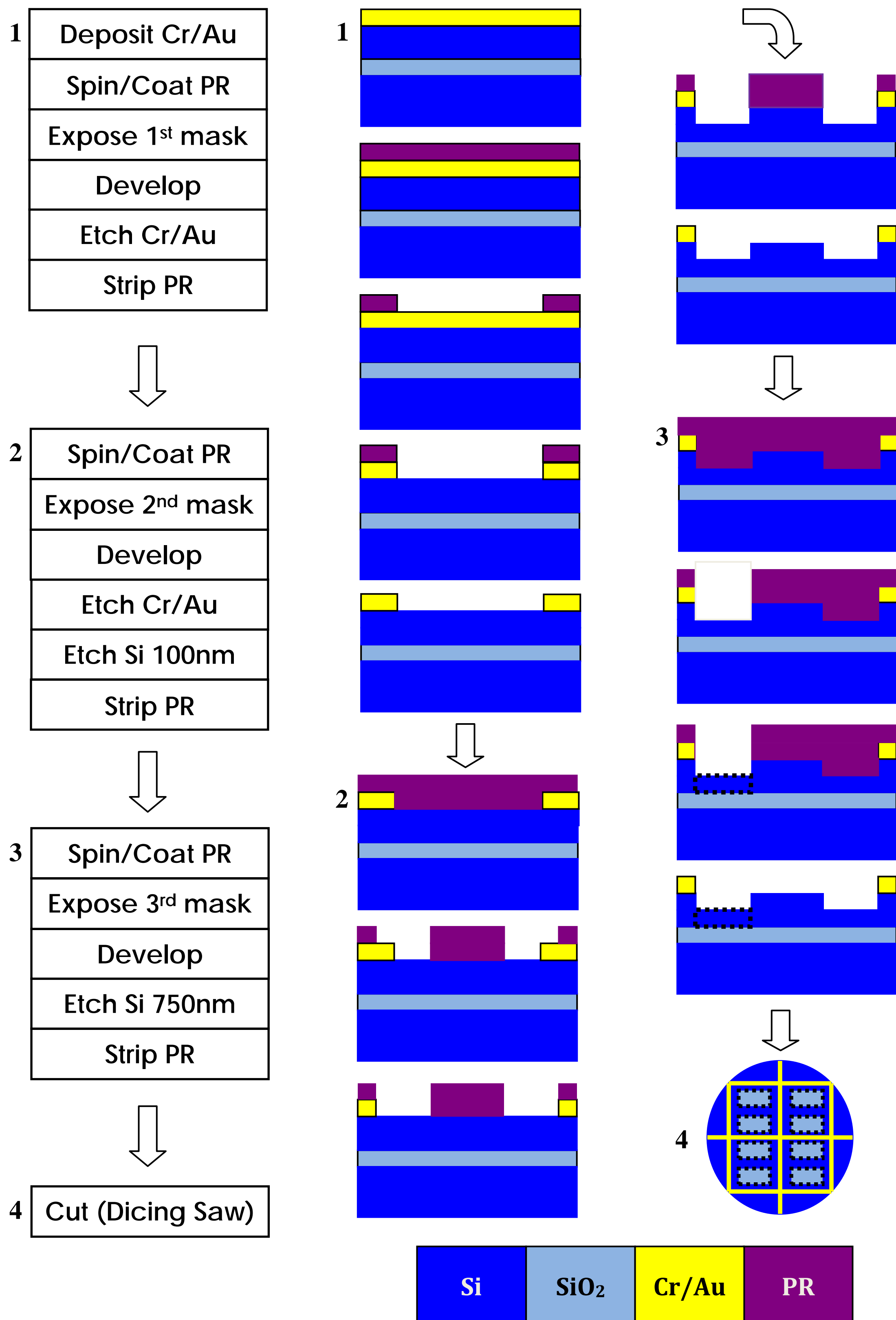

Figure 3-15: Fabrication flow chart for wafer based process

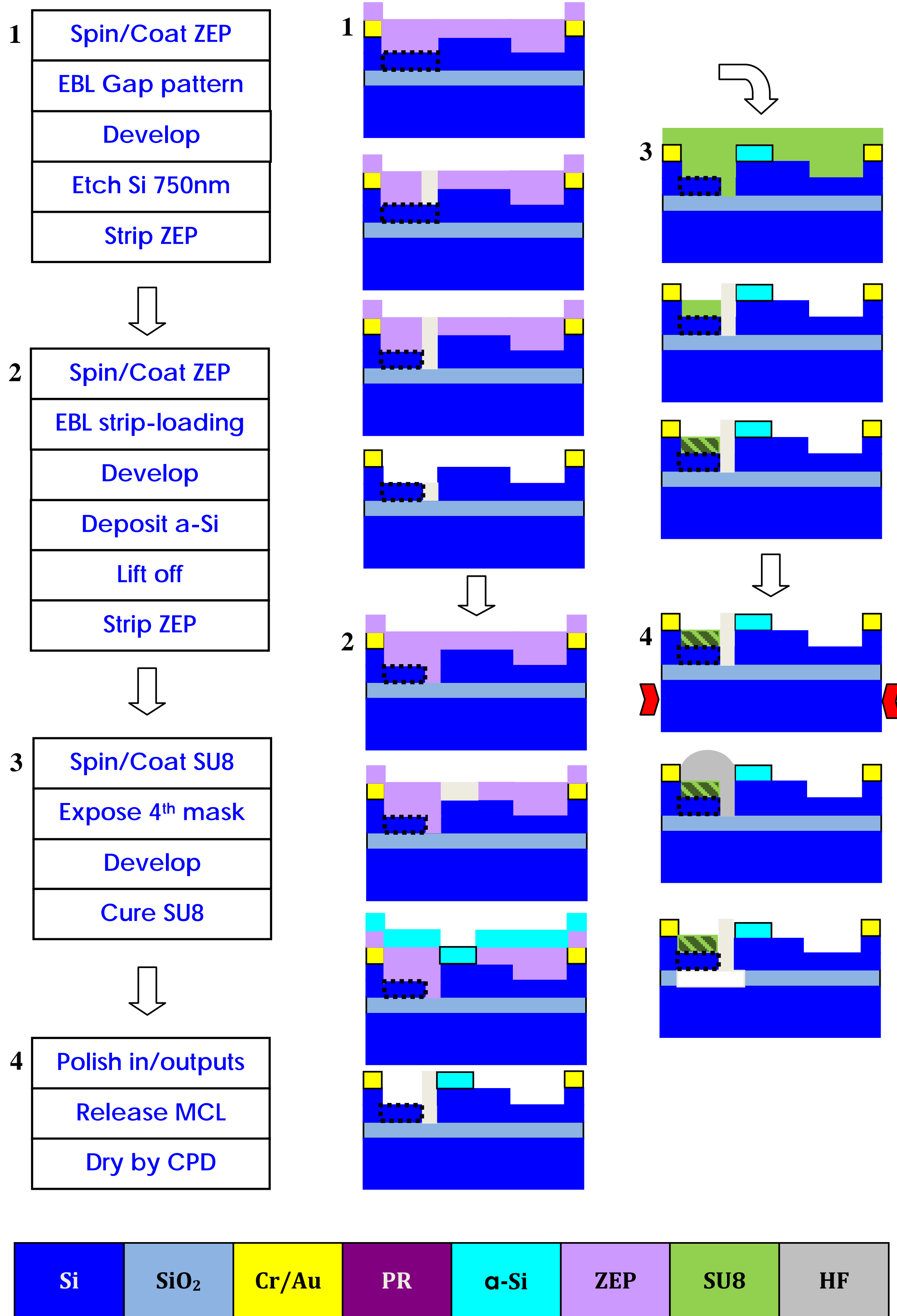

Figure 3-16: Fabrication flow chart for individual die based process

Figure 3-17 shows a fabricated photonic microcantilever: (a) a microscope image of a waveguide microcantilever before starting individual die-based fabrication and SEM images (b) through (d) of the microcantilever fully released after the HF release process. A close-up of the gap region is shown in Figure 3-17(d) in which placement of the strip loading can be clearly seen.

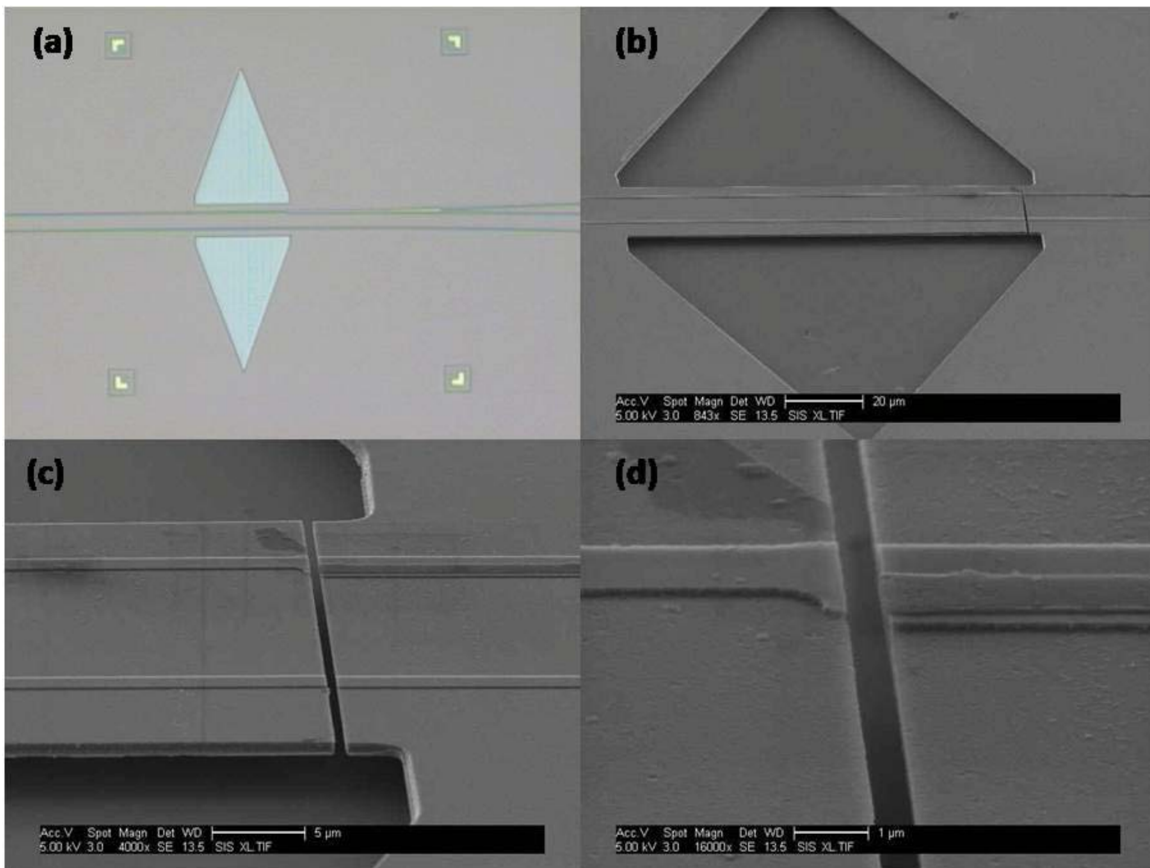

Figure 3-17: (a) Microscope image of a waveguide microcantilever fabricated on a SOI wafer, SEM images of (b) after releasing the microcantilever, (b) close up of microcantilever and strip-loaded multimode receiving waveguide, and (d) close up of a gap.

3.4 Experimental Measurement

To measure the differential signal as a function of microcantilever deflection, we pattern an SU-8 polymer layer on the top of the microcantilever, and heat-treat it to deflect the microcantilever due to tensile stress induced by thermally driven epoxy cross-linking. As shown in Figure 3-18, a sharp probe tip located on the end of the piezoactuator (Physik Instrumente, Germany) makes physical contact with the microcantilever such that vertical displacement of the microcantilever tip can be accurately controlled by pushing down on the microcantilever.

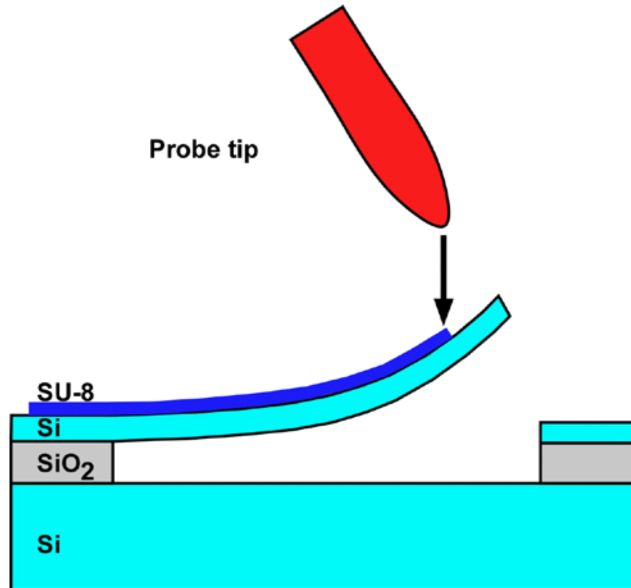

Figure 3-18: Schematic of the experimental set-up using thermally treated SU-8 to bend the cantilever beam up.

Figure 3-19 shows an SEM image of a microcantilever bent up by a stressed SU-8 film. The amount of the initial deflection is controlled by the temperature at which the film is cured. In our samples this is typically 6-10 μm. A top-view CCD image of a probe tip pushing down a microcantilever is shown in Figure 3-20.

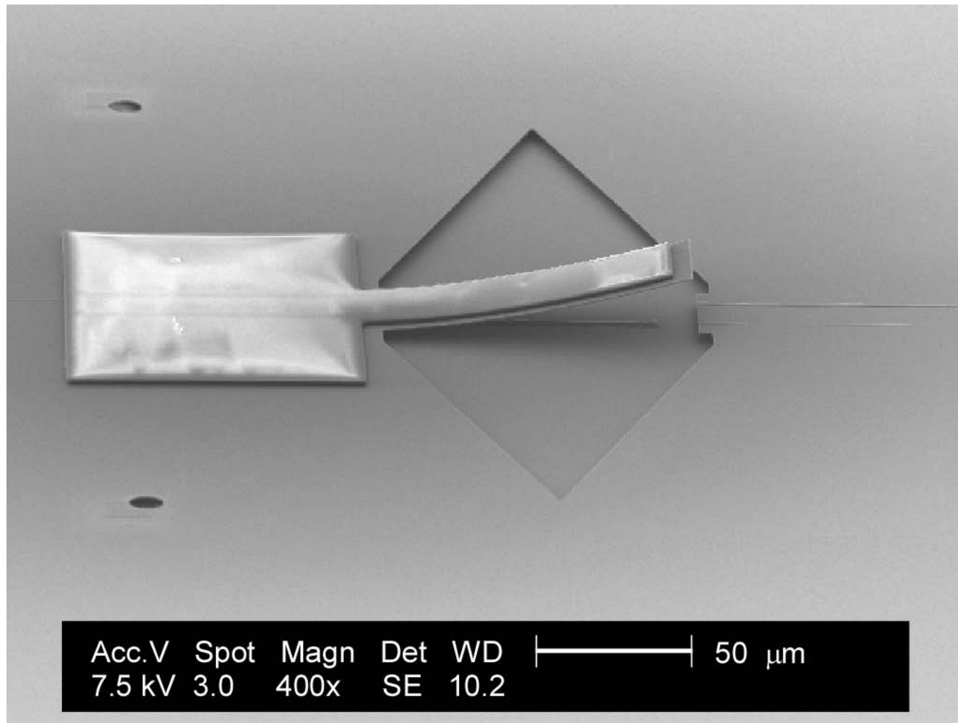

Figure 3-19: SEM image of a cantilever beam bent up by a stressed SU-8 patch.

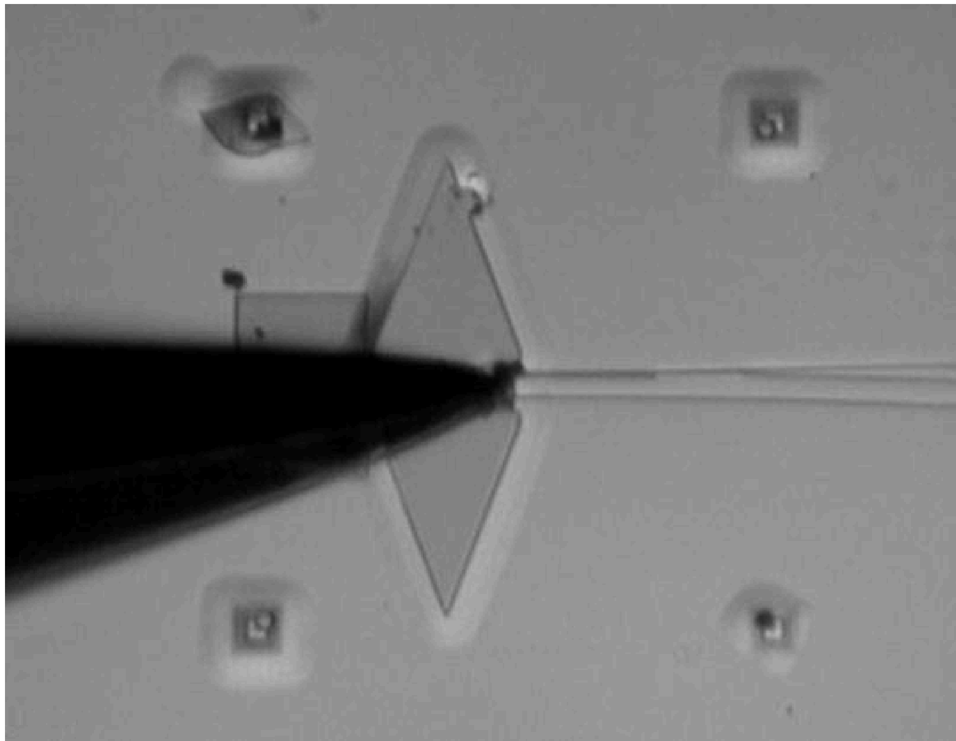

Figure 3-20: CCD camera image during an experiment to demonstrate the photonic waveguide microcantilever transduction mechanism.

Light from a fiber-coupled super luminescent light emitting diode (SLD) with a center wavelength of 1550 nm is amplified by an erbium-doped fiber amplifier (EDFA) and propagated through a polarization controller paddle to create TE polarized light at the end of the fiber. The TE polarized light is then butt-coupled to the chip. An optical fiber array block is used to simultaneously collect the three optical output powers (P_1, P_2, and P_{ref}) which are directed to individual photodetectors (PDA10CS, Thorlabs) that are sampled at 5 kHz by a computer-controlled data acquisition card (NI BNC-2110, National Instruments). The total piezoactuator scan distance for a measurement is 3 μm with a step increment of 50 nm. At each position, 100 data points are recorded and averaged.

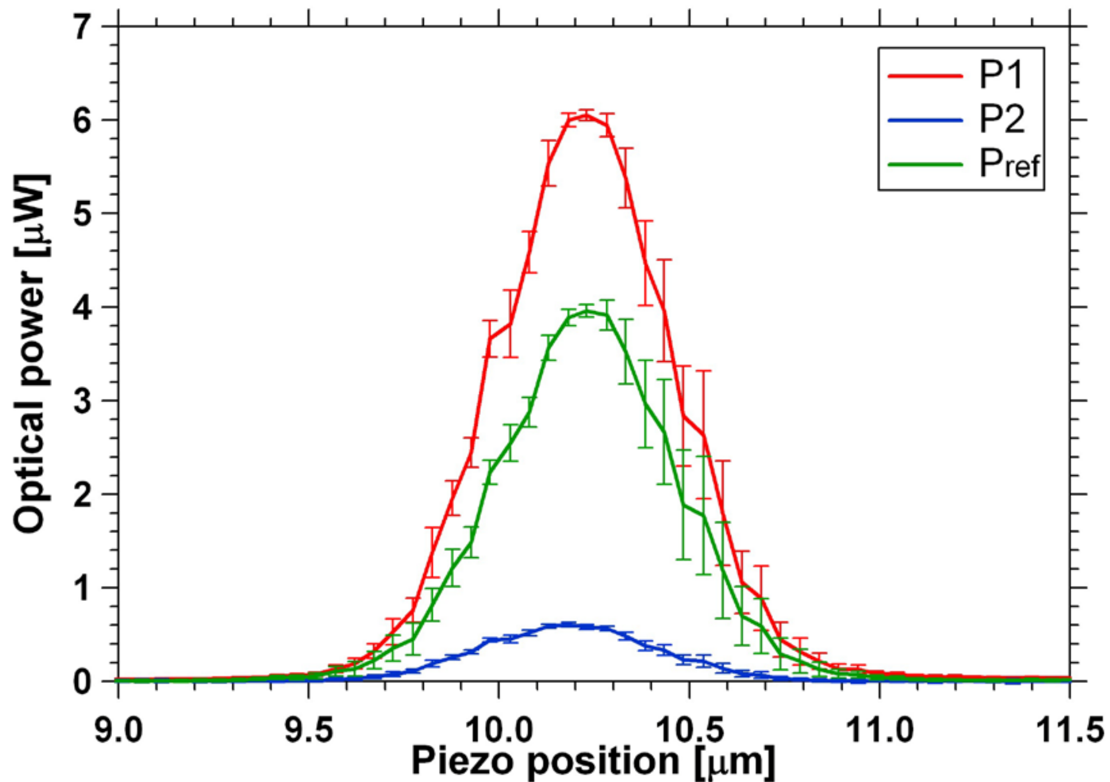

Figure 3-21: Measured output power as a function of piezoactuator position.

Figure 3-21 shows the measured optical power for the three outputs as a function of piezoactuator position. The position of the peak of P_1 is coincident with that of P_{ref}, and P_2 has an offset as expected. To determine the actual deflection of the microcantilever, the piezoactuator position is converted to microcantilever position based on the contact point of the probe tip and knowing that the peak of P_{ref} occurs at zero deflection. The result is shown in Figure 3-22 in which P_1 and P_2 are plotted as a function of microcantilever deflection. Gaussian curve fits are also shown.

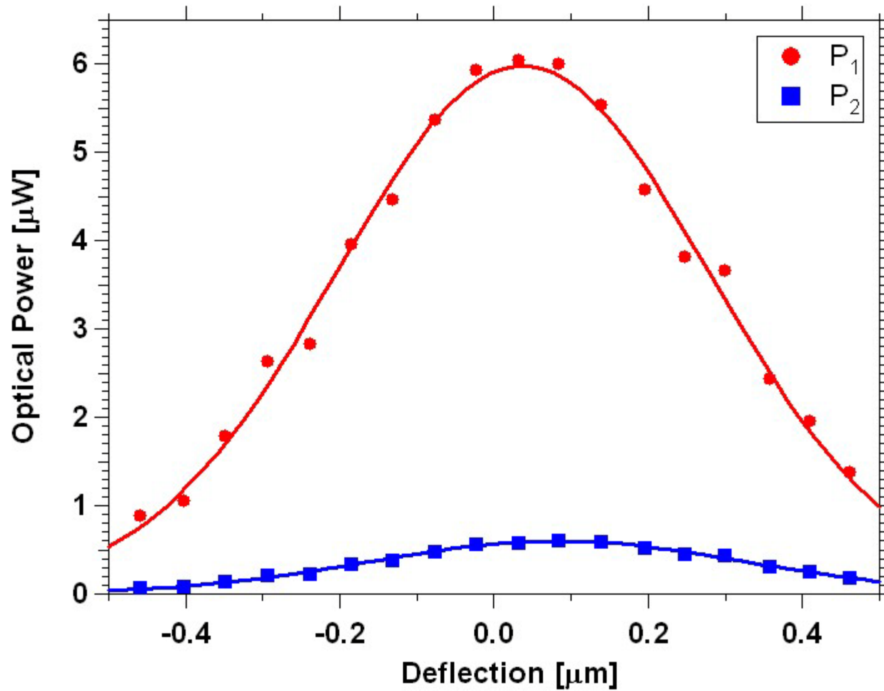

Figure 3-22: P_1 and P_2 as a function of deflection of the microcantilever converted from the piezoactuator position

3.5 Analysis and Discussion

There are a number of differences between the experimental measurement in Figure 3-22 and the initial simulation result in the Figure 3-5. For example, the ratio of the peak value of P_1 to P_2, P_1/P_2, in Figure 3-5 is approximately 0.16/0.72 = 0.22, whereas it is (6.0 μW)/(0.58 μW) = 10 for the experimental data. Note that there are a number of possible causes for this difference. These include quality of the polished output facet and the concomitant effect on coupling efficiency into the two output fibers, different defects in the waveguides between the Y-branch and the output facet, and the fact that the fibers in the fiber block have a 1 μm center-to-center spacing tolerance that affects the individual fiber coupling efficiency.

There is another difference between measurement and simulation that is more significant. In Figure 3-5 the position of the peak of P_1 relative to the peak of P_2, Δ, is 0.035 μm, whereas it is -0.045 μm for the experimental data. Note that the sign as well as the magnitude of the offset is different. Through a combination of experimental investigation and simulation, it is clear that the difference is due to a rotation of the microcantilever about its long axis which is caused by the probe tip contacting the cantilever at a position off of the centerline of the microcantilever.

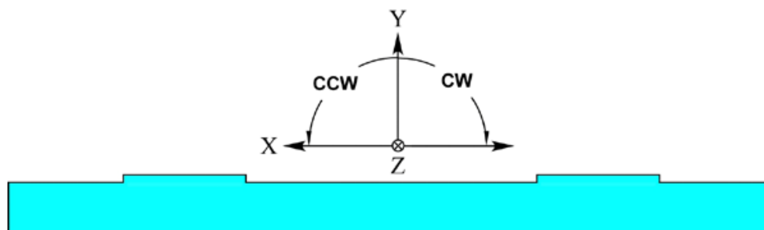

Figure 3-23: Definition of counter-clockwise (ccw) and clockwise (cw) rotation

As the probe tip pushes down on the microcantilever, it causes a rotation of the cantilever as well as a deflection if the probe tip is off-center. Referring to Figure 3-17 and Figure 3-23, the sense of rotation is counterclockwise (ccw) if the probe tip touches above the microcantilever center line (i.e., positive x-axis in Figure 3-23) and clockwise (cw) if it is below the center line.

In our experimental setup it is not possible to reliably place the probe tip directly on the microcantilever center line. We therefore infer the rotation from experimental measurement and compare with simulation for that inferred rotation.

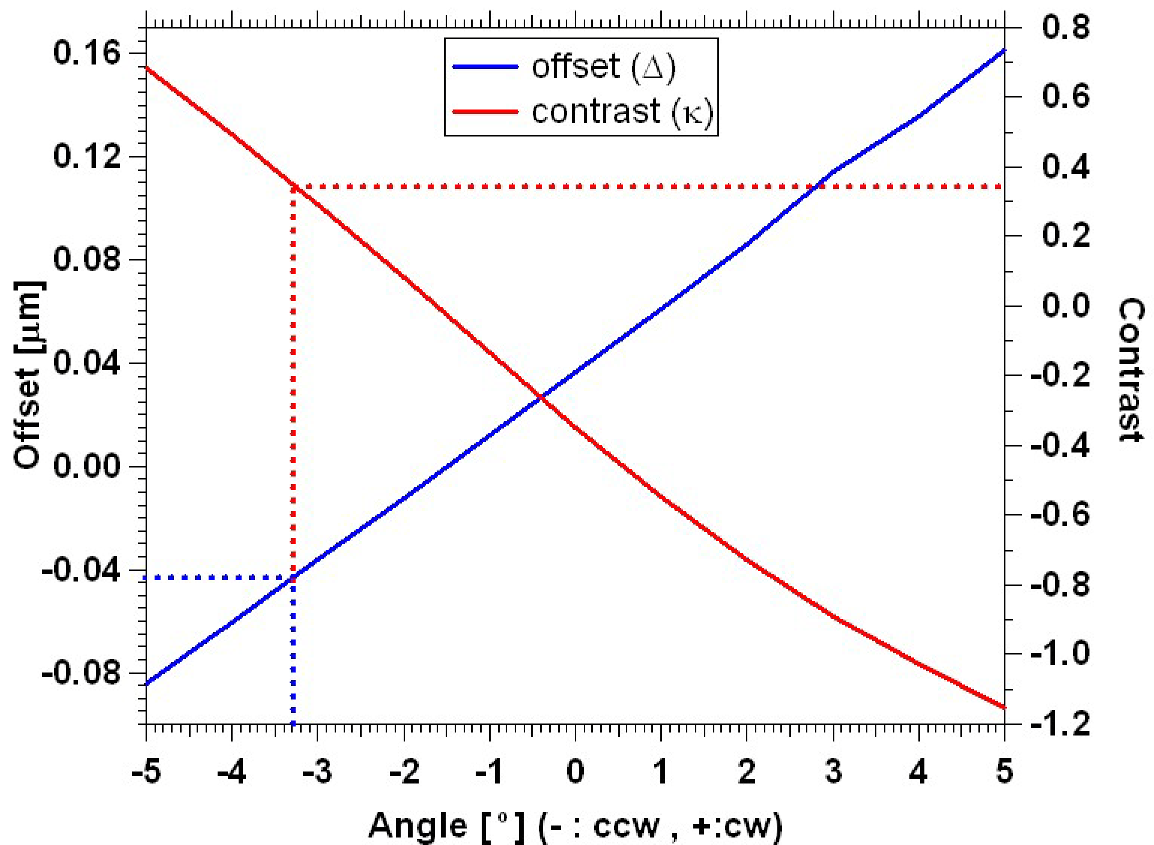

Figure 3-24: Offset and contrast as a function of rotation angle of the microcantilever about the z-axis.

Figure 3-24 shows the predicted offset (left axis) as a function of microcantilever rotation. Note that the offset is positive for microcantilever rotations greater than -1.5°, and negative for rotations less than -1.5°. The horizontal blue dashed line indicates the experimentally measured offset of -0.45 μm and the vertical blue dashed line shows that this corresponds to a microcantilever rotation of -3.3° (i.e., 3.3° ccw around the z-axis).

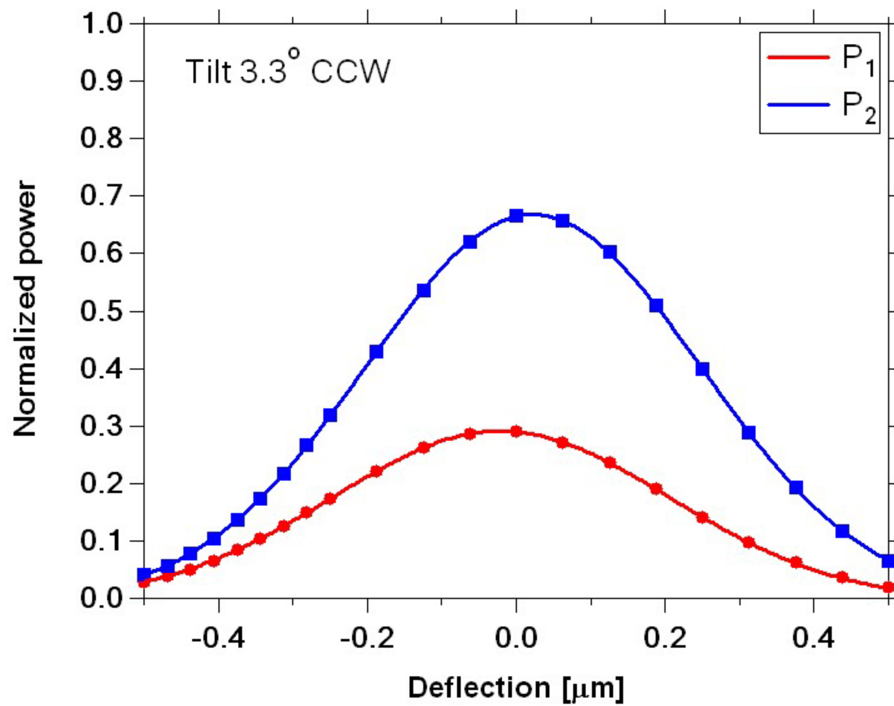

Figure 3-25: Simulation result of input waveguide microcantilever tilted 3.3 degree ccw direction about z-axis.

Figure 3-25 shows simulation results for P_1 and P_2 for the case of 3.3° ccw microcantilever rotation. Now the offset of P_1 and P_2 of course matches experiment, but the peak P_1 to peak P_2 ratio, P_1/P_2, is still different (0.44). It turns out that the differential signal is dependent on this ratio, as illustrated in Figure 3-26, which is obtained by scaling P_1 relative to

P_2 and forming the differential signal. Note that for P_1/P_2 ratios of order 1, the differential signal curves are quite similar (i.e., have nearly the same slope and therefore nearly the same contrast) and differ mainly in their average value. However, when the ratio significantly differs from 1 (such as the case of $P_1/P_2 = 10$) the slope and hence the contrast becomes smaller.

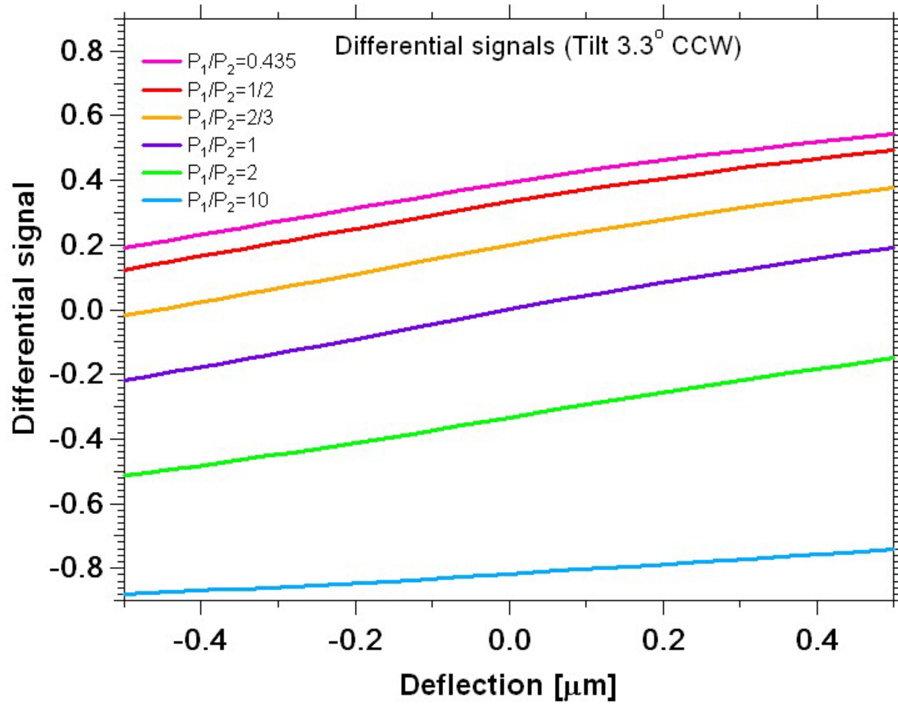

Figure 3-26: Differential signals tilted 3.3 degree to ccw direction as different ratios of P_1/ P_2

Figure 3-27 shows the differential signal from simulation for $P_1/P_2 = 10$ and the measured differential signal. There is good agreement between measurement and simulation, indicating that the differential signal behaves as predicted and hence we can expect the differential signal for an unrotated microcantilever to exhibit characteristics similar to Figure 3-6.

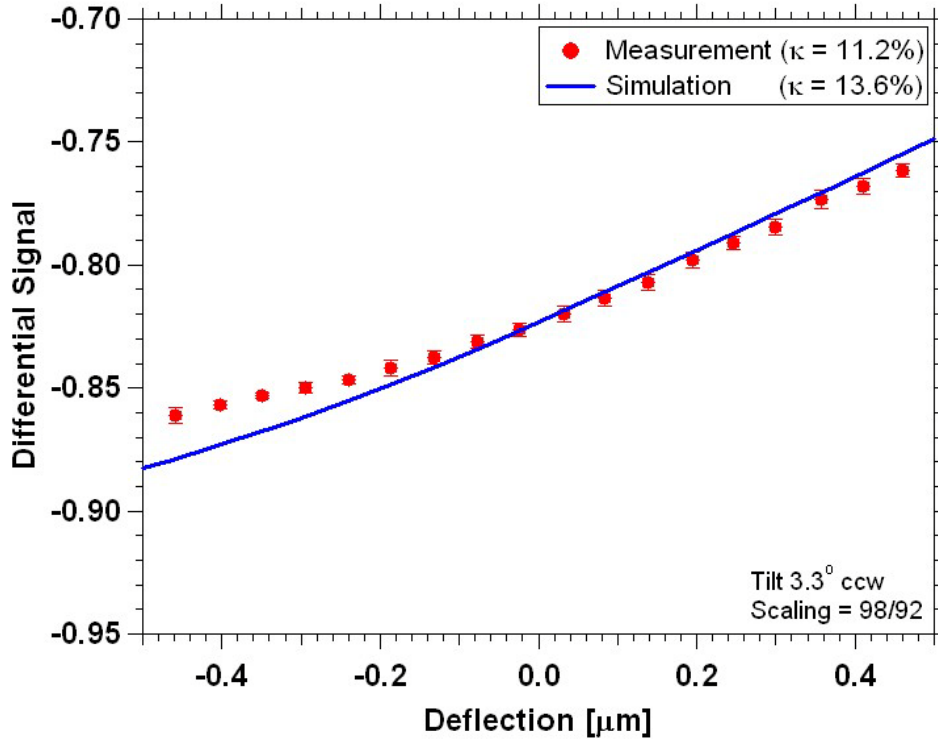

Figure 3-27 Comparison with the simulation and measurement results

We turn now to a discussion of microcantilever measurement sensitivity, which can be calculated as [72]

$$S = \frac{\Delta\eta}{\eta_0} \cdot \frac{1}{\Delta z} \tag{3.2}$$

where $\Delta\eta$ is the differential signal variation over some deflection range Δz, and η_0 is the differential signal for zero deflection. From the initial simulation (Figure 3-5 and Figure 3-6), we calculate a sensitivity of 3.6×10^{-4} nm^{-1}. The observed deflection sensitivity from Figure 3-27 is 1.4×10^{-4} nm^{-1}, which is smaller than predicted by simulation primarily because of the reduced contrast attributable to the large P_1/P_2 ratio. Note, however, that the observed deflection

sensitivity is still at least two orders of magnitude greater than piezoresistive transduction techniques [53-55, 73] and comparable to other optical transduction methods [38, 39].

Another way to characterize the performance of the microcantilever sensor is the minimum detectable deflection (MDD) [39, 53] which is defined as the deflection that corresponds to a signal-to-noise ratio equal to unity. The MDD is calculated as

$$MDD = \frac{\delta\eta}{m} \tag{3.3}$$

where m is the slope of the differential signal and $\delta\eta$ is the differential signal noise, which in turn can be expressed as

$$\delta\eta = \frac{2\sqrt{\left(\delta P_1 \cdot P_2\right)^2 + \left(\delta P_2 \cdot P_1\right)^2}}{\left(P_1 + P_2\right)^2} \tag{3.4}$$

where P_1 and P_2 are the power of the two output signals, and δP_1 and δP_2 are their noises, respectively, for a given bandwidth. The powers and noises are determined empirically from the noise floors of measured signal spectra.

We determined the differential signal noise for a low-noise version of our data acquisition system (PDA10CS detectors, Thorlabs, and NI PCO-6052E data acquisition board, National Instruments) in which δP_1 and δP_2 are measured to be 0.12 nW and 0.14 nW, respectively, for a bandwidth of 250 Hz. The measured P_1 and P_2 from Figure 3-21 are 6 μW and 0.58 μW. These measurements give a $\delta\eta$ calculated by Equation 3.4 of 0.023×10^{-3}. Using Equation 3.3 and a differential signal slope of 0.11 μm^{-1} from Figure 3-27 gives an MDD of 0.35 nm, which is limited by broadband noise on each output signal. This broadband noise does not appear to be shot-noise dominated as has previously been assumed [39], but is instead a power

independent background noise from the detectors and preamplifiers, indicating that it is either thermal or dark current shot-noise. Improving the detectors and electronics to reach the shot noise limit would improve the MDD by nearly an order of magnitude to 0.054 nm, which is comparable to the best performance offered by laser reflection transduction.

3.6 Conclusion

We have designed and demonstrated an in-plane photonic transduction method for microcantilevers that maintains signal sensitivity over the full measurable microcantilever deflection range. The microcantilever is etched to create a single mode rib waveguide and light from the end of the microcantilever is captured by an asymmetric multimode waveguide with a Y-branch splitter. The differential signal formed with the two Y-branch outputs is monotonically dependent on microcantilever deflection. The analysis shows good agreement between simulation and measurement when microcantilever rotation and P_1/P_2 ratio are taken into account, thereby validating the in-plane photonic transduction method. The measured differential signal sensitivity is 1.4×10^{-4} nm^{-1} and the minimum detectable deflection is 0.35 nm.

4 DIFFERENTIAL SPLITTER USING DOUBLE-STEP RIB WAVEGUIDE

Further analysis of our differential splitter shows that the sensitivity is dependent on the refractive index of the strip on the multimode rib waveguide, and that the amorphous silicon strip that we previously used introduced fabrication difficulties such as delamination and deformation of the strip due to adhesion issues and intrinsic film stress. I have therefore developed a new asymmetric double-step multimode rib waveguide that replaces amorphous with crystalline silicon having a higher refractive index, which improves sensitivity while maintaining the asymmetric structure of the differential splitter and eliminating fabrication issues. In this chapter we examine the design, fabrication, and experimental demonstration of the new differential splitter.

4.1 Design of Differential Splitter with Double-Step Rib Waveguide

Figure 4-1 and Figure 4-2 illustrate asymmetric double-step multimode rib waveguide and a Y-branch splitter for a photonic microcantilever. As before, the two outputs of the differential splitter are designated P_1 and P_2. The silicon photonic microcantilever has a width of 45 μm, a length of 110 μm, and a thickness of 0.65 μm and forms a single mode rib waveguide which has a rib width and height of 1.6 μm and 0.1 μm, respectively, and supports only a fundamental transverse electric (TE) mode at a wavelength of 1550 nm. Initially, the capture waveguide is a multimode rib waveguide etched 0.1 μm deep in a 0.75 μm thick silicon layer

(i.e., same etch depth as the single mode waveguide) and has a rib width of 3.0 μm. As shown in Figure 4-2, the entire top surface of the multimode rib waveguide, except for a 1.5 μm wide section on the right half of the rib, is etched down an additional 0.1 μm to form a double-step rib waveguide. The other waveguide structures for the optical waveguide network are the same as the single mode rib waveguide in the photonic microcantilever.

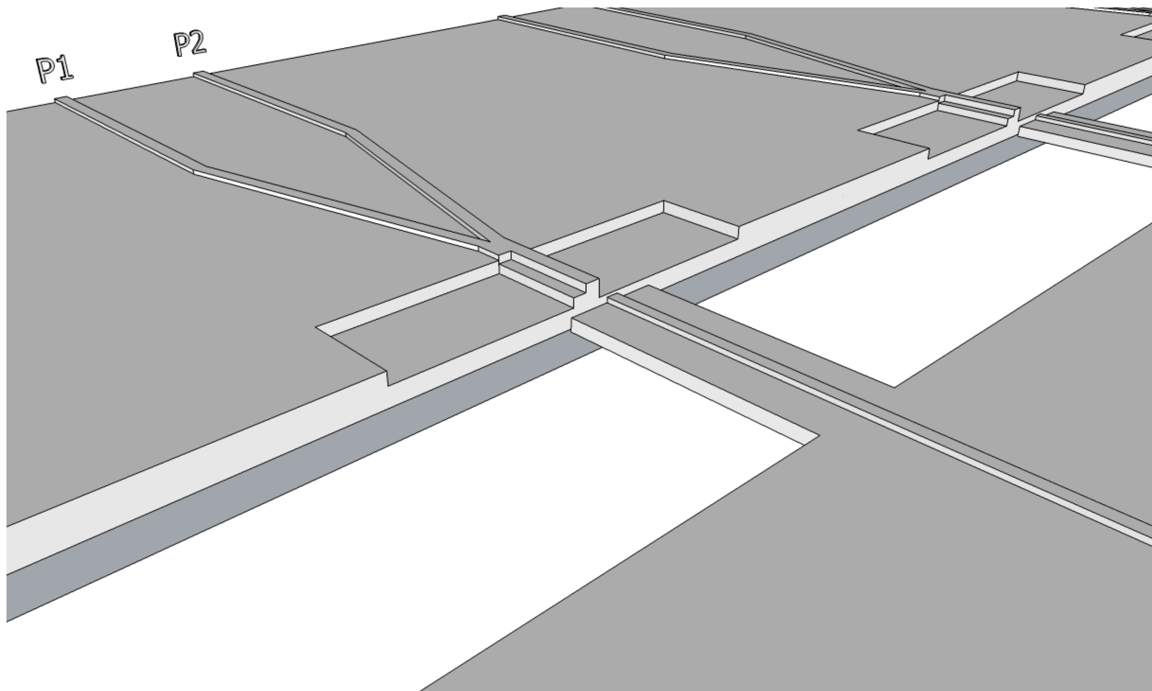

Figure 4-1: Schematic illustration of in-plane all-photonic microcantilever transduction structure based on a differential splitter composed of an asymmetric double-step multimode rib waveguide and Y-branch splitter.

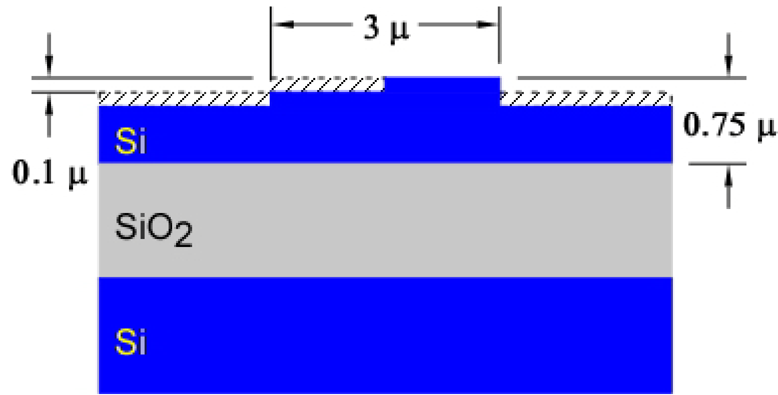

Figure 4-2: Cross section of the double-step rib waveguide. Dashed regions indicate the etched area from the initial multimode rib waveguide. Buried oxide layer thickness is 3 μm and the remaining silicon layer thickness is 0.55 μm.

We performed photonic simulations to optimize the length of the double-step rib waveguide in a differential splitter with results shown in Figure 4-3. The optical output powers of the differential splitter, P_1 and P_2, vary as a function of the length of the asymmetric double-step rib waveguide. For several arbitrarily selected lengths of the waveguide, we also calculated the contrast of the differential signal. The differential signal, η, is defined in Equation 3.1. The contrast, κ, of the differential signal is the difference between the maximum and minimum values of the differential signal over the deflection measurement range (±0.5 μm). The following Equation 4.1 defines the contrast of the differential signal,

$$\kappa = \eta_{+0.5\mu m} - \eta_{-0.5\mu m} . \qquad (4.1)$$

The important factors for choosing the length of the double-step rib waveguide are contrast, which sets the signal range, and the ratio of the peak P_1 and P_2 output powers. The latter should be close to unity such that each output signal has a similar dynamic range. Figure 4-3 suggests that the contrast variation with respect to the length of the waveguide is not large. Therefore, we choose the shortest length (17 μm) of the waveguide at which the peak output

powers of P_1 and P_2 are equal. P_1 and P_2 as a function of deflection are plotted for this case in Figure 4-4. Both P_1 and P_2 have similar Gaussian-like profiles over the deflection range of ±0.5 μm, but have a small peak offset, Δ, between the two profiles. As discussed in Ref. [21], the peak offset (in this case Δ=0.029 μm) results in a differential signal with monotonic response to deflection as shown in Figure 4-5. The contrast of the differential signal is -0.37 which is 1.6 times greater than our previously reported design while the asymmetric rib waveguide length is 6 times shorter.

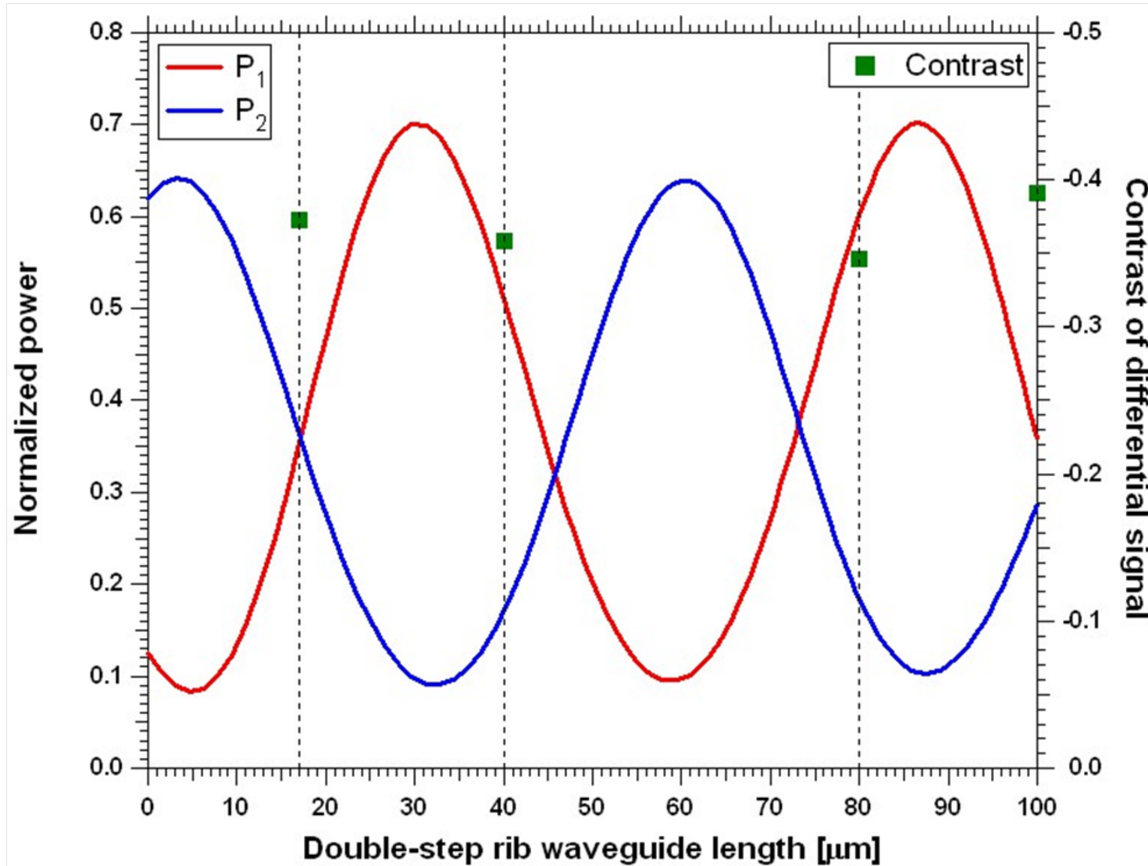

Figure 4-3: Normalized P_1 and P_2 output powers (left axis) and contrast of the differential signal (right axis) for selected lengths as a function of the length of the double-step rib waveguide.

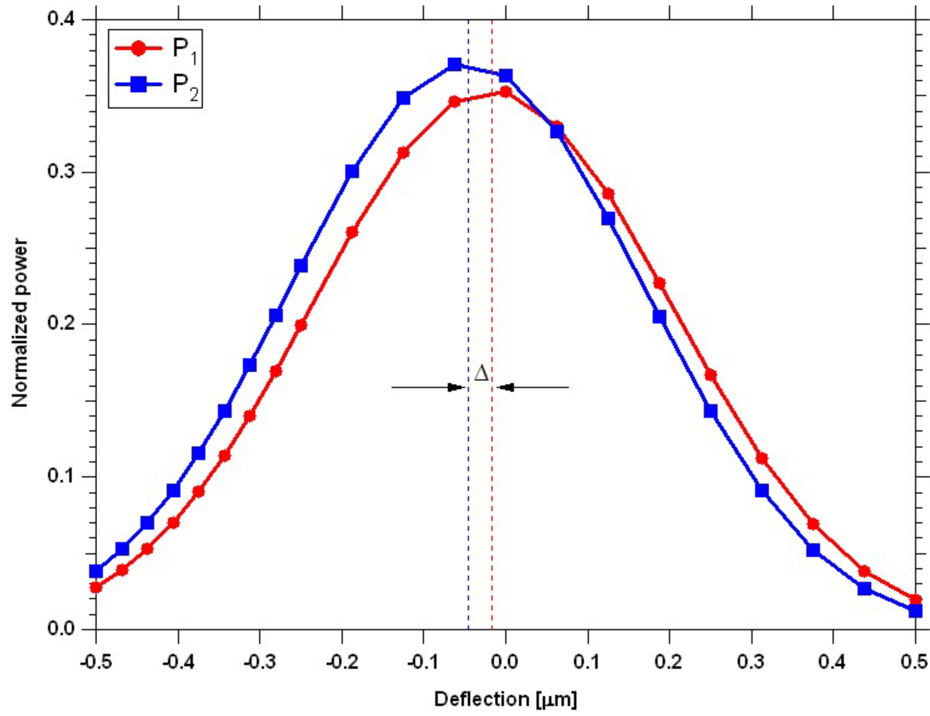

Figure 4-4: Output powers as a function of deflection for a 17 µm long double-step rib waveguide.

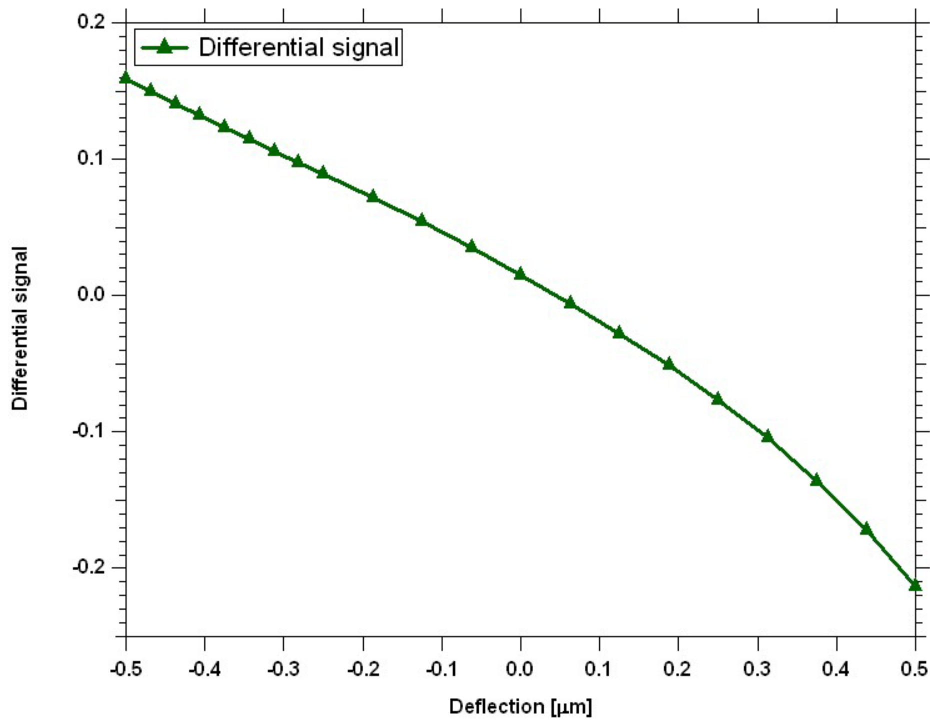

Figure 4-5: Differential signal calculated from outputs, P_1 and P_2, as a function of deflection

4.2 Fabrication of Photonic Microcantilever and Differential Splitter Array System

To experimentally confirm the performance of the new differential splitter, test samples were fabricated, each with two 8-microcantilever array sets. A schematic illustration of a photonic microcantilever array with a Y-branch splitter network is shown in Figure 4-6. The layout of one array set in the photonic circuit is shown in Figure 4-7. An input waveguide (I) into which light from an optical fiber is butt-coupled is located in the lower left corner as shown in Figure 4-7. The input waveguide is displaced from the center of the array by a large S-bend to avoid introducing uncoupled light from the fiber into the detector array used to measure light from the differential splitter output waveguides. Light coupled into the input waveguide is split by a three stage Y branch splitter network to 8 photonic microcantilevers. Another input waveguide (II) directs light into two groups of waveguides straddling the array to facilitate alignment of detector optics prior to measuring microcantilever array photonic properties.

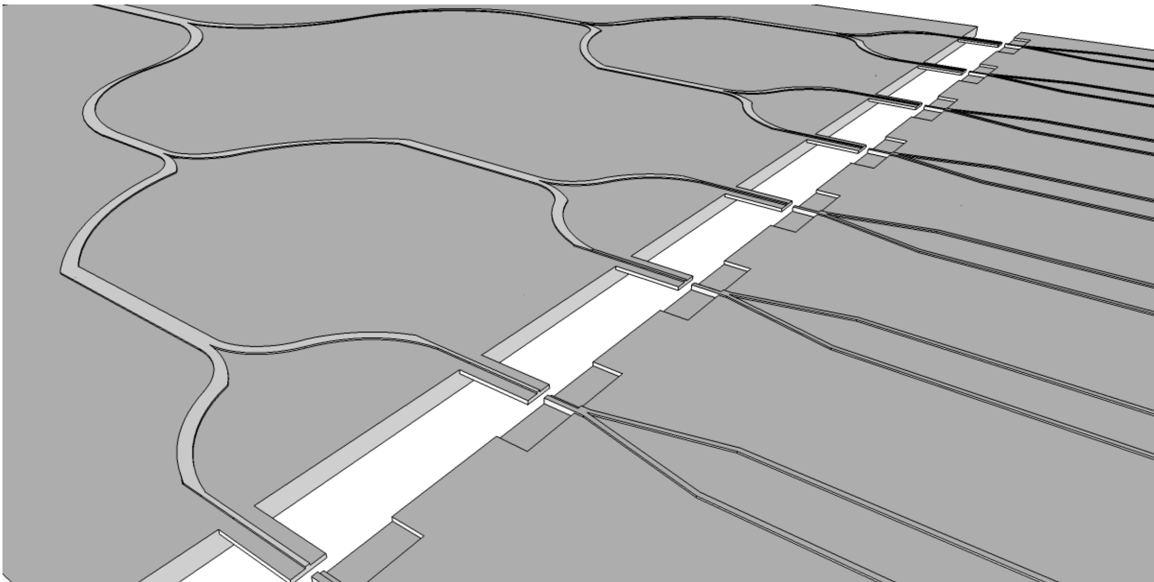

Figure 4-6: Schematic of photonic microcantilever array sensor with Y-branch splitter network

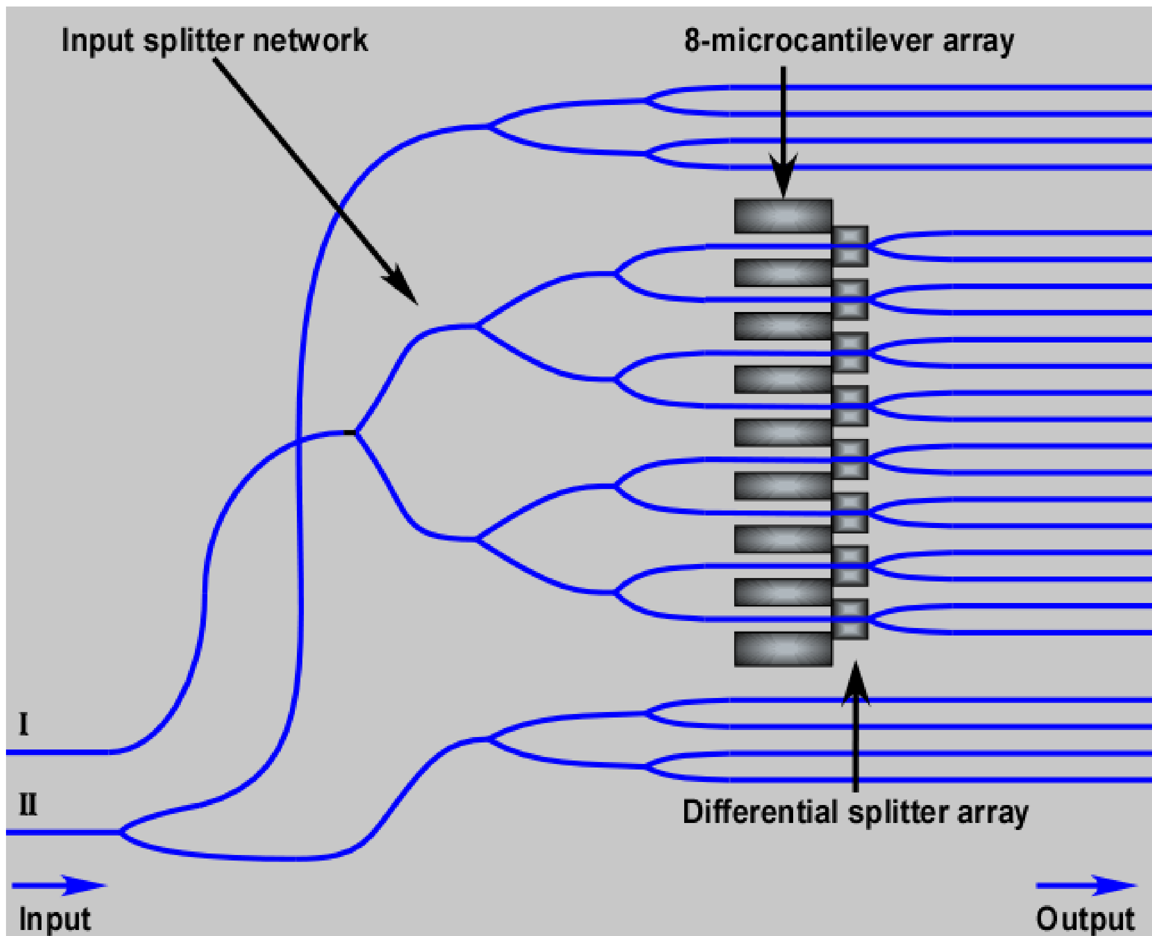

Figure 4-7: Layout of an 8-microcantilever array with associated Y-branch input splitter network. Each fabricated die includes two such structures.

Fabrication of test samples is similar to what we have previously reported [21], with the exception that the asymmetric double-step rib is patterned with electron beam lithography (EBL) followed by a 100 nm etch in an inductively coupled plasma reactive ion etcher (ICP-RIE). We use EBL in a scanning electron microscope only because positioning accuracy is much better (<0.1 μm) than for our contact mask aligner (~1 μm).

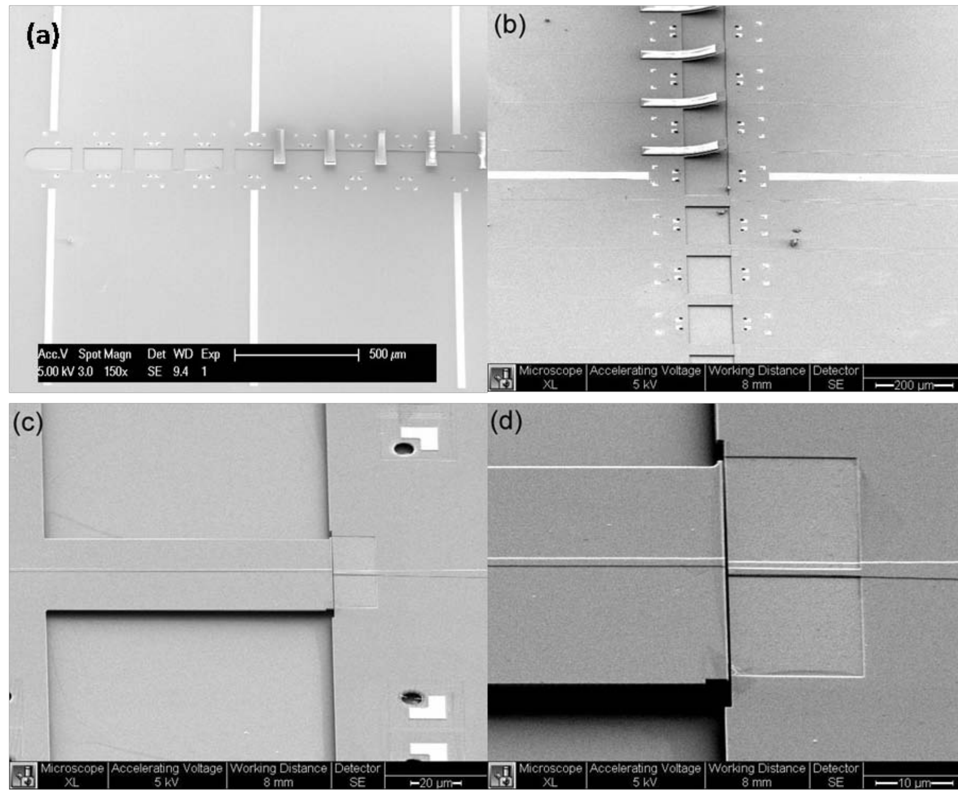

Figure 4-8: SEM images of (a) and (b) an 8-microcantilever array with SU8 bending patches on the top half of the array, (c) a photonic microcantilever that is 110 μm long and 45 μm wide, and (d) a double-step rib waveguide differential splitter.

Figure 4-8 shows scanning electron microscope (SEM) images of an 8-microcantilever array that has undergone the full fabrication process. Four microcantilevers (#1 through #4) are intentionally bent up with thermally stressed SU8 patches after releasing the microcantilevers with a hydrofluoric acid etch as shown in Figure 4-8(a) and Figure 4-8(b). A single microcantilever without the SU8 bending patch in an array is shown in Figure 4-8(c) and a close-up of a double-step rib waveguide in Figure 4-8(d).

4.3 Experimental Measurement

After fabrication, the samples are tested to examine the sensitivity and uniformity of the photonic microcantilever array responses as a function of deflection. The deflection state of all 8 microcantilevers in an array is simultaneously set by pushing down on them with the edge of a thin glass piece attached to a linear piezo-translator as shown in Figure 4-9. The 500 μm thick glass piece is cut in the shape of an isosceles trapezoid, with a base width of 1.5 mm on the edge that makes physical contact with the 8 microcantilevers. This edge is polished to remove major defects and increase the uniformity of deflection across the array. A rotation stage and goniometer ensure that the edge of the glass piece is perpendicular to the array of microcantilevers so that all are pushed down in unison. During actuation the piezo-translator moves through a 3 μm range in 50 nm steps.

An InGaAs digital line scan camera (SU512LDV-1.7RT-0500/LSE, Goodrich) simultaneously captures light from the 16 output waveguides in an array. The output face of the sample is imaged onto the camera's linear array of pixels such that each output waveguide illuminates a single pixel. Measurements are performed for both of the 8-microcantilever arrays on a die. The Set 1 array measurement uses a camera exposure time of 0.12 ms with a corresponding line sampling rate of 3,026 Hz. Measurement for the Set 2 array uses an exposure time of 0.08 ms and a line sampling rate of 3,443 Hz. For both measurements 400 line scans were averaged to obtain the mean output powers of P_1 and P_2 at each piezo-translator position.

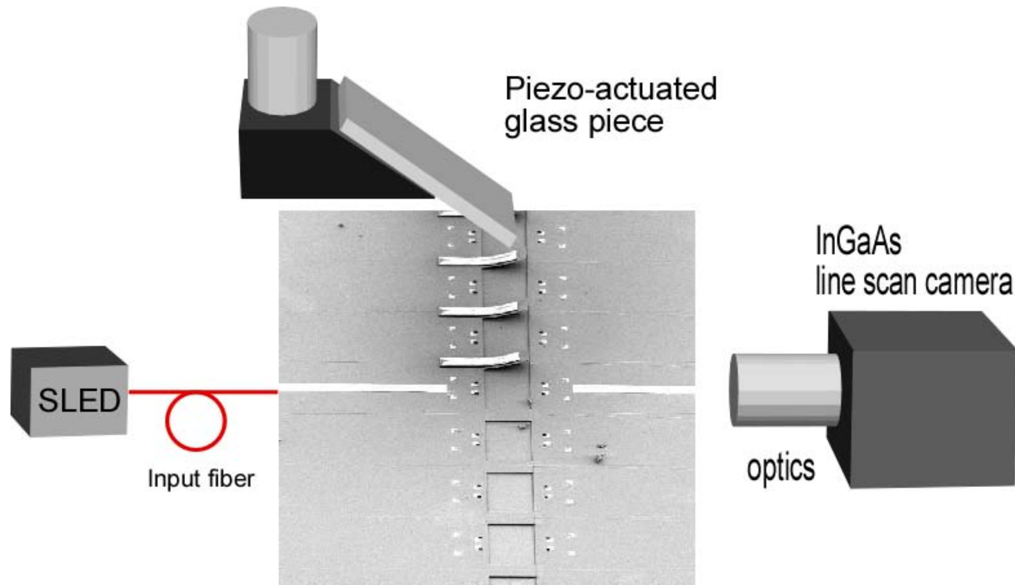

Figure 4-9: Sketch of measurement setup for an 8-microcantilever array

The measured P_1 and P_2 output powers from both microcantilever arrays on a single die are shown in Figure 4-10(a) and Figure 4-10(b) as a function of microcantilever deflection. Microcantilevers #4 and #5 of Set 1 are not included in the figures since breaks in the input waveguides prevented light from being guided to these microcantilevers (see Figure 4-11). Additionally, although only four microcantilevers in each set were covered with SU8 patches, we note that most of the microcantilevers without patches were initially bent up by approximately 0.6 μm or more. The exceptions are Set 1 #8 and Set 2 #6 and #8 which have essentially no deflection after being released. This accounts for the flat P_1 and P_2 responses at positive deflection for these microcantilevers (i.e., the glass piece only contacts them near zero deflection and below).

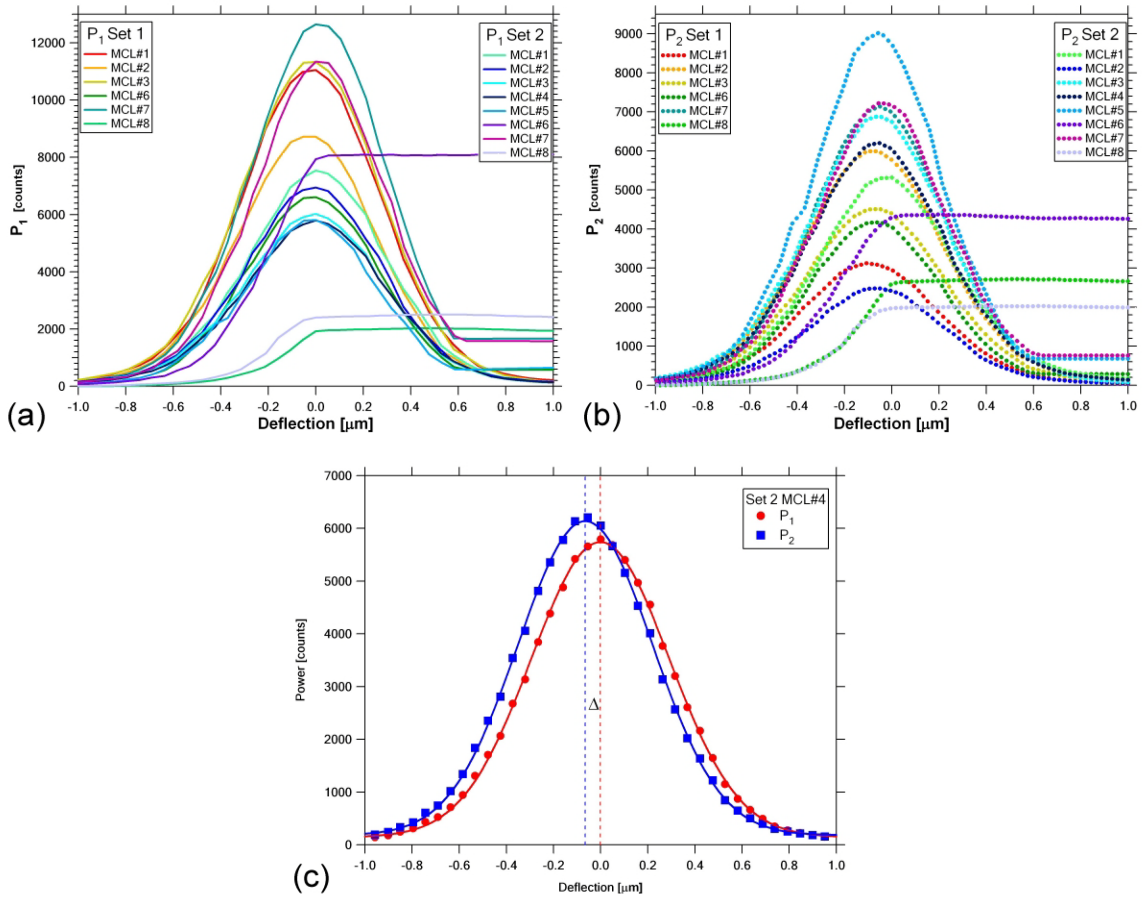

Figure 4-10: Measured individual (a) P_1 and (b) P_2 output powers as a function of deflection for 14 out of 16 microcantilevers from two array sets. (c) Both outputs, for example, from microcantilever #4 of Set 2 are plotted in the same graph. There is a lateral shift, Δ, as expected.

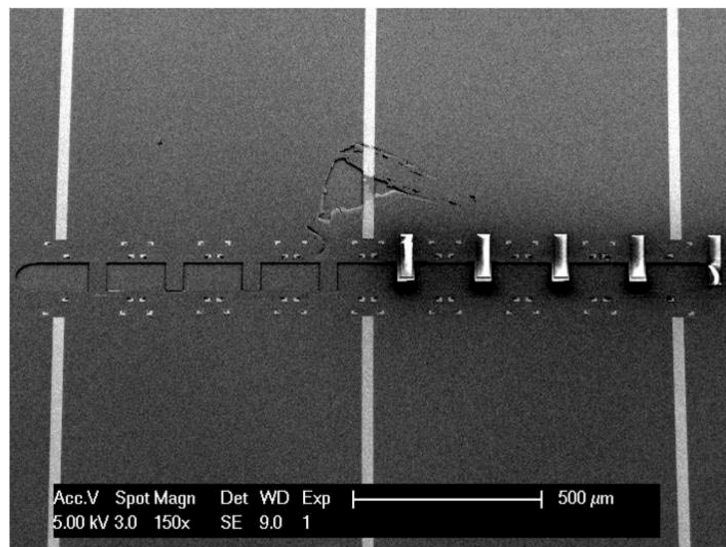

Figure 4-11: SEM image shows clearly a defect which breaks waveguides of microcantilever #4 and #5 in the array set 1

The other P_1 and P_2 profiles are Gaussian-like as expected. However, the measured profiles are wider than the predicted profiles from simulation as shown in Figure 4-3. The difference in widths is due to the divergence of light across the gap between the free end of the microcantilever and the capture waveguide, which is not included in the simulation. The peak power variation from waveguide to waveguide in the measured data is likely due to different losses in individual waveguides caused by factors such as dissimilar waveguide top surface conditions, coupling efficiencies at interfaces, and output waveguide facet roughness. Additionally, the peak positions of the profiles in Figure 4-10(a) and Figure 4-10(b) are not perfectly aligned because of small defects in the glass piece. Therefore, before calculating the differential signals, we redefine zero deflection for each microcantilever to be at the P_1 peak position which simulation indicates coincides with zero deflection.

Figure 4-12 shows the differential signals calculated from the measured P_1 and P_2 output powers. Subsequent SEM and atomic force microscope (AFM) inspections revealed fabrication imperfections for the gaps of microcantilever #8 of Set 1 and #8 of Set 2, and a particle stuck on the tip of microcantilever #1 of Set 2 as shown in Figure 4-13. Therefore, the differential signals from these microcantilevers are not included in Figure 4-12. Note that the differential signal curves have a wide vertical spread although their slopes are somewhat similar, making it difficult to compare differential signals for different microcantilevers in the arrays. As discussed in Chapter 3 [21], the vertical spread of the differential signals is due to different ratios of the peak values of P_1 and P_2. To compensate for the different ratios, we have introduced a scaled differential signal [74] defined as:

$$\eta_{scaled} = \frac{P_2 - \alpha \cdot P_1}{P_2 + \alpha \cdot P_1}. \tag{4.2}$$

The scaling factor, α, is given by $\alpha = P_{10}/ P_{20}$ where P_{10} and P_{20} are the output powers at an arbitrary reference deflection. We choose the P_1 peak position to be the reference deflection for P_{10} and P_{20}. As shown in Figure 4-14, the scaled differential signals from 11 microcantilevers from both sets overlap well with each other for deflections of zero and below where the glass piece contacts all of the microcantilevers. As we have shown previously for differential splitters based on amorphous silicon strip loading, variation in the slopes of the scaled differential signals correlates with differences in peak offset (Δ) values. [74]

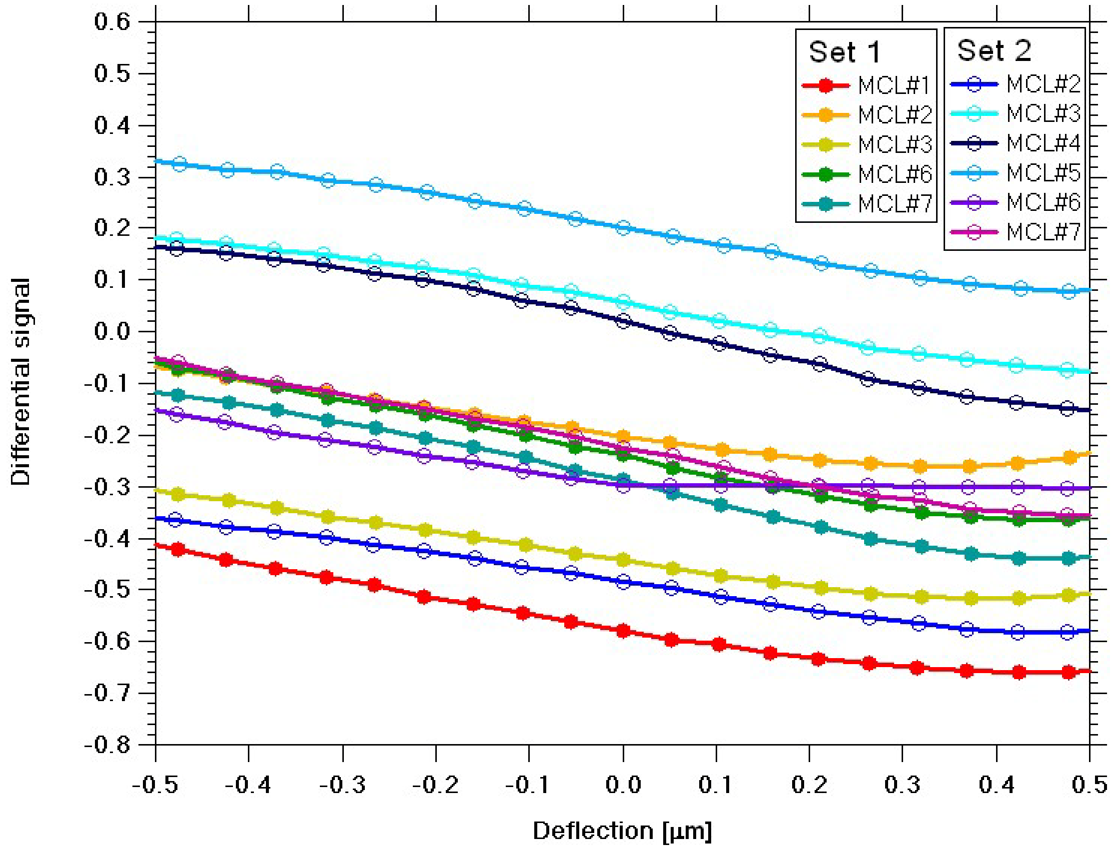

Figure 4-12: Differential signals as a function of deflection

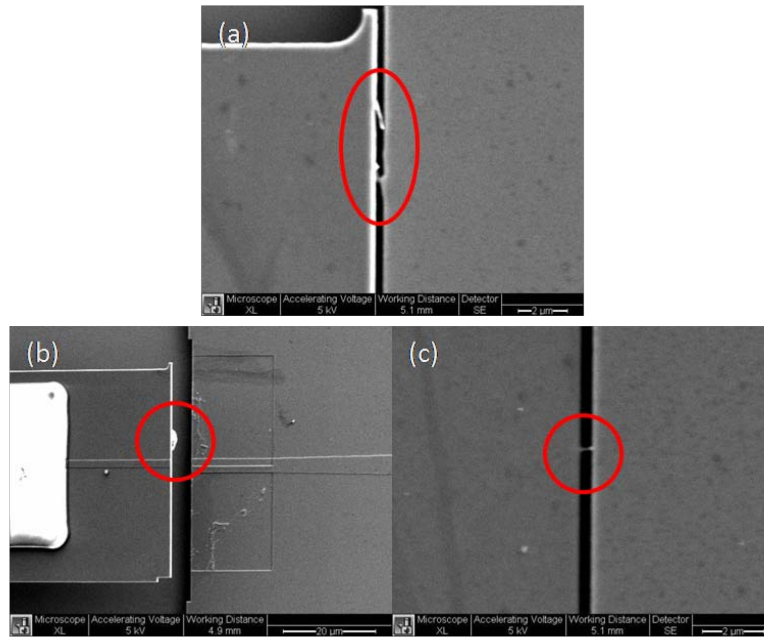

Figure 4-13: SEM images of microcantilever (a) #8 of Set 1, (b) #1 of Set 2, and (c) #8 of Set 2

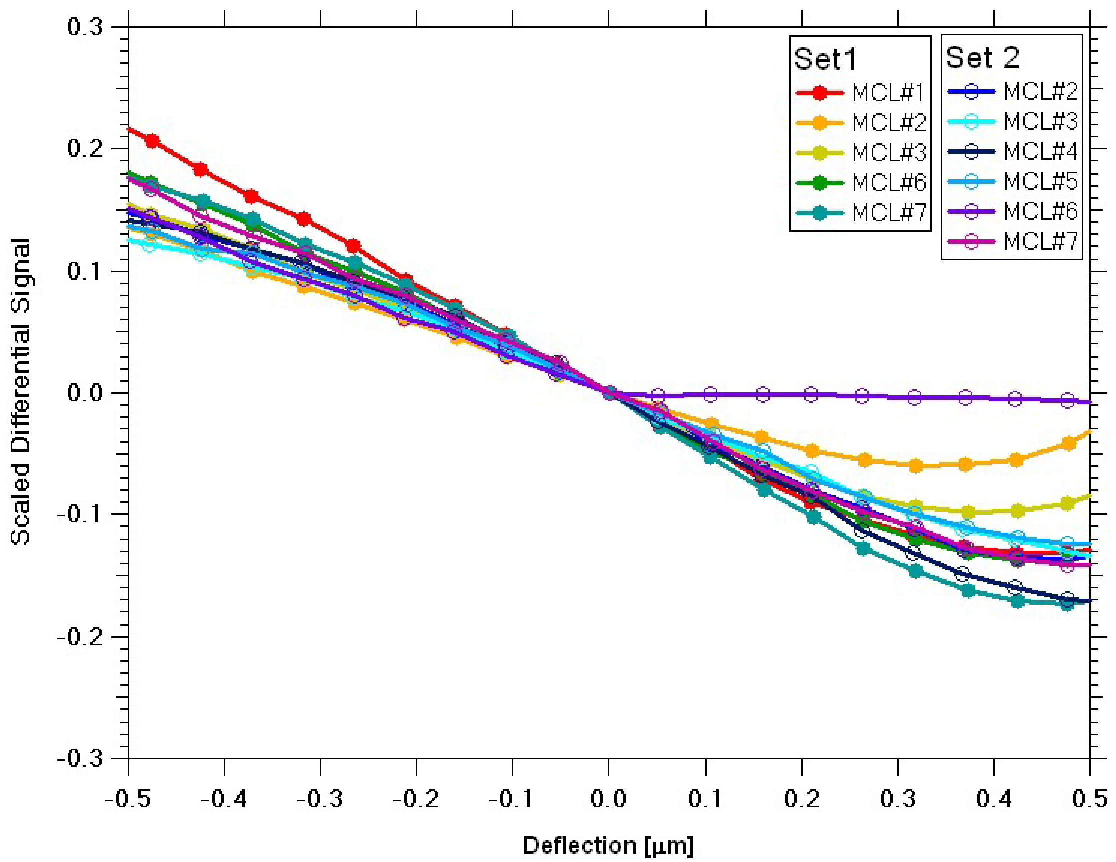

Figure 4-14: Scaled differential signals as a function of deflection.

4.4 Analysis and Discussion

After SEM and AFM measurement of the as-fabricated dimensions of the asymmetric double-step rib waveguides, we re-ran the simulation of its photonic response as a function of deflection. The updated simulation results are compared with the average measured scaled differential signal in Figure 4-15. Over the deflection range where the averaged scaled differential signal exhibits roughly linear behavior (-0.5 μm to 0.3 μm) the average slope is $0.32\ \mu m^{-1}$. The difference between measurement and simulation in this deflection range is from the broader widths and a slightly larger peak offset of the measured P_1 and P_2 profiles. While the averaged scaled differential signal agrees reasonably well with the simulation in that range, the two curves diverge noticeably for deflections greater than 0.3 μm.

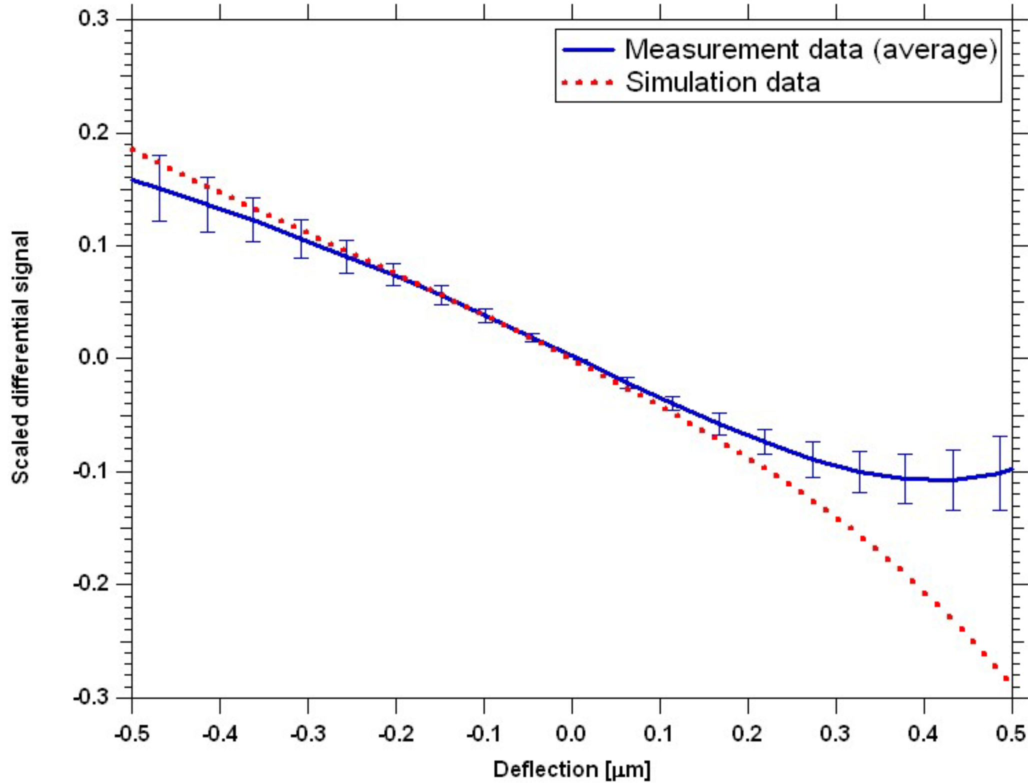

Figure 4-15: Comparison of measured data with simulation results

Note that microcantilever #6 from Set 2 is not included in the average for deflections greater than zero and hence does not bias the average in this region.

Analysis of measurement data indicates that this is mainly due to a background DC offset in the measurements. Although an aperture mask is used to block the majority of stray light not associated with the P_1 and P_2 outputs, some amount of scattered and stray light is still incident on the InGaAs camera's pixel array. Because of the scattered and stray light, the camera measures a DC offset in addition to the deflection-dependent output powers. In the region where P_1 and P_2 have large values, such as around zero deflection, the effect of the background DC offset on the scaled differential signal is negligible. However, when the DC offset is comparable to the values of P_1 and P_2, the scaled differential signal will differ markedly from the expected behavior. The effect is more pronounced for positive deflections because the P_2 peak is shifted toward the negative deflection region. Since the effect is noticeable only for deflections greater than 0.3 μm, the practical implication of the DC offset is a limitation of the dynamic range of the microcantilevers. As the intended future use of the photonic microcantilevers is for biological and chemical sensing scenarios where the expected static deflection is on the order of 100 nm, [49] we do not expect the DC offset to cause a significant limitation to sensing. Nonetheless, we are presently investigating techniques to dramatically reduce stray light in the silicon slab to largely eliminate the DC offset issue.

Two important parameters for characterizing the capability of a microcantilever sensor to detect small changes in static deflection are the sensitivity and the minimum detectable deflection (MDD). The sensitivity of a microcantilever sensor is the change in output signal per unit deflection of the microcantilever. As noted above, the average sensitivity is 0.32×10^{-3} nm^{-1}, which is orders of magnitude better than piezoresistive readout methods [72, 73, 75] (with

sensitivities typically on the order of 10^{-6} nm^{-1}), and comparable to optical lever readout methods [38, 39] whose best reported sensitivities are on the order of 10^{-3} nm^{-1} [38]. The MDD gives the limit of detection of microcantilever deflection and is calculated by dividing the noise of the transduction signal by the sensitivity of the readout method [39]. For our photonic microcantilevers, the noise of the scaled differential signal ($\delta\eta$) can be determined from the measured power, noise, and correlation of the P_1 and P_2 outputs for each microcantilever. The first-order approximation of the noise of the scaled differential signal is given by:

$$\delta\eta = \frac{2\alpha}{\left(P_2 + P_1\right)^2}\sqrt{P_2^2\delta P_1^2 + P_1^2\delta P_2^2 - P_1 P_2 \delta P_1 \delta P_2 r_{12}} \tag{4.3}$$

where δP_1 and δP_2 are the measured noise of the two outputs and r_{12} is the correlation coefficient for P_1 and P_2. Based on the measured values of P_1 and P_2 and the slope of the scaled differential signal, we obtain an average MDD of 141 pm for a 3.5 Hz bandwidth, which corresponds to a minimum detectable surface stress of 0.3 mN/m. This MDD is comparable to or better than other common readout methods [72, 73, 75, 76] for static deflection. Analysis of the total noise shows that the signal shot noise is roughly equal in magnitude to that of the combined power-independent noises - thermal noise, dark current shot noise, flicker noise, etc. The MDD can be improved by increasing the output powers, which will reduce $\delta\eta$, and by decreasing the exposure time, which will reduce the dark current shot noise.

4.5 Conclusion

In conclusion, we have implemented a new differential splitter using an asymmetric double-step multimode rib waveguide for in-plane all-photonic transduction of a photonic microcantilever. Simultaneous measurement of an array of microcantilevers using this

transduction method has been demonstrated with mechanical actuation of the microcantilevers. From the measured outputs, the scaled differential signals are calculated and 11 of the 16 microcantilevers from two independent arrays show acceptable uniformity and repeatability. The averaged scaled differential signal from the measurements is well matched with simulation in the deflection range of -0.5 μm to 0.3 μm with noticeable disagreement for deflections greater than 0.3 μm due to a DC offset in the measurements. The sensitivity and MDD of the photonic microcantilever system are 0.32×10^{-3} nm^{-1} and 141 pm, respectively, which are comparable to or better than other common readout methods for nanomechanical static-deflection sensors. Currently we are investigating further structure optimization to enhance system performance and practical methods to eliminate the measured DC offset. We are also pursuing application of the transduction method reported here to much larger arrays of photonic microcantilevers.

5 SENSITIVITY ENHANCEMENT OF DIFFERENTIAL SIGNALS

Through analytical examination of the relationship between differential signal and the asymmetric double-step multimode rib waveguide, we have found a way to improve performance of the photonic microcantilever sensor. In this chapter, the relationship between sensitivity and double-step rib waveguide structure is investigated analytically and experimentally.

5.1 Sensitivity of Photonic Microcantilever Sensor

When evaluating the effectiveness of a transduction method for microcantilever systems, one of the important metrics is the sensitivity. For a microcantilever system designed to measure static deflection, the sensitivity is defined as the change in the transduction signal per unit deflection of the microcantilever. The sensitivity of the photonic microcantilever system is the slope of the differential signal which is calculated by fitting a straight line to the differential signal.

From the previous experiments as discussed in Chapter 4, the sensitivity of the double-step waveguide-based differential splitter has been experimentally demonstrated as comparable to other transduction methods which are currently employed for static deflection sensors. The following Table 5-1 shows the sensitivity and MDD comparison with the other reported transduction methods.

Table 5-1: Sensitivity and MDD comparison with other transduction methods reported

Transduction Type	Sensitivity [units/nm]	MDD [nm]	Reference [#]
Piezoresistive	3.00×10^{-7}	0.4	Thaysen et al. [72]
Piezoresistive	4.00×10^{-6}	0.4	Gunter et al. [75]
Optical waveguide	1.50×10^{-5}	3.33	Zinoviev et al. [39]
MOSFET	0.2 [mA/nm]	2.5×10^{-4}	Shekhawat et al. [56]
Piezoresistive	3.40×10^{-6}	0.1	Yu et al. [73]
Optical beam reflection	49 [nm/pH]	-	Ji et al. [77]
Optical beam reflection	10^{-3}	-	Kocabas et al. [38]
Optical interferometer	-	0.001	Manalis et al. [78]
Optical interferometer	-	0.001	Schönenberger et al. [79]
Photonic (α-Si strip-loaded)	0.14×10^{-3}	0.21	Noh et al. [21]
Photonic (double-step)	0.32×10^{-3}	0.14	Noh et al. [22]

The best reported sensitivities are 10^{-3} nm^{-1} and 4×10^{-6} nm^{-1} for optical readout and piezoresistive methods, respectively as shown in Table 5-1.

5.2 Analysis

Figure 5-1 shows a schematic diagram of the geometry of a photonic microcantilever and differential splitter. The silicon microcantilever is 45 μm wide, 0.65 μm thick, and 110 μm long. The rib down the middle of the microcantilever is 0.1 μm tall and 1.6 μm wide, and forms a rib waveguide that supports only a fundamental transverse electric (TE) mode at a wavelength of 1550 nm.

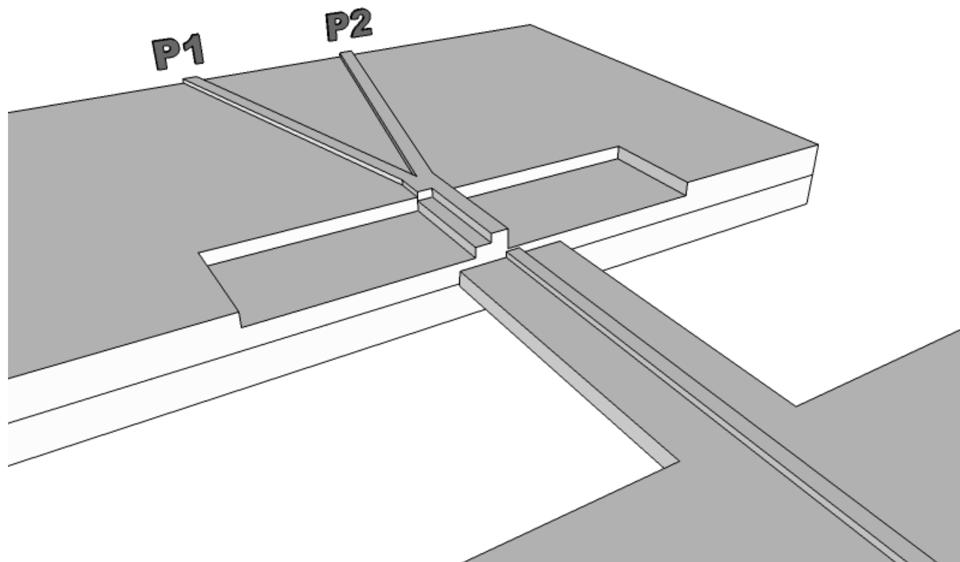

Figure 5-1: Schematic of photonic microcantilever and asymmetric differential splitter

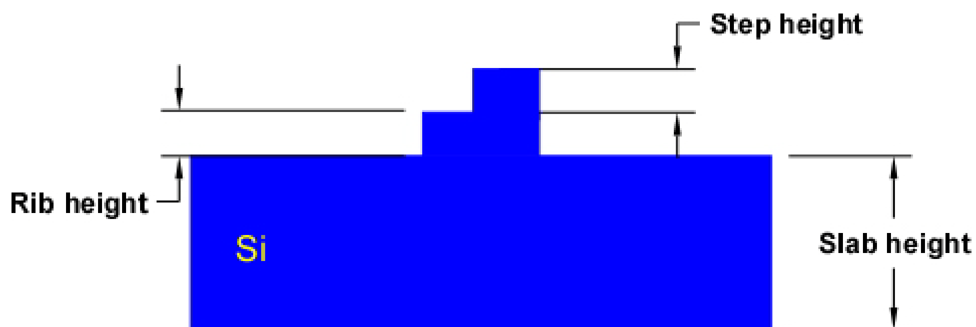

Figure 5-2: Cross-section of the asymmetric double-step multimode rib waveguide

Figure 5-2 shows a cross section of the asymmetric double-step multimode rib waveguide that captures light from the free end of the microcantilever. The double-step rib waveguide is fabricated by etching half the width of a 3 μm wide multimode waveguide and the neighboring slab. The etch depth determines the step height h and causes the slab height to be 0.65 μm – h. The rib height of the double-step rib waveguide is the same as that of the other waveguides on the chip (0.1 μm).

We have modified the differential signal formula to compensate waveguide variation in the array system, a scaled differential signal (Equation 4.2), as discussed in Section 4.3. In the case of a step height of 50 nm and length of 17 μm of the double-step multimode rib waveguide, Figure 5-3shows simulation results of output powers and the scaled differential signal as a function of microcantilever deflection. The scaled differential signal exhibits monotonic and near linear response over the deflection range due to a peak difference, Δ, between the Gaussian-like output power profiles. The sensitivity of the photonic microcantilever system is the slope, $\partial\eta/\partial d$ (where d is deflection), of the scaled differential signal. The slope is calculated by fitting a straight line to a differential signal.

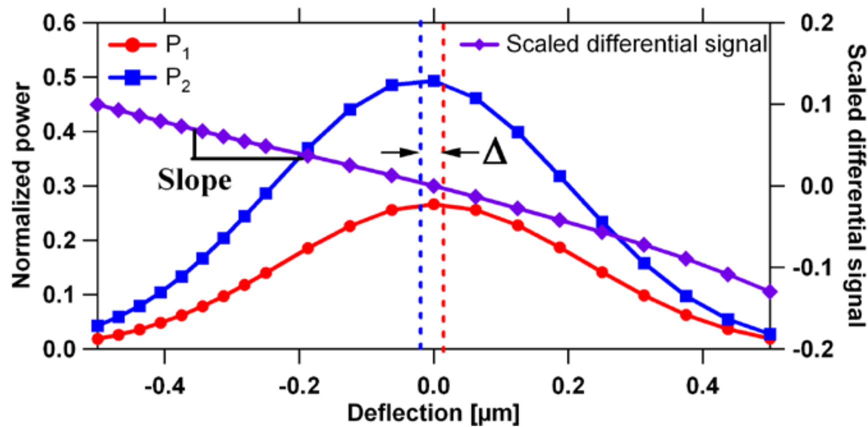

Figure 5-3: Output power profiles and the scaled differential signal as a function of deflection.

We perform photonic simulations for four different step heights to examine the effect on the slope of the scaled differential signal. Simulation results are shown in Figure 5-4 for deflections less than zero (the deflection range is chosen to be commensurate with experimental measurements shown below). Note that larger step heights (deeper etch) cause steeper slopes.

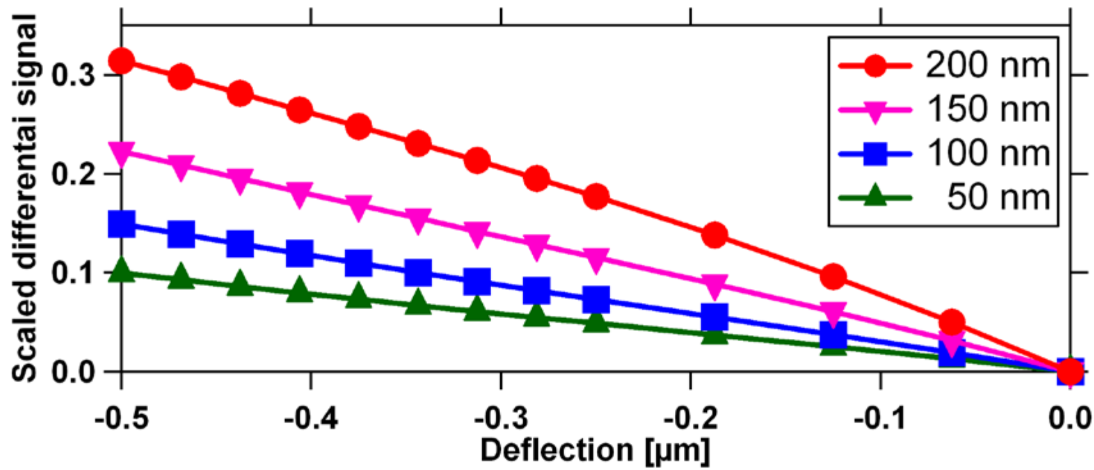

Figure 5-4: Simulation results for four different step-height cases.

To understand why, first consider the fundamental and first order mode profiles, (i) and (ii), in Figure 5-5 for step heights of 50 and 200 nm. While larger step height results in lateral squeezing of the fundamental mode, the vertical position of its centroid is relatively unchanged. However, the vertical position of the main (left) lobe of the first order mode shifts noticeably downward with increasing step height. Also note that for both step heights the fundamental mode is predominantly directed into the upper (P1) output and vice versa for the first order mode as shown in top views, (iii) and (iv), of mode propagation profiles in the differential splitter.

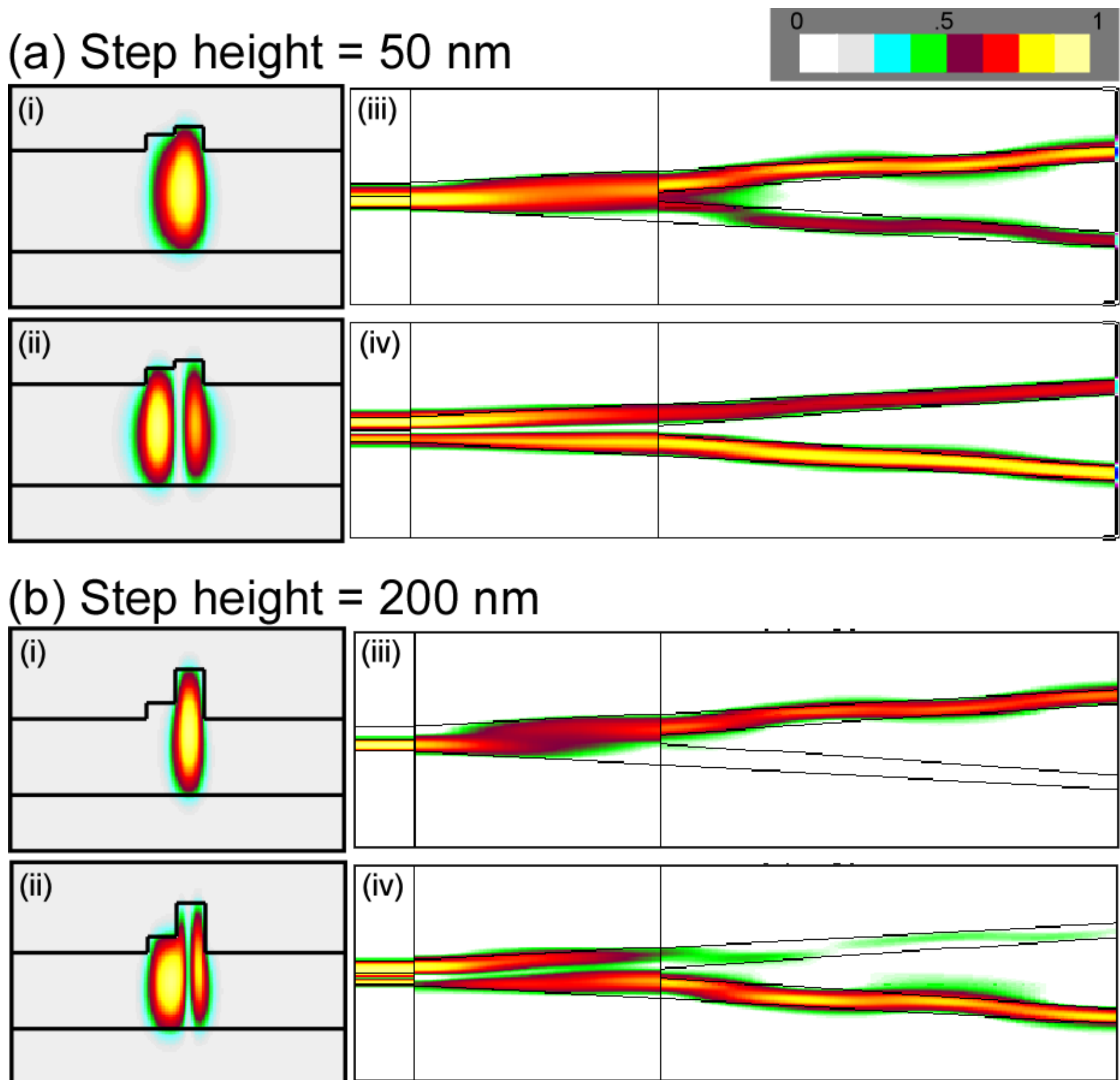

Figure 5-5: (i) Fundamental and (ii) first order mode profiles, and top view of mode propagation in differential splitter for the (iii) fundamental and (iv) first order modes for 50 nm and 200 nm step heights.

Now consider coupling from the microcantilever waveguide mode into the fundamental and first order modes as a function of deflection. Simulation results based on mode overlap integrals are shown in Figure 5-6 for all 4 step heights. Note that maximum mode coupling into the fundamental mode for etch step height is at zero deflection, corresponding to the fundamental mode showing no significant change in its vertical position (however, narrowing of the mode

does result in less coupled light for larger step heights). Also note that the maximum mode coupling for the first order mode is more shifted toward negative deflection with larger step height, reflecting the fact that the mode becomes more shifted toward the bottom of the waveguide (vertical lines indicate deflection at which maximum mode coupling occurs).

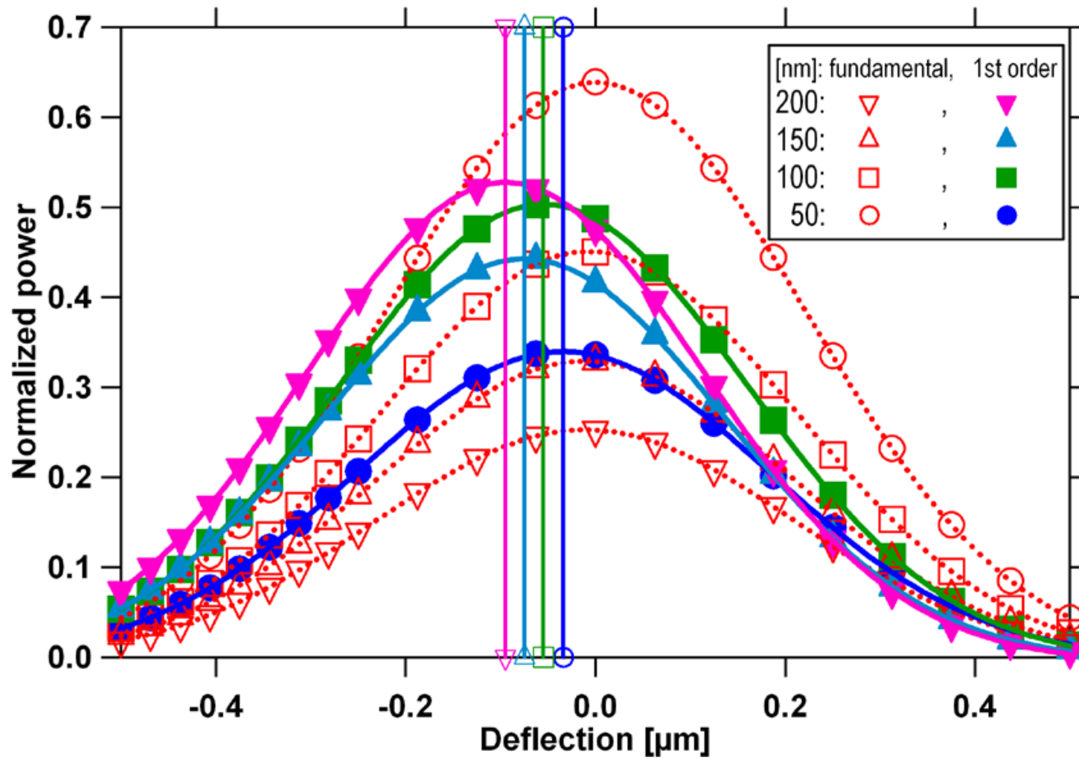

Figure 5-6: Mode coupling as a function of microcantilever deflection.

Hence the separation between maximum coupling into the fundamental and first order modes is larger for greater step heights, which is shown in Figure 5-7. Also plotted is the corresponding lateral shift, Δ, for P1 and P2, which is clearly affected by the separation of the mode coupling maxima because, as seen in Figure 5-3, each mode is predominantly directed into

either the P1 or P2 output path. As demonstrated in Fig. 5(f) of Ref. [74], larger Δ corresponds to larger slope of the scaled differential signal.

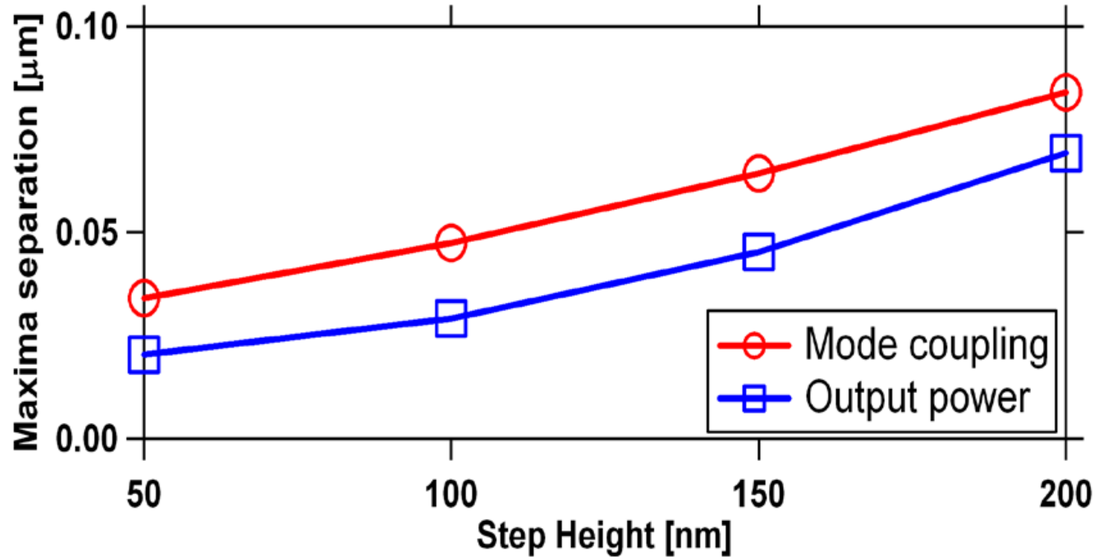

Figure 5-7: Peak Maxima separation for mode coupling and lateral shift of P_1 and P_2 as a function of step height.

5.3 Fabrication

To experimentally investigate the effect of step height, we fabricated two samples, each with two arrays of 8 microcantilevers. The fabrication process is as described in Section 4.2, except four different step heights were used. We chose four different etch times to make four different etch depth for the experiment and put two different heights on each sample. After finishing fabrication processes, the feature dimensions of the double-step rib waveguide were measured by SEM and AFM inspections. We simultaneously measured the outputs from an 8-microcantilever array with an InGaAs line scan camera while pushing down on the whole array

with the polished edge of a glass piece attached to a piezo-translator. Since the microcantilevers are nominally at zero-deflection after release, the measurement range is limited to deflections downward from zero-deflection (i.e., negative deflections). Figure 5-8 shows scanning electron microscope (SEM) images of photonic microcantilever array and differential splitter.

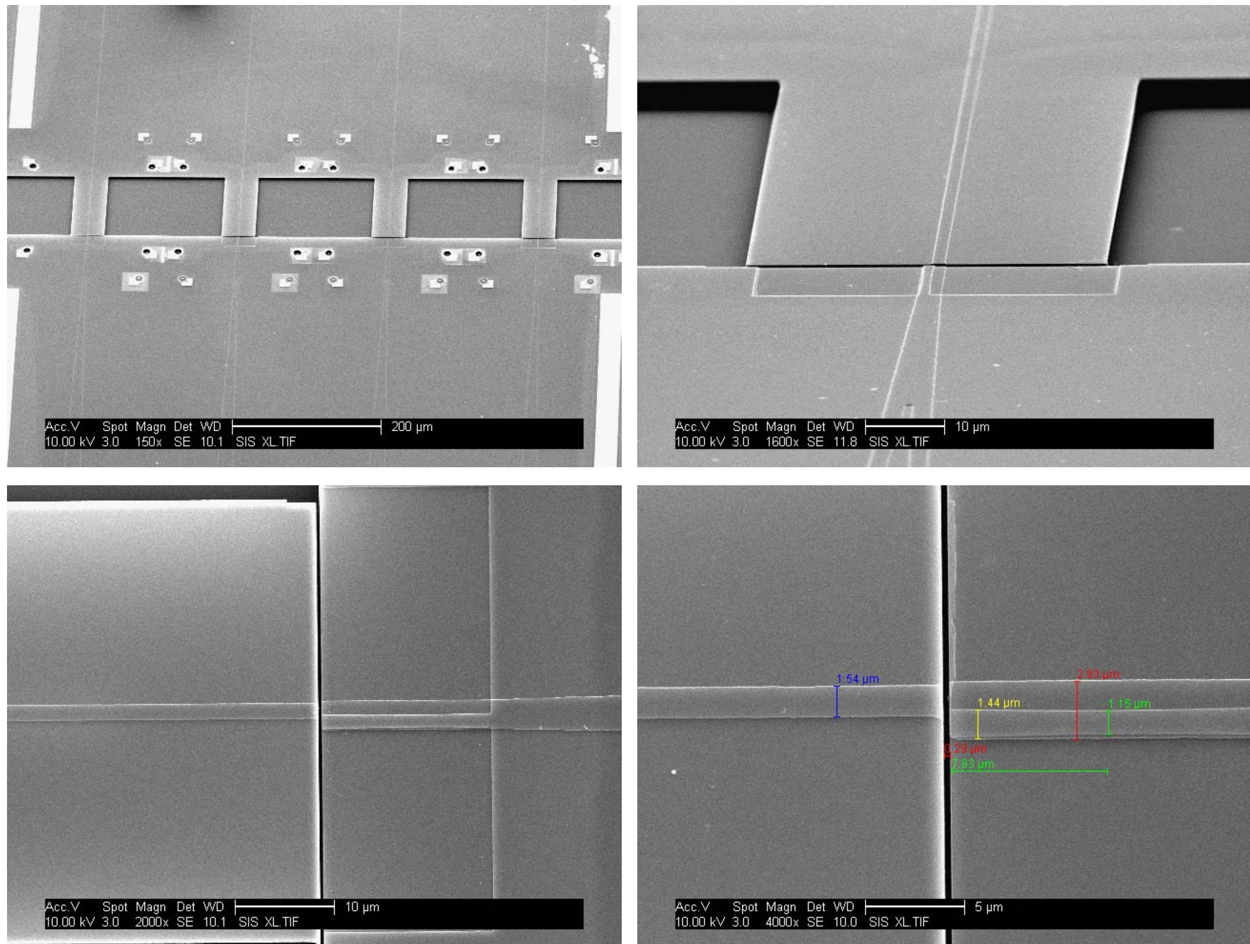

Figure 5-8: SEM images of photonic microcantilever array system

5.4 Measurement and Discussion

Scaled differential signals for multiple microcantilevers with the same step height are measured. Average measured scaled differential signals as a function of microcantilever deflection are shown in Figure 5-9, together with actual fabricated step heights. The slopes from the measurement data were averaged for each step height of the double-step rib waveguide. We also calculated the average peak difference of output powers as a function of the step height and combined with simulation results as shown in Figure 5-10 and Figure 5-11. Note that the measured signals are similar to simulation results in Figure 5-4.

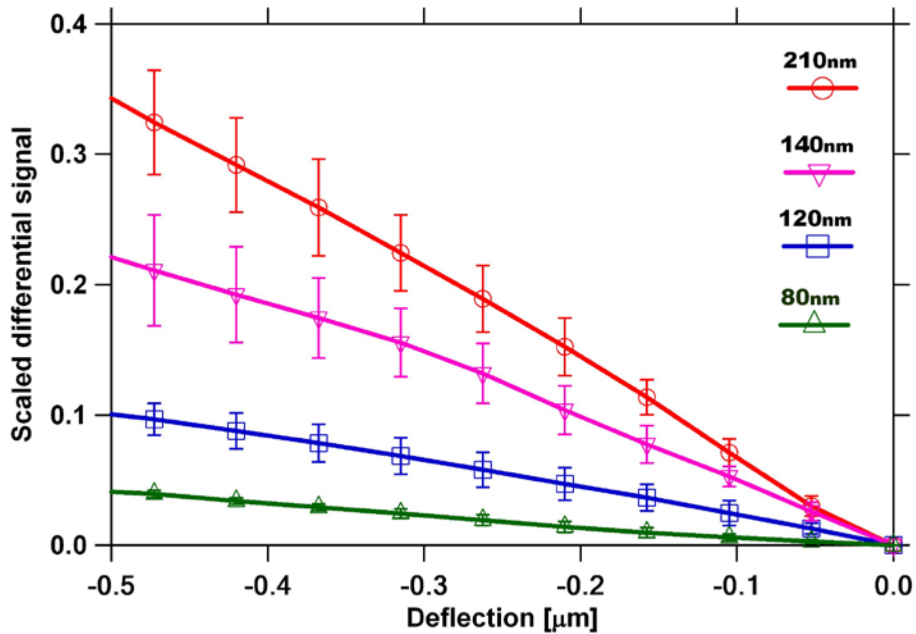

Figure 5-9: Average scaled differential signal as a function of deflection from measurement data of four photonic microcantilever arrays.

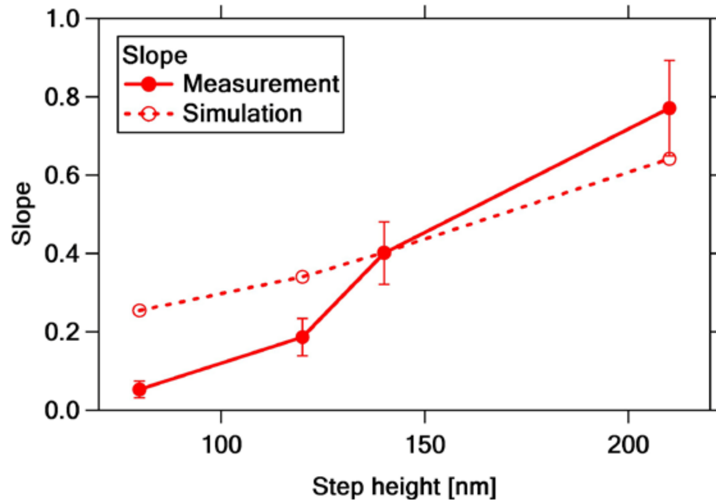

Figure 5-10: Average slope as a function of step height for measurement and simulation.

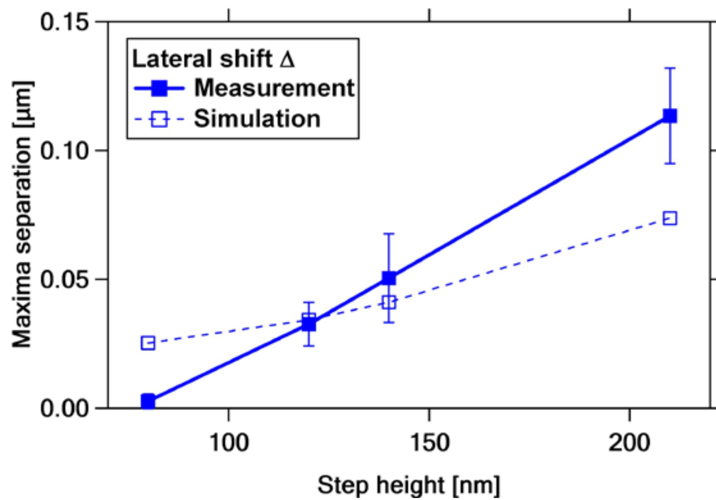

Figure 5-11: Average maxima separation of output powers as a function of step height for measurement and simulation.

The 210 nm step-height case has the largest slope among the measured scaled differential signals while the slope of the 80 nm case is the smallest. The smaller step heights (120 nm and 80 nm) result in less than predicted slope and lateral shift, Δ, while the opposite is true for larger step heights. The cause of this discrepancy is still under investigation. Nonetheless, the 210 nm step

height case results in a sensitivity of 0.77×10^{-3} nm^{-1}, which is 2.4 times greater than our previous result [22]. The sensitivity also determines the minimum detectable deflection (MDD), which corresponds to a signal-to-noise ratio of unity. Hence the MDD is the noise of the sensor response signal divided by the sensitivity.[80] The corresponding MDD is 59 pm for a 3.5 Hz measurement bandwidth.

5.5 Conclusion

We have explored the effect of double step rib waveguide structure on deflection measurement sensitivity. By increasing the step height of the double-step rib waveguide, the difference in mode coupling to the two lowest order modes is increased. Since each mode is preferentially directed into one of the two differential splitter outputs, the result is a larger shift between the outputs as a function of deflection, which increases the slope of the scaled differential signal. Simulation results are shown to be confirmed by experiment. The largest measured sensitivity obtained in this study is 0.77×10^{-3} nm^{-1}, which is comparable to the best reported for the optical lever method (10^{-3} nm^{-1}). The corresponding MDD is 59 pm for a 3.5 Hz measurement bandwidth.

6 SUMMARY AND FUTURE WORK

6.1 Summary

Microcantilever-based devices have been used in a variety of science and engineering fields since microcantilever probes were first used for atomic force microscopy. Microcantilever-based sensors have been investigated for a wide variety of applications and have been found to exhibit high sensitivity. To understand basic fundamentals of microcantilever-based sensors, the mechanical behavior of a simple cantilever beam, and its operation modes and readout methods, functionalization, and applications were briefly reviewed in Chapter 2.

The optical readout method using the laser beam reflection technique is the most sensitive in the conventional readout methods, but its application is limited by the number of microcantilevers that can be measured simultaneously. On the other hand, the piezoresistive and capacitive readout methods do lend themselves microcantilever arrays, but their sensitivity are significantly less than that of the optical method.

The in-plane photonic transduction method proposed by us is an alternative readout method that is scalable to large arrays. As shown in this dissertation, it can also achieve high sensitivity comparable to the optical lever method. A differential splitter with amorphous silicon strip-loaded multimode rib waveguide was used for the initial demonstration of the in-plane photonic transduction mechanism for silicon photonic microcantilevers. With the outputs of an asymmetrical multimode waveguide structure that terminates in a Y-branch splitter, a differential

signal can be formed, which has a monotonic response as a function of microcantilever deflection. Our design for the photonic microcantilever system was based on the photonic simulations to maximize the contrast of the differential signal. Fabrication and measurement of the photonic microcantilevers were described in Sections 3.2 and 3.3. A thermally stressed SU8 polymer patch was used to intentionally bend up the microcantilever in order to mechanically actuate the cantilever's deflection with a piezo-translator-mounted probe tip. The experimental results do not match with simulation due to microcantilever rotation and the power ratio of P_1/P_2. After accounting for rotation and power ratio, we find good agreement between simulation and measurement. The measured sensitivity is 0.135×10^{-3} nm^{-1} and the minimum detectable deflection is 0.35 nm for a 250Hz measurement bandwidth.

Further analysis of the differential splitter shows that the sensitivity is dependent on the refractive index of the strip on the multimode capture waveguide and on the waveguide structure. Moreover, we have encountered fabrication difficulties such as delamination and deformation of the amorphous silicon strip in the previous experiments. In order to improve sensitivity while maintaining the asymmetric structure of the differential splitter and eliminating fabrication issues, a new asymmetric double-step multimode rib waveguide was developed. Test samples were fabricated with two 8-microcantilever array sets with a three stage Y-branch splitter network that splits and delivers the input light to 8 photonic microcantilevers. The fabrication processes for the test samples were similar to what we have done for the previous samples with the exception that the asymmetric double-step rib is patterned with electron beam lithography for positioning accuracy followed by a 100 nm etch in an inductively coupled plasma reactive ion etcher (ICP-RIE). After inspecting the fully processed sample, we found 5 microcantilevers which were not usable due to fabrication imperfections. As a result, measurements focused on 11

of the 16 microcantilevers measured from two independent arrays. The measurement results showed reasonable uniformity and repeatability. The averaged scaled differential signal from the measurements was reasonably matched with simulation in the deflection range of -0.5 μm to 0.3 μm with noticeable disagreement for deflections greater than 0.3 μm due to a DC offset in the measurements. The sensitivity and MDD of the photonic microcantilever system are 0.32×10^{-3} nm^{-1} and 141 pm, respectively, which are comparable to or better than other common readout methods for nanomechanical static-deflection sensors.

We also investigated the effects on the sensitivity of the in-plane photonic transduction method when modifying the asymmetric structure of the double-step multimode rib waveguide. We explained analytically the relationship between the differential signal and the step height of the double-step rib waveguide and also the reason for the maxima separation between output power profiles, P_1 and P_2, which causes a monotonic signal response over the microcantilever deflection range. Four different step height cases were fabricated on two test samples, and then inspected by AFM and SEM to accurately measure the step-height. From the experimental results, a sensitivity of 0.77×10^{-3} nm^{-1} is achieved, which is 2.4 times greater than the previous result. Through these experiments, we confirmed that the output power peak difference shifts when the step height changes and that the performance of the in-plane all-photonic transduction method for the photonic microcantilever sensor is enhanced by modifying the structure of the double-step rib waveguide in the differential splitter. By increasing the step height of the double-step multimode rib waveguide in the differential splitter, we have significantly improved the sensitivity of the photonic microcantilever system and found a pathway for optimizing the in-plane photonic transduction method.

6.2 Future Work

The in-plane photonic transduction method using the differential splitter for photonic microcantilever is targeted at improving sensitivity and scalability. The demonstration of the photonic microcantilever system employing the transduction thus far shows a promising result to be able to use it for sensing applications in the real world. Currently, we are working on the practical demonstration with some sensing scenarios.

As discussed in Chapter 5, the performance of the photonic microcantilever system is affected by changes in the structure of the double-step rib waveguide. Through the former experiments to optimize the differential splitter structure for greater sensitivity, we have found that a real device does not exactly match with a simulation model. Simulations results are generally restricted to ideal situations, and so experimental approaches are required to apply for practical conditions. To conduct experiments relying on trial-and-error methodology is one way to maximize the performance of the photonic microcantilever sensor. Characterization and refinement of the differential splitter structure and the photonic microcantilever for optimal performance need to be implemented by the statistical approach of design of experiments. Because microcantilever based biosensors need to respond reliably to biomolecular interaction on the functionalized surface of the microcantilever, the spring constant (force constant) of the microcantilever beam has to be adjusted to the desired surface stress induced by the specific interaction that we are interested in. As discussed in Section 2.2.2, the spring constant is determined by dimensions and material properties. Hence, we change the length of the microcantilever to optimize its spring constant since it is the simplest way to reduce the cantilever beam's spring constant. To experimentally find the right length for our application, samples are fabricated with several different lengths. The structure of the double-step waveguide

is also modified to maximize its performance. Currently, these designs are in the experimental phase.

Our ultimate objective is to build lab-on-a-chip devices (LOC) or micro total analysis systems (μTAS) by integrating photonic microcantilever system with microfluidic devices for bio/chemical sensing applications. A microfluidic device is composed of one or more channels whose dimensions are usually hundreds of microns. Common aqueous solutions used in microfluidic devices contain proteins or antibodys, metal or ceramic particles, blood cells, tumor markers, and bacteria. Microfluidic devices have been used for a variety of sensing applications such as flow rate [81-83], viscosity [84-86], pH [87, 88], and chemical binding coefficients [89]. There are many other applications which are currently conducting in diverse research fields [90, 91]. Polydimethylsiloxane (PDMS) microfluidic device and sensing functionalization for the photonic microcantilever sensor are currently being pursued by other graduate students in our group.

7 REFERENCES

1. T. Thundat, E. A. Wachter, S. L. Sharp, and R. J. Warmack, "Detection of Mercury-Vapor Using Resonating Microcantilevers," Applied Physics Letters 66, 1695-1697 (1995).

2. R. Raiteri, M. Grattarola, and R. Berger, "Micromechanics senses biomolecules," Materials Today 5, 22-29 (2002).

3. J. Fritz, M. K. Baller, H. P. Lang, H. Rothuizen, P. Vettiger, E. Meyer, H.-J. Guumlntherodt, C. Gerber, and J. K. Gimzewski, "Translating Biomolecular Recognition into Nanomechanics," Science 288, 316-318 (2000).

4. G. Wu, R. H. Datar, K. M. Hansen, T. Thundat, R. J. Cote, and A. Majumdar, "Bioassay of prostate-specific antigen (PSA) using microcantilevers," Nat Biotech 19, 856-860 (2001).

5. R. Bashir, J. Z. Hilt, O. Elibol, A. Gupta, and N. A. Peppas, "Micromechanical cantilever as an ultrasensitive pH microsensor," Applied Physics Letters 81, 3091-3093 (2002).

6. A. M. Moulin, S. J. O'Shea, and M. E. Welland, "Microcantilever-based biosensors," Ultramicroscopy 82, 23-31 (2000).

7. K. M. Hansen, and T. Thundat, "Microcantilever biosensors," Methods 37, 57-64 (2005).

8. L. G. Carrascosa, M. Moreno, M. Álarez, and L. M. Lechuga, "Nanomechanical biosensors: a new sensing tool," TrAC Trends in Analytical Chemistry 25, 196-206 (2006).

9. ZhangJ, H. P. Lang, HuberF, BietschA, GrangeW, CertaU, McKendryR, H. J. Guntherodt, HegnerM, and GerberCh, "Rapid and label-free nanomechanical detection of biomarker transcripts in human RNA," Nat Nano 1, 214-220 (2006).

10. H. P. Lang, R. Berger, F. Battiston, J. P. Ramseyer, E. Meyer, C. Andreoli, J. Brugger, P. Vettiger, M. Despont, T. Mezzacasa, L. Scandella, H. J. Güntherodt, C. Gerber, and J. K. Gimzewski, "A chemical sensor based on a micromechanical cantilever array for the identification of gases and vapors," Applied Physics A: Materials Science & Processing 66, S61-S64 (1998).

11. J. D. Adams, G. Parrott, C. Bauer, T. Sant, L. Manning, M. Jones, B. Rogers, D. McCorkle, and T. L. Ferrell, "Nanowatt chemical vapor detection with a self-sensing, piezoelectric microcantilever array," Applied Physics Letters 83, 3428-3430 (2003).

12. L. Fadel, F. Lochon, I. Dufour, and O. Francais, "Chemical sensing: millimeter size resonant microcantilever performance," Journal of Micromechanics and Microengineering 14, S23-S30 (2004).

13. A. Boisen, J. Thaysen, H. Jensenius, and O. Hansen, "Environmental sensors based on micromachined cantilevers with integrated read-out," Ultramicroscopy 82, 11-16 (2000).

14. P. S. Waggoner, and H. G. Craighead, "Micro- and nanomechanical sensors for environmental, chemical, and biological detection," Lab on a Chip 7, 1238-1255 (2007).

15. M. Tortonese, R. C. Barrett, and C. F. Quate, "Atomic resolution with an atomic force microscope using piezoresistive detection," Applied Physics Letters 62, 834-836 (1993).

16. P. A. Rasmussen, J. Thaysen, O. Hansen, S. C. Eriksen, and A. Boisen, "Optimised cantilever biosensor with piezoresistive read-out," Ultramicroscopy 97, 371-376 (2003).

17. J. D. Adams, B. Rogers, L. Manning, Z. Hu, T. Thundat, H. Cavazos, and S. C. Minne, "Piezoelectric self-sensing of adsorption-induced microcantilever bending," Sensors and Actuators A: Physical 121, 457-461 (2005).

18. C. L. Britton, R. L. Jones, P. I. Oden, Z. Hu, R. J. Warmack, S. F. Smith, W. L. Bryan, and J. M. Rochelle, "Multiple-input microcantilever sensors," Ultramicroscopy 82, 17-21 (2000).

19. J. Amírola, A. Rodríguez, L. Castaňer, J. P. Santos, J. Gutiérrez, and M. C. Horrillo, "Micromachined silicon microcantilevers for gas sensing applications with capacitive read-out," Sensors and Actuators B: Chemical 111-112, 247-253 (2005).

20. G. Nordin, J. Cardenas Gonzalez, and M. A. George, "Optical waveguide microcantilever with differential output and associated methods of cantilever sensing," USPTO, ed. (University of Alabama in Huntsville, USA, 2007).

21. J. W. Noh, R. Anderson, S. Kim, J. Cardenas, and G. P. Nordin, "In-plane photonic transduction of silicon-on-insulator microcantilevers," Opt. Express 16, 12114-12123 (2008).

22. J. W. Noh, R. R. Anderson, S. Kim, W. Hu, and G. P. Nordin, "In-plane all-photonic transduction with differential splitter using double-step rib waveguide for photonic microcantilever arrays," Opt. Express 17, 20012-20020 (2009).

23. J. W. Noh, R. R. Anderson, S. Kim, W. Hu, and G. P. Nordin, "Sensitivity enhancement of differential splitter-based transduction for photonic microcantilever arrays," Nanotechnology submitted.

24. G. Binnig, C. F. Quate, and C. Gerber, "Atomic Force Microscope," Physical Review Letters 56, 930 (1986).

25. R. Berger, C. Gerber, J. K. Gimzewski, E. Meyer, and H. J. Guntherodt, "Thermal analysis using a micromechanical calorimeter," Applied Physics Letters 69, 40-42 (1996).

26. J. R. Barnes, R. J. Stephenson, M. E. Welland, C. Gerber, and J. K. Gimzewski, "Photothermal spectroscopy with femtojoule sensitivity using a micromechanical device," Nature 372, 79-81 (1994).

27. E. T. Arakawa, N. V. Lavrik, S. Rajic, and P. G. Datskos, "Detection and differentiation of biological species using microcalorimetric spectroscopy," Ultramicroscopy 97, 459-465 (2003).

28. S. Dohn, R. Sandberg, W. Svendsen, and A. Boisen, "Enhanced functionality of cantilever based mass sensors using higher modes," Applied Physics Letters 86, 233501-233503 (2005).

29. S. Hosaka, T. Chiyoma, A. Ikeuchi, H. Okano, H. Sone, and T. Izumi, "Possibility of a femtogram mass biosensor using a self-sensing cantilever," Current Applied Physics 6, 384-388 (2006).

30. M. Spletzer, A. Raman, A. Q. Wu, X. Xu, and R. Reifenberger, "Ultrasensitive mass sensing using mode localization in coupled microcantilevers," Applied Physics Letters 88, 254102-254103 (2006).

31. L. B. Sharos, A. Raman, S. Crittenden, and R. Reifenberger, "Enhanced mass sensing using torsional and lateral resonances in microcantilevers," Applied Physics Letters 84, 4638-4640 (2004).

32. R. Raiteri, M. Grattarola, H.-J. Butt, and P. Skládal, "Micromechanical cantilever-based biosensors," Sensors and Actuators B: Chemical 79, 115-126 (2001).

33. R. P. Cowburn, A. M. Moulin, and M. E. Welland, "High sensitivity measurement of magnetic fields using microcantilevers," Applied Physics Letters 71, 2202-2204 (1997).

34. E. Ohmichi, and T. Osada, "Torque magnetometry in pulsed magnetic fields with use of a commercial microcantilever," Review of Scientific Instruments 73, 3022-3026 (2002).

35. J. Liu, and X. Li, "A piezoresistive microcantilever magnetic-field sensor with on-chip self-calibration function integrated," Microelectronics Journal 38, 210-215 (2007).

36. B. D. Jensen, M. P. de Boer, N. D. Masters, F. Bitsie, and D. A. LaVan, "Interferometry of actuated microcantilevers to determine material properties and test structure nonidealities in MEMS," Microelectromechanical Systems, Journal of 10, 336-346 (2001).

37. R. Erlandsson, G. M. McClelland, C. M. Mate, and S. Chiang, "Atomic force microscopy using optical interferometry," Journal of Vacuum Science & Technology A: Vacuum, Surfaces, and Films 6, 266-270 (1988).

38. C. Kocabas, and A. Aydinli, "Design and analysis of an integrated optical sensor for scanning force microscopies," Sensors Journal, IEEE 5, 411-418 (2005).

39. K. Zinoviev, C. Dominguez, J. A. Plaza, V. J. C. Busto, and L. M. Lechuga, "A novel optical waveguide microcantilever sensor for the detection of nanomechanical forces," Lightwave Technology, Journal of 24, 2132-2138 (2006).

40. T. Thundat, R. J. Warmack, G. Y. Chen, and D. P. Allison, "Thermal and ambient-induced deflections of scanning force microscope cantilevers," Applied Physics Letters 64, 2894-2896 (1994).

41. S. M. Han, H. Benaroya, and T. Wei, "DYNAMICS OF TRANSVERSELY VIBRATING BEAMS USING FOUR ENGINEERING THEORIES," Journal of Sound and Vibration 225, 935-988 (1999).

42. A. C. Ugural, Mechanics of Materials (John Wiley and Son 2007).

43. C. Ziegler, "Cantilever-based biosensors," Analytical and Bioanalytical Chemistry 379, 946-959 (2004).

44. R. J. Jaccodine, and W. A. Schlegel, "Measurement of Strains at Si-SiO[sub 2] Interface," Journal of Applied Physics 37, 2429-2434 (1966).

45. X. Feng, Y. Huang, H. Jiang, D. Ngo, and A. J. Rosakis, "The effect of thin film/substrate radii on the Stoney formula for thin film/substrate subjected to nonuniform axisymmetric misfit strain and temperature," Journal of Mechanics of Materials and Structures 1, 12 (2006).

46. H. J. Butt, and M. Jaschke, "Calculation of thermal noise in atomic force microscopy," Nanotechnology 6, 1-7 (1995).

47. K. M. Goeders, J. S. Colton, and L. A. Bottomley, "Microcantilevers: Sensing Chemical Interactions via Mechanical Motion," Chemical Reviews 108, 522-542 (2008).

48. M. Sepaniak, P. Datskos, N. Lavrik, and C. Tipple, "Peer Reviewed: Microcantilever Transducers: A new Approach in Sensor Technology," Analytical Chemistry 74, 568 A-575 A (2002).

49. N. V. Lavrik, M. J. Sepaniak, and P. G. Datskos, "Cantilever transducers as a platform for chemical and biological sensors," Review of Scientific Instruments 75, 2229-2253 (2004).

50. I. K. Lin, Y.-M. Liao, Y. Liu, K.-S. Ou, K.-S. Chen, and X. Zhang, "Viscoelastic mechanical behavior of soft microcantilever-based force sensors," Applied Physics Letters 93, 251907-251903 (2008).

51. P. Paolino, and L. Bellon, "Frequency dependence of viscous and viscoelastic dissipation in coated micro-cantilevers from noise measurement," Nanotechnology 20, 405705 (2009).

52. R. Berger, H. P. Lang, C. Gerber, J. K. Gimzewski, J. H. Fabian, L. Scandella, E. Meyer, and H. J. G?therodt, "Micromechanical thermogravimetry," Chemical Physics Letters 294, 363-369 (1998).

53. X. Yu, J. Thaysen, O. Hansen, and A. Boisen, "Optimization of sensitivity and noise in piezoresistive cantilevers," Journal of Applied Physics 92, 6296-6301 (2002).

54. A. Kooser, R. L. Gunter, W. D. Delinger, T. L. Porter, and M. P. Eastman, "Gas sensing using embedded piezoresistive microcantilever sensors," Sensors and Actuators B: Chemical 99, 474-479 (2004).

55. J. Thaysen, A. Boisen, O. Hansen, and S. Bouwstra, "Atomic force microscopy probe with piezoresistive read-out and a highly symmetrical Wheatstone bridge arrangement," Sensors and Actuators A: Physical 83, 47-53 (2000).

56. G. Shekhawat, S.-H. Tark, and V. P. Dravid, "MOSFET-Embedded Microcantilevers for Measuring Deflection in Biomolecular Sensors," Science, 1122588 (2006).

57. M. Nordstrom, D. A. Zauner, M. Calleja, J. Hubner, and A. Boisen, "Integrated optical readout for miniaturization of cantilever-based sensor system," Applied Physics Letters 91, 103512-103513 (2007).

58. S. Cesaro-Tadic, G. Dernick, D. Juncker, G. Buurman, H. Kropshofer, B. Michel, C. Fattinger, and E. Delamarche, "High-sensitivity miniaturized immunoassays for tumor necrosis factor [small alpha] using microfluidic systems," Lab on a Chip 4, 563-569 (2004).

59. A. Bietsch, J. Zhang, M. Hegner, H. P. Lang, and C. Gerber, "Rapid functionalization of cantilever array sensors by inkjet printing," Nanotechnology 15, 873-880 (2004).

60. H. P. Lang, M. K. Baller, R. Berger, C. Gerber, J. K. Gimzewski, F. M. Battiston, P. Fornaro, J. P. Ramseyer, E. Meyer, and H. J. Güntherodt, "An artificial nose based on a micromechanical cantilever array," Analytica Chimica Acta 393, 59-65 (1999).

61. M. K. Baller, H. P. Lang, J. Fritz, C. Gerber, J. K. Gimzewski, U. Drechsler, H. Rothuizen, M. Despont, P. Vettiger, F. M. Battiston, J. P. Ramseyer, P. Fornaro, E. Meyer, and H. J. G?therodt, "A cantilever array-based artificial nose," Ultramicroscopy 82, 1-9 (2000).

62. D. R. Baselt, G. U. Lee, and R. J. Colton, "Biosensor based on force microscope technology," (AVS, 1996), pp. 789-793.

63. M. D. Antonik, N. P. D'Costa, and J. H. Hoh, "A biosensor based an micromechanical interrogation of living cells," Engineering in Medicine and Biology Magazine, IEEE 16, 66-72 (1997).

64. B. Ilic, D. Czaplewski, M. Zalalutdinov, H. G. Craighead, P. Neuzil, C. Campagnolo, and C. Batt, "Single cell detection with micromechanical oscillators," in The 45th international conference on electron, ion, and photon beam technology and nanofabrication(AVS, Washington, DC (USA), 2001), pp. 2825-2828.

65. B. H. Cha, S.-M. Lee, J. C. Park, K. S. Hwang, S. K. Kim, Y.-S. Lee, B.-K. Ju, and T. S. Kim, "Detection of Hepatitis B Virus (HBV) DNA at femtomolar concentrations using a silica nanoparticle-enhanced microcantilever sensor," Biosensors and Bioelectronics 25, 130-135 (2009).

66. H.-F. Ji, H. Gao, K. R. Buchapudi, X. Yang, X. Xu, and M. K. Schulte, "Microcantilever biosensors based on conformational change of proteins," The Analyst 133, 434-443 (2008).

67. G. P. Nordin, J. W. Noh, and S. Kim, "In-plane photonic transduction for microcantilever sensor arrays," in Nanoscale Imaging, Spectroscopy, Sensing, and Actuation for Biomedical Applications IV(SPIE, San Jose, CA, USA, 2007), pp. 64470J-64478.

68. G. P. Nordin, "In-Plane Photonic Transduction as an Enabler for Microcantilever Arrays," in ASME Workshop-Nanomechanics: Sensors and Actuators(Knoxville, TN, 2005).

69. G. P. Nordin, J. W. Noh, Y. Qian, J. Song, R. Anderson, and S. Kim, "Demonstration of in-plane photonic transduction for microcantilever arrays," in International Workshop on Nanomechanical Sensors(Montreal, Canada, 2007).

70. K. E. Burcham, G. N. De Brabander, and J. T. Boyd, "Micromachined silicon cantilever beam accelerometer incorporating an integrated optical waveguide," in Integrated Optics and Microstructures(SPIE, Boston, MA, USA, 1993), pp. 12-18.

71. S. Wu, and H. J. Frankena, "Integrated optical sensors using micromechanical bridges and cantilevers," in Integrated Optics and Microstructures(SPIE, Boston, MA, USA, 1993), pp. 83-89.

72. J. Thaysen, A. D. Yalcinkaya, P. Vettiger, and A. Menon, "Polymer-based stress sensor with integrated readout," Journal of Physics D: Applied Physics 35, 2698-2703 (2002).

73. X. Yu, Y. Tang, H. Zhang, T. Li, and W. Wang, "Design of High-Sensitivity Cantilever and Its Monolithic Integration With CMOS Circuits," Sensors Journal, IEEE 7, 489-495 (2007).

74. W. Hu, R. Anderson, Y. Qian, J. Song, J. W. Noh, S. Kim, and G. P. Nordin, "Demonstration of microcantilever array with simultaneous readout using an in-plane photonic transduction method," Review of Scientific Instruments 80, 085101-085107 (2009).

75. R. L. Gunter, R. Zhine, W. G. Delinger, K. Manygoats, A. Kooser, and T. L. Porter, "Investigation of DNA sensing using piezoresistive microcantilever probes," Sensors Journal, IEEE 4, 430-433 (2004).

76. V. Tabard-Cossa, M. Godin, L. Y. Beaulieu, and P. Grütter, "A differential microcantilever-based system for measuring surface stress changes induced by electrochemical reactions," Sensors and Actuators B: Chemical 107, 233-241 (2005).

77. H.-F. Ji, K. M. Hansen, Z. Hu, and T. Thundat, "Detection of pH variation using modified microcantilever sensors," Sensors and Actuators B: Chemical 72, 233-238 (2001).

78. S. R. Manalis, S. C. Minne, A. Atalar, and C. F. Quate, "Interdigital cantilevers for atomic force microscopy," Applied Physics Letters 69, 3944-3946 (1996).

79. C. Schonenberger, and S. F. Alvarado, "A differential interferometer for force microscopy," Review of Scientific Instruments 60, 3131-3134 (1989).

80. T. E. Schäffer, and P. K. Hansma, "Characterization and optimization of the detection sensitivity of an atomic force microscope for small cantilevers," Journal of Applied Physics 84, 4661-4666 (1998).

81. A. Rasmussen, C. Mavriplis, M. E. Zaghloul, O. Mikulchenko, and K. Mayaram, "Simulation and optimization of a microfluidic flow sensor," Sensors and Actuators A: Physical 88, 121-132 (2001).

82. J. Collins, and A. P. Lee, "Microfluidic flow transducer based on the measurement of electrical admittance," Lab on a Chip 4, 7-10 (2004).

83. V. Lien, and F. Vollmer, "Microfluidic flow rate detection based on integrated optical fiber cantilever," Lab on a Chip 7, 1352-1356 (2007).

84. P. Galambos, and F. Forster, "An Optical Micro-fluidic Viscometer," in ASME Intl. Mech. Eng. Cong. & Exp.(Anaheim, CA, 1998), pp. 187-191.

85. P. Guillot, P. Panizza, J.-B. Salmon, M. Joanicot, A. Colin, C.-H. Bruneau, and T. Colin, "Viscosimeter on a Microfluidic Chip," Langmuir 22, 6438-6445 (2006).

86. C. S. Lo, P. D. Prewett, G. J. Davies, C. J. Anthony, and K. Vanner, "The Micromagnetoflowcell - A Microfluidic Viscometer," in World Congress on Engineering(London, UK, 2007), pp. 1379-1384.

87. B. H. Weigl, and P. Yager, "Silicon-microfabricated diffusion-based optical chemical sensor," Sensors and Actuators B: Chemical 39, 452-457 (1997).

88. K. Macounova, C. R. Cabrera, M. R. Holl, and P. Yager, "Generation of Natural pH Gradients in Microfluidic Channels for Use in Isoelectric Focusing," Analytical Chemistry 72, 3745-3751 (2000).

89. A. E. Kamholz, B. H. Weigl, B. A. Finlayson, and P. Yager, "Quantitative Analysis of Molecular Interaction in a Microfluidic Channel: The T-Sensor," Analytical Chemistry 71, 5340-5347 (1999).

90. D. Erickson, and D. Li, "Integrated microfluidic devices," Analytica Chimica Acta 507, 11-26 (2004).

91. B. Kuswandi, Nuriman, J. Huskens, and W. Verboom, "Optical sensing systems for microfluidic devices: A review," Analytica Chimica Acta 601, 141-155 (2007).